UTILIZATION OF REDUCIBLE MIXED METAL OXIDES AS PROMOTERS FOR THE ENHANCEMENT OF SULFUR REGENERATION IN NSR CATALYSTS

A THESIS SUBMITTED TO

THE GRADUATE SCHOOL OF ENGINEERING AND SCIENCE

OF BILKENT UNIVERSITY

IN PARTIAL FULFILLMENT OF THE REQUIREMENTS FOR

THE DEGREE OF

MASTER OF SCIENCE

IN

CHEMISTRY

By

ZEHRA AYBEGÜM SAMAST

July 2016

UTILIZATION OF REDUCIBLE MIXED METAL OXIDES AS PROMOTERS FOR THE ENHANCEMENT OF SULFUR REGENERATION IN NSR CATALYSTS

By Zehra Aybegüm Samast

July, 2016

We certify that we have read this thesis and that in our opinion it is fully adequate, in scope and in quality, as a thesis for the degree of Master of Science.

_____

Emrah Özensoy (Advisor)

_____

Ferdi Karadaş

_____

Damla Eroğlu Pala

Approved for the Graduate School of Engineering and Science:

_____

Prof. Dr. Levent Onural

Director of the Graduate School

ABSTRACT

UTILIZATION OF REDUCIBLE MIXED METAL OXIDES AS PROMOTERS FOR THE ENHANCEMENT OF SULFUR REGENERATION IN NSR CATALYSTS

ZEHRA AYBEGÜM SAMAST

M.S. in Chemistry
Advisor: Emrah Özensoy
July 2016

Pt functionalized binary, ternary, and quaternary oxides (e.g. Pt/BaO/CeO_2/ZrO_2/Al_2O_3) were synthesized by wetness impregnation method and characterized by X-ray Diffraction (XRD), Brunauer–Emmett–Teller (BET) surface area analysis, *in-situ* Fourier Transform Infrared (FTIR), and temperature programmed desorption (TPD) techniques. Effect of the synthesis sequence on the NO_x storage capacity was investigated by synthesizing subsequently impregnated and co-impregnated ternary oxides. Influence of BaO loading on NO_x uptake of quaternary oxides was examined by utilizing two different BaO loadings namely; 8 wt% and 20 wt% on co-impregnated ternary oxide, Pt10-10CeZrAl. Co-presence of CeO_2-ZrO_2 oxide domains leads to an increase in NO_x storage. As BaO loading increases in quaternary oxides, thermal stabilities of nitrates and nitrites increase due to the formation of bulk/ionic nitrates. Although BaO impregnation on co-impregnated ternary oxides leads to a decrease in specific surface area (SSA) values due to sintering, NO_x adsorption on BaO-functionalized

quaternary oxides was found to be higher than the BaO deficient ternary oxides. Upon sulfur poisoning, formation of strongly bound bulk/ionic sulfate/sulfite functional groups on BaO containing catalysts result in a need for higher temperatures for complete sulfur regeneration. Comparison of the CeO_2-ZrO_2 promoted systems with that of the Pt/ 20 wt% Ba/Al_2O_3 conventional NO_x Storage Reduction (NSR) catalyst suggests that ceria-zirconia promotion enhances the sulfur tolerance. In conclusion, in this study a new NSR catalyst namely, Pt20Ba10-10CeZrAl, which is promoted with reducible mixed metal oxides, was synthesized and characterized. This novel NSR catalyst formulation revealed favorable sulfur resistance with minor sacrifice in NO_x storage ability.

Keywords: NSR, $DeNO_x$, catalyst, BaO, Pt, CeO_2, Zr_2O, Al_2O_3, NO_x storage capacity, sulfur poisoning.

ÖZET

İNDİRGENEBİLİR KARIŞIK METAL OKSİTLERİN KULLANIMI İLE NDİ KATALİZÖRLERİNİN KÜKÜRT DİRENCİNİN ARTIRILMASI

ZEHRA AYBEGÜM SAMAST

Kimya, Yüksek Lisans
Tez Danışmanı: Emrah Özensoy
Temmuz 2016

Bu çalışmada, Pt ile işlevselleştirilmiş ikili, üçlü ve dörtlü oksitler (örn. Pt/BaO/CeO_2/ZrO_2/Al_2O_3), ıslak emdirme yöntemi ile sentezlenmiştir. Ardından bu malzemelerin, XRD (X-Işını Difraksiyonu), BET (Brunauer, Emmett ve Teler) yüzey alanı ölçümleri, in-situ FT-IR (Fourier Dönüşüm Infrared Spektroskopisi) ve TPD (Sıcaklık Programlı Desorpsiyon) teknikleri kullanılarak karakterizasyonları yapılmıştır. Üçlü oksitlerin sıralı veya aynı anda eklenmesi ile sentez dizisinin NO_x depolama kapasitesi üzerine etkisi incelenmiştir. Dörtlü oksitlerin yapısında bulunan BaO oranının, NO_x alımına etkisi, üçlü oksit, Pt10-10CeZrAl, yapısına kütlece % 8 ve % 20 BaO eklenmesi ile incelenmiştir. Yapılan deneylerde, katalizör yapısına CeO_2-ZrO_2 oksitlerinin aynı anda eklenmesinin, NO_x depolama kapasitesinde artışa neden olduğu görülmüştür. Pt/20ZrO_2/Al_2O_3 katalizörü yapısındaki nitrat ve nitritlerin ısıl kararlılıkları, Pt/20 CeO_2/Al_2O_3 katalizöründekilerden daha yüksektir. Ayrıca, dörtlü oksit yapılarındaki BaO oranı arttıkça, oylum (külçe)/iyonik nitrat oluşumlarından

dolayı yapıdaki nitrat ve nitritlerin ısıl kararlılıkları artmaktadır. Eş zamanlı sentezlenmiş üçlü katalizöre eklenen BaO, oylum (külçe)/iyonik yapıdaki nitratların oluşumunun artmasından dolayı katalizörün yüzey alanının düşmesine neden olmaktadır. Buna rağmen, BaO içeren dörtlü katalizörlerdeki NO_x depolama oranı, BaO içermeyenlerden daha fazladır. Buna ek olarak, yapıdaki BaO oranı arttıkça, NO_x depolama kapasitesinde de artış gözlemlenmiştir. Kükürt zehirlenmesinin ardından elde edilen spektroskopik ölçümler sonucunda, BaO içeren katalizörler üzerinde güçlü bağlanmış, iyonik yapıda sülfat ve sülfit fonksiyonel gruplarının oluşmasının, katalizörün rejenerasyonunu zorlaştırdığı ve rejenerasyon için gerekli sıcaklıkların artmasına neden olduğu görülmektedir. CeO_2-ZrO_2 oksit sistemini içeren katalizörlerde, ticari Pt/20Ba/Al_2O_3 katalizörüne göre çok daha düşük kükürt alımı gözlemlenmiştir. Sonuç olarak bu çalışmada, indirgenebilir metal oksit karışımlarıyla geliştirilmiş; yeni bir NO_x Depolama ve İndirgeme (NDİ) katalizörleri sentezlenmiş, yapısal özellikleri incelenmiş ve bu yeni katalizörün, ticari katalizöre göre NO_x depolama yeteneğinden biraz feda ederek daha üstün kükürt direnci gösterdiği belirlenmiştir.

Anahtar sözcükler: NDİ, $DeNO_x$ katalizörleri, BaO, Pt, CeO_2, Zr_2O, Al_2O_3, NO_x NO_x depolama kapasitesi, kükürt zehirlenmesi.

Acknowledgement

I would like to extend my gratitude to my advisor Assoc. Prof. Emrah Özensoy for his valuable knowledge, encouragement, supervision, patience and guidance throughout my studies. I would like to state my sincere thanks to him for providing me the opportunity to study in his research groups.

Especially, I would like to thank to Merve Tohumeken for her valuable friendship, scientific discussion and emotional support. I will never forget our conversations, thank you Merve for making my days better.

I wish to thank to Kerem Emre Ercan, Deniz Erdoğan, Mustafa Karatok, Mustafa Çağlayan, Zafer Say and other Özensoy group members for their support through my studies.

I also would like to express my gratitude to past and present members of Chemistry Department; especially to Gülbahar Saat, Pınar Alsaç, Emre Köken, Obadah Albahra, Ethem Anber and Deniz Gökçeaslan.

I also wish to send my thanks to Nihan Büyükbayram, Zelal Yavuz, Canan Erdoğan, Şehmus Tohumeken who have provided me good memories in both my personal life and academic study. I thank them all for their valuable friendship.

I also acknowledge to TUBITAK for financial support.

I wish specially thank to my family; “Samast Family” and “Ok Family”. I am grateful to my parents Yüksel and Münüre; my siblings Hamza, Aybüke (and Baby Samast ☺), Bilge and Buğra for their love, continuous support and encouragement. There are not enough words to express my deep loyalty and love for them. I cannot imagine life without them. I love being a part of these two families. I wish them long, beautiful and peaceful life to spend together.

Lastly, my deepest thank to my love Mehmet Sefa Ok, I would like to thank you for your endless support and unconditional love. I love you. ♥♥♥

Dedicated to my Family and

my love Mehmet Sefa Ok

Contents

List of Figures

List of Tables

List of Abbreviations

BET: Brunauer-Emmett-Teller

FTIR: Fourier Transform Infrared Spectroscopy

IR: Infrared

JCPDS: Joint Committee on Powder Diffraction Standards

NIST: National Institute of Standards and Technology

NO_x: Nitrogen Oxides (e.g. N_2O, NO, NO_2)

NSR: NO_x Storage and Reduction

NSC: NO_x Storage Capacity

PID: Proportional Integral Derivative

QMS: Quadruple Mass Spectrometer

SCR: Selective Catalytic Reduction

SO_x: Sulfur Oxides (e.g. SO_2, SO_3)

SMSI: Strong Metal Support Interaction

SSA: Specific Surface Area

TPD: Temperature Programmed Desorption

XRD: X-Ray Diffraction

Chapter 1

Introduction

1.1. Air Pollution Problem

Air pollution is a significant problem that poses several challenges all over the world due to its adverse effects on human health, ecosystem and climate. Air pollutants such as nitrogen oxides (NO_x) and sulfur oxides (SO_x) can induce loss of wildlife as they lead to acidification of lakes, soil, and rivers. In addition, air pollution is a substantial problem that cause serious health impact such as increasing the mortality risks, premature death, and cardiovascular diseases. Furthermore, it has also severe considerable economic implications such as decreasing productivity and increasing medical costs. European Commission estimates that in 2010, total health-related annual economic damages of environmental pollution was 940 billion EUR [1]. According to a study performed by the European Environment Agency (EEA) in 2009, % 58 of NO_x, %21 of SO_x and %30 of CO emissions occur because of automobile sector in 32 European countries [2]. In order to avoid undesirable consequences of air pollution, various emission limits were established in Europe since 1993. Some of these regulations are summarized in Table 1.

Table 1. Evolution of environmental regulations for air pollutants from mobile sources in Europe (Copyright © 2011 Elsevier [3]).

	gasoline engine				diesel engine			
standard regulation[a]	CO	HC	NO_x	HC + NO_x	CO	NO_x	HC + NO_x	particulates
Euro 1 (1993)	2.72			0.97	2.72		0.97	0.14
Euro 2 (1996)	2.20			0.5	1.00		0.90	0.10
Euro 3 (2000)	2.30	0.20	0.15		0.64	0.50	0.56	0.05
Euro 4 (2005)	1.00	0.10	0.08		0.50	0.25	0.30	0.025
Euro 5 (2009)	1.00	0.10	0.06		0.50	0.18	0.25	0.005
Euro 6 (2014)	1.00	0.10	0.06		0.50	0.08	0.17	0.005

a Measured from New European Driving Cycle (g/km).

In order to satisfy these emission regulations, new technologies such as NO_x Storage and Reduction (NSR) and Selective Catalytic Reduction (SCR) have been developed by the automobile industry. Figure 1 presents the changes in the per cent emissions of various air pollutants in Europe in between 2004 and 2013. Additionally, Figure 2 shows the changes in the emission of selected air pollutants for transportation sector between the years 2004 and 2013. As can be seen from Figure 2, SO_x and NO_x emissions decreased about % 60 and % 30, respectively in this period. Furthermore, particular matter (PM) emissions (which are also classified as carcinogenic), decreased ca. % 25 due to improvements in the commercial catalytic emission control systems.

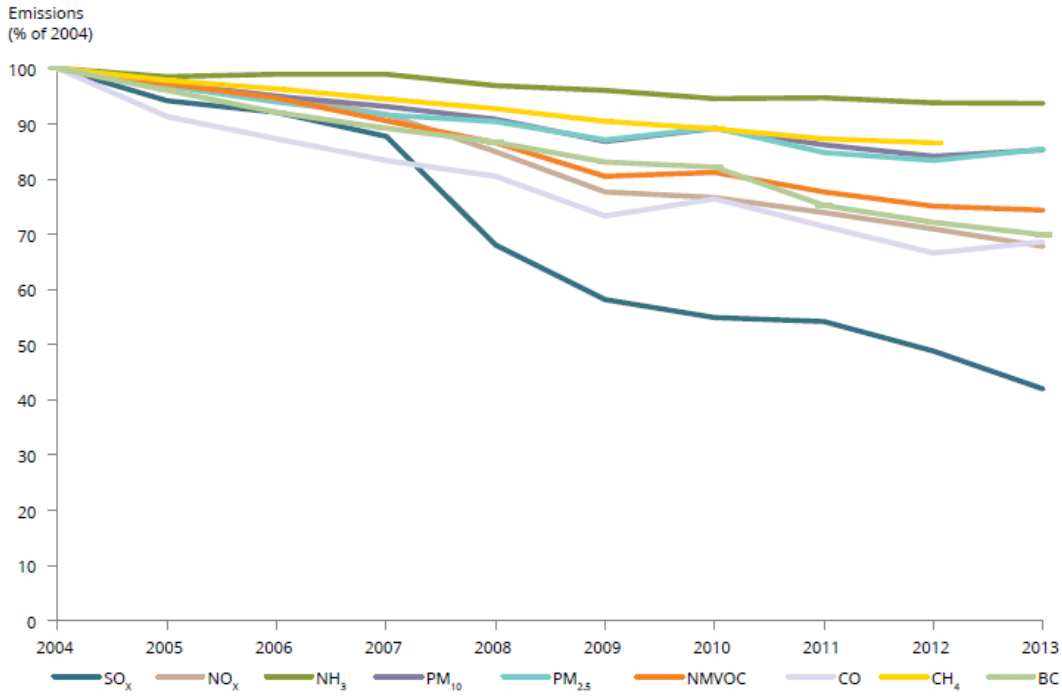

Figure 1. Variations in the emissions of SO_x , NO_x , NH_3 , PM_{10} , $PM_{2.5}$, NMVOCs ,CO ,CH_4, BC for all sectors in Europe between 2004-2013 [4]. (Copyright notice © European Environment Agency, 2015.)

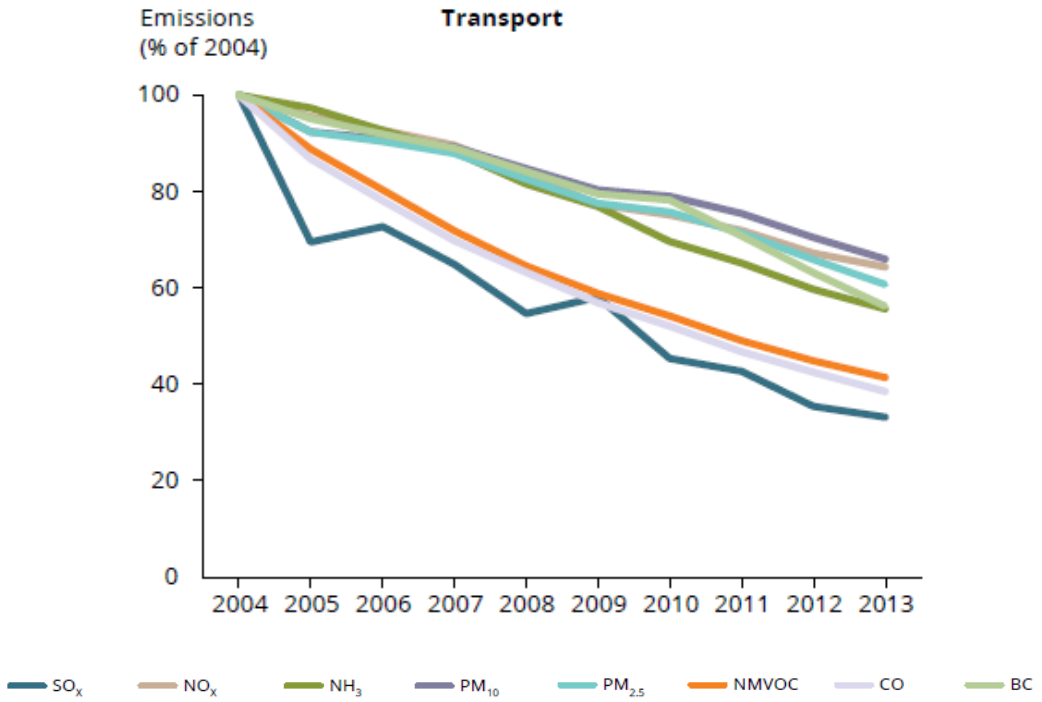

Figure 2. Changes the in the emissions of SO_x , NO_x , NH_3 , PM_{10} , $PM_{2.5}$, NMVOCs ,CO ,CH_4, BC for transportation sector in Europe between 2004-2013 [4]. (Copyright notice © European Environment Agency, 2015.)

Recent developments in automobile industry enabled a significant decrease in the emission of air pollutants, particularly in NO_x and SO_x emissions, however it can be observed clearly from the Figure 3 that the percentage of transport sector in emissions of air pollutants are still considerably high [5]. Performances of current catalytic systems are not sufficient to fulfill Euro 6 targets under realistic driving conditions. Figure 4 shows change in NO_x emission amounts for European countries with the National Emission Ceilings Directive (NECD) 2010 and the Gothenburg protocol targets. As it can be seen from Figure 4, unfortunately, in some countries such as Turkey, NO_x emissions increased between the years 1990-2012. In addition, NO_x emissions in most of the European

countries also need to be decreased further in order to achieve 2020 Gothenburg targets [6].

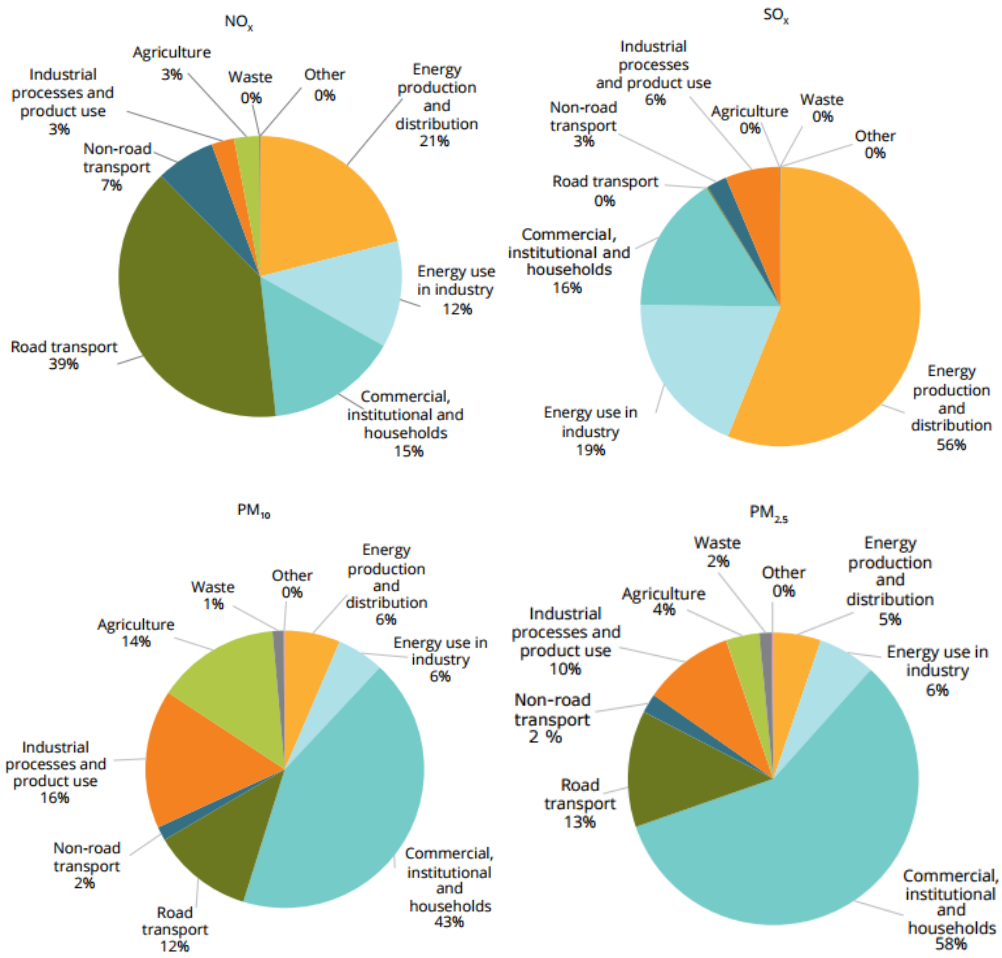

Figure 3. Share of NO_x, SO_x, PM_{10} and $PM_{2.5}$ emissions by different sectors in Europe in 2013 [5]. (Copyright notice © European Environment Agency, 2015.)

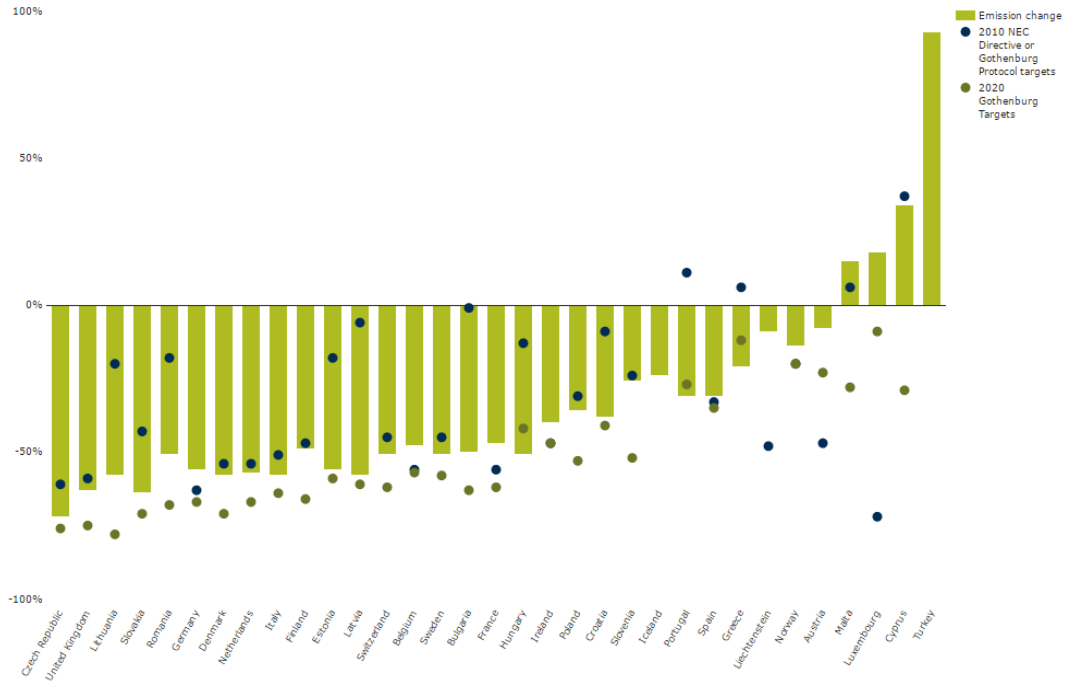

Figure 4. Change in NO_x emissions for European countries with the NECD (National Emission Ceilings Directive) 2010 and the Gothenburg protocol targets [6]. (Copyright notice © European Environment Agency, 2015.)

1.2. NO_x Storage and Reduction (NSR) Catalysis

The implementation of new technologies in automobile industry to fulfill emission standards have provided remarkable results. One of the technologies that was innovated by Toyota Motor Company in 1995 was NO_x Storage and Reduction Catalysts [7]. Before the introduction of the NSR catalysts in diesel engine cars, other conventional catalytic technologies were being employed. For instance, in the gasoline engine vehicles, Three Way Catalysts (TWC) have been commonly used. Operational principle of TWC include the following simultaneous oxidation and reduction reactions operated at a specific air/fuel stoichiometric ratio of 14.7 as can be seen in Figure 5 [8], [3].

Oxidation

$$CO + \frac{1}{2} O_2 \rightarrow CO_2 \qquad (1)$$

$$C_xH_y + (x+y/4)\, O_2 \rightarrow xCO_2 + y/2\, H_2O \qquad (2)$$

Reduction

$$NO + H_2 \rightarrow \frac{1}{2} N_2 + H_2O \qquad (3)$$

$$NO + CO \rightarrow \frac{1}{2} N_2 + CO_2 \qquad (4)$$

$$(2x + y/2)\, NO + C_xH_y \rightarrow (x+y/4)\, N_2 + xCO_2 + y/2\, H_2O \qquad (5)$$

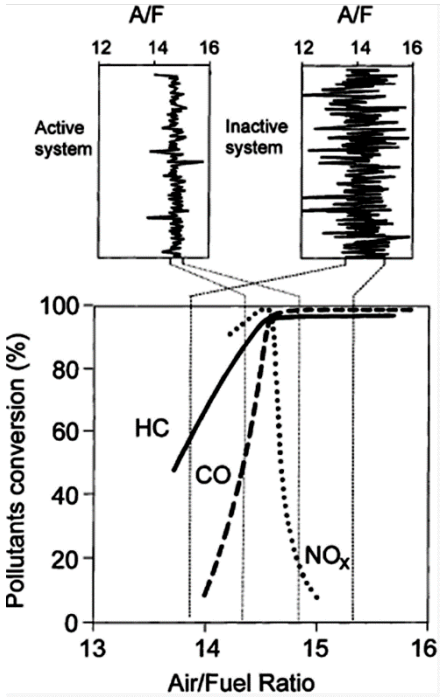

Figure 5. Effect of air to fuel ratio on the catalytic efficiency of TWC (Copyright © 2003 Elsevier [9].

NSR catalysts work in a cyclic operation mode including a 1-2 min lean cycle and a subsequent 3-5 s rich cycle [10-12]. Under lean conditions (i.e. in the presence of excess oxygen, typically λ>20 where λ=Air to fuel ratio stoichiometric), combustion and NO_x adsorption/oxidation take place; while during the rich cycle (i.e. under reducing environment with a λ< 1), reduction of adsorbed NO_x species occurs [13]. The operational mechanism of NSR catalysts can be summarized in five steps:

(a) Oxidation of NO to NO_2 (λ>1)

(b) NO_x adsorption as nitrates or nitrites on basic sites of the catalyst (λ>1)

(c) Injection of reductants (e.g. CO, C_xH_y) to the exhaust stream (λ<1)

(d) Nitrate/nitrite decomposition, NO_x release from the catalyst (λ<1)

(e) NO_x reduction to N_2 (λ<1)

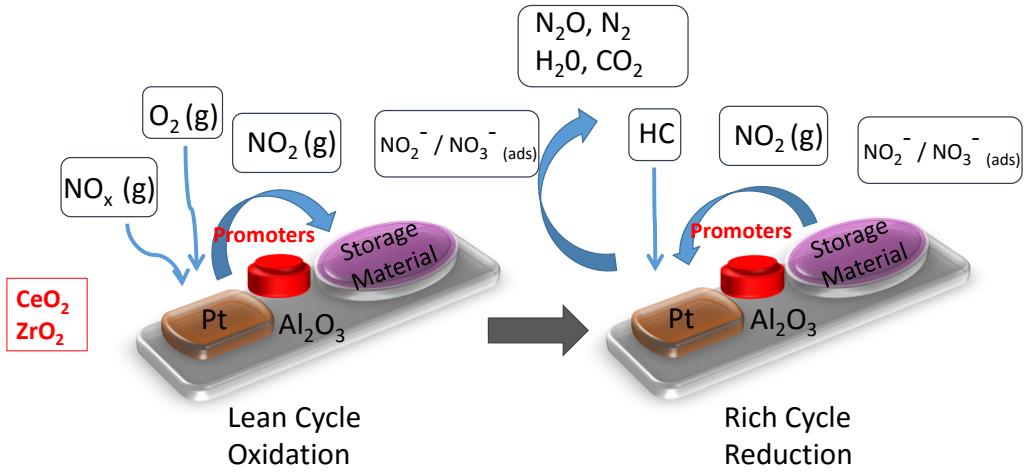

Figure 6. Schematic presenting the fundamental operational principles of NSR catalysts.

During the lean cycle, NO oxidation to NO_2 and NO_x adsorption occur primarily over precious metal sites. Then, acidic nitrogen oxides are stored on basic storage domains in the form of nitrates or nitrites. Alkaline oxide or alkaline-earth oxide components such as BaO, K_2O, CeO_2, ZrO_2, MgO, CaO and SrO were used in the past as storage domains [14-17]. Different reaction mechanisms have been reported in the literature for the NO_x sorption process on the basic BaO sites [18-20]. For instance, Fridell et al. proposed a three-step storage mechanism as shown below:[19]

$$BaO + NO_2 \rightarrow BaO\text{-}NO_2 \qquad (6)$$

$$BaO\text{-}NO_2 \rightarrow BaO_2 + NO \qquad (7)$$

$$BaO_2 + 2NO_2 \rightarrow Ba(NO_3)_2 \qquad (8)$$

On the other hand, Forzatti and co-workers proposed a mechanism that has two parallel routes for nitrate (NO_3^-) and nitrite (NO_2^-) formation [21]. As can be seen in Figure 7, in the nitrate route, after NO oxidation to NO_2 on Pt, NO_2 is stored by NO_2 spillover on Ba sites to form Ba-Nitrates with NO (g) formation. In the nitrite route, after NO oxidation on Pt, NO_2 is stored directly on Ba sites as nitrites and then nitrites are oxidized to nitrates.

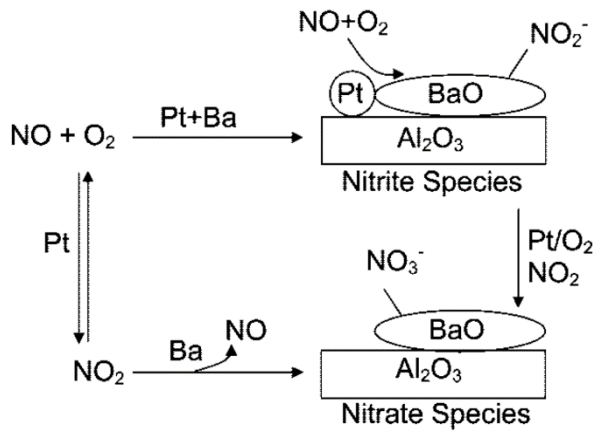

Figure 7. Two different pathways for NO oxidation and subsequent adsorption on $Pt/Ba/Al_2O_3$. (Copyright 2006 Elsevier B.V.)

It is also worth mentioning that BaO loading in the catalyst is crucial for the dominance of different storage routes. As Ba loading increases, nitrite route becomes dominant due to increase in the Pt-Ba interfacial sites [21-24].

Under reducing conditions, stored nitrates/nitrites are removed from the surface of the catalyst with the help of reductants such as H_2, CO or hydrocarbons (e.g. C_3H_6 or C_3H_8). Reduction mechanism of trapped NO_x can be summarized using the following reactions: [21, 25]

$$Ba(NO_3)_2 + 5\ CO \rightarrow N_2 + BaO + 5\ CO_2 \qquad (9)$$

$$Ba(NO_3)_2 + 5\ H_2 \rightarrow N_2 + BaO + 5\ H_2O \qquad (10)$$

$$Ba(NO_3)_2 + 3\ H_2 \rightarrow BaO + 2\ NO + 3\ H_2O \qquad (11)$$

$$Ba(NO_3)_2 + 4\ H_2 \rightarrow BaO + N_2O + 4\ H_2O \qquad (12)$$

$$Ba(NO_3)_2 + 8\ H_2 \rightarrow BaO + 2\ NH_3 + 5\ H_2O \qquad (13)$$

1.2.1. Compositions of NSR Catalysts

There are three major structural components in the formulation of the NSR catalysts; a support material, oxidation- reduction (i.e. redox) active sites and a NO_x storage component. As a support material, ɣ-Al_2O_3 is preferred due to its high surface area, robustness and favorable surface functional groups enabling good Pt and Ba dispersion as well as efficient NO_x storage [26]. For the redox active sites, precious metals such as Pt, Pd and Rh can be used in order to catalyze NO oxidation under lean conditions and NO_x reduction under rich conditions as well as for SO_x regeneration. Burch and Millington reported that reduction of NO attenuates over precious metals under lean conditions and Pt based catalysts have the highest NO conversion at low temperatures (Figure 8) [27]. Baiker et al. investigated a series of 1 wt % Pt functionalized catalysts with different metal oxide supports such as alumina and silica and found that the lowest NO_x storage capacity belongs to Pt/SiO_2 [17].

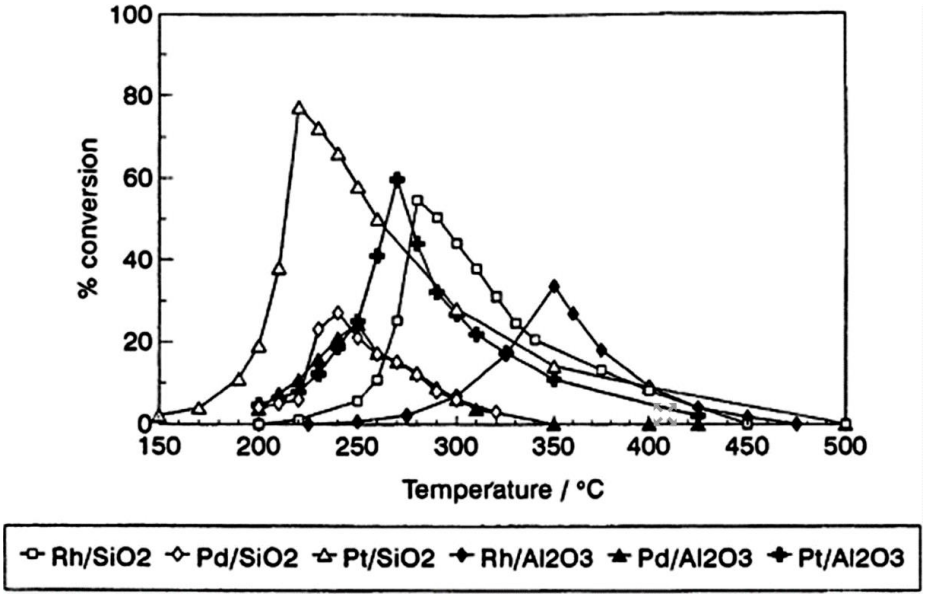

Figure 8. Reduction of NO by propene (C_3H_6) as a function of temperature on monometallic Rh, Pd and Pt supported on SiO_2 or Al_2O_3. (Flow Gas Composition: 500 ppm NO, 1000 ppm C_3H_6, 5%O_2) (Copyright © 1995 Elsevier [27].)

Correlation between Pt crystallite (i.e. particle) size and NO oxidation capacity have been extensively studied in the literature. Kim et al. reported the critical role of Pt particle size in NO_x storage capacity on Pt functionalized BaO/Al_2O_3 catalysts. They found negative effect of Pt sintering during thermal treatment on NO_x storage activity [28]. Lee and Kung examined oxidation of NO on Pt/ Al_2O_3 catalysts of 82% and 4.4% Pt dispersion and they found that decrease in Pt crystallite size leads to an increase in turnover frequency of NO oxidation to NO_2. Pt is also known as a good promoter to reduce nitrates and nitrites under rich conditions. A study on the H_2 activation ability showed that Pt can be used to promote the reduction of stored NO_x at temperatures as low as 150 ^oC [29]. Electron transfer due to high oxygen content results in the loss of catalytic activity

due to the formation of mobile platinum oxides, PtO (Pt^{2+}) and PtO_2 (Pt^{4+}) and sintering [30].

As a NO_x absorbent material, strongly basic oxides such as BaO are preferred. Barium can be present as BaO, BaO_2, $Ba(OH)_2$ and $BaCO_3$ in $Pt/Ba/Al_2O_3$ catalysts synthesized by the wetness impregnation method. NO_x storage preferentially happens at BaO/ BaO_2 sites and to a lesser extent on the $Ba(OH)_2$ and $BaCO_3$ sites [31-34]. Interaction between Ba-containing sites and the support material (Al_2O_3), as well as the interplay between Pt and Ba phases have significant effects not only on the thermal stability of barium containing sites but also on the reactivity of bulk and surface Ba phases towards NO_x storage [35]. A study done by Gilot et al. showed that proximity between the barium and Pt sites are critical for reactivity in NSR systems [36].

CeO_2 and ZrO_2 can be used in order to promote BaO storage phases in NSR catalysts [33, 34, 37-44]. Superior oxygen storage capacity and favorable redox properties of ceria exhibiting a cubic fluorite structure may enhance NO_x storage and reduction performance. Examples for the dynamic redox properties of ceria are given in the reactions below:

$$CeO_2 + x\,CO \rightarrow CeO_{2-x} + x\,CO_2 \qquad (14)$$

$$CeO_2 + HC \rightarrow CeO_{2-x} + (H_2O, CO_2, CO, H_2) \qquad (15)$$

$$CeO_2 + x\,H_2 \rightarrow CeO_{2-x} + x\,H_2O \qquad (16)$$

$$CeO_{2-x} + x\,NO \rightarrow CeO_2 + 0.5\,x\,N_2 \qquad (17)$$

$$CeO_{2-x} + x\,H_2O \rightarrow CeO_2 + x\,H_2 \qquad (18)$$

$$CeO_{2-x} + 0.5\,x\,O_2 \rightarrow CeO_2 \qquad (19)$$

One of our former studies showed the positive effect of ceria on Al, Ba/Al and Ba/Pt/Al catalysts regarding NSR catalysis, particularly NO_x reduction/regeneration in the presence of H_2 (g), under rich conditions. In the same study, increase in Pt dispersion after ceria addition was demonstrated along with strong metal support interaction (SMSI) between Ce and Pt sites and the formation of Pt-O-Ce sites[45].

Casapu et al. demonstrated the improvement in NO_x storage capacities of Pt-BaO/CeO_2 compared to Pt-BaO/Al_2O_3 benchmark catalysts [37]. It is well known in the literature that the formation of $BaAl_2O_4$ phase decreases the NSR performance of the benchmark catalyst (i.e. Pt-BaO/Al_2O_3) due to the blocking of the active Ba sites and need for high temperature regeneration. Whereas, regeneration ability of $BaCeO_3$ that suppresses the $BaAl_2O_4$ formation is much higher at low temperatures [46]. Another important property of ceria is related to Mars-Van Krevelen Mechanism of catalytic oxidations. CeO_2 can release its lattice oxygen in an oxygen deficient atmosphere and store oxygen in an oxygen excess environment. Giving lattice oxygen from the catalyst, which provides additional oxygen source for oxidation step, reveals formation of oxygen vacancies over ceria surfaces and that vacancy can be replenished by oxygen from the vapor phase (Figure 9).

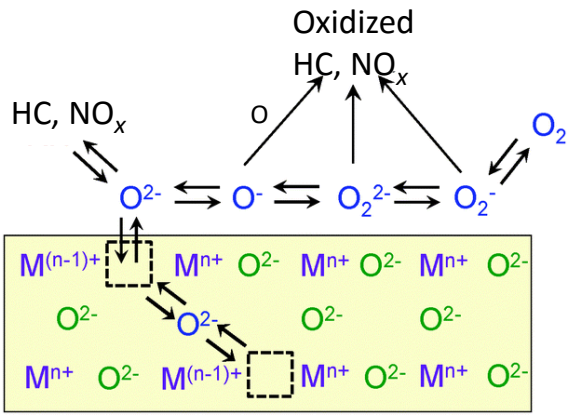

Figure 9. Depiction of the redox processes associated with the Mars and van Krevelen mechanism (Copyright © 2015 Elsevier. Reproduced with permission from [47].)

Degradation problem of ceria at high temperatures due to thermal sintering can be alleviated by zirconia doping. Mamontov and Egami investigated the temperature dependence of the crystallite growth for ceria-zirconia solid solutions and reported that presence of zirconia stabilizes the system against thermal aging [48]. In figure 10, positive effect of zirconia addition on the thermal stability of ceria phases can be realized by considering the limited crystal size variations in the CeO_2-ZrO_2 system with increasing temperature.

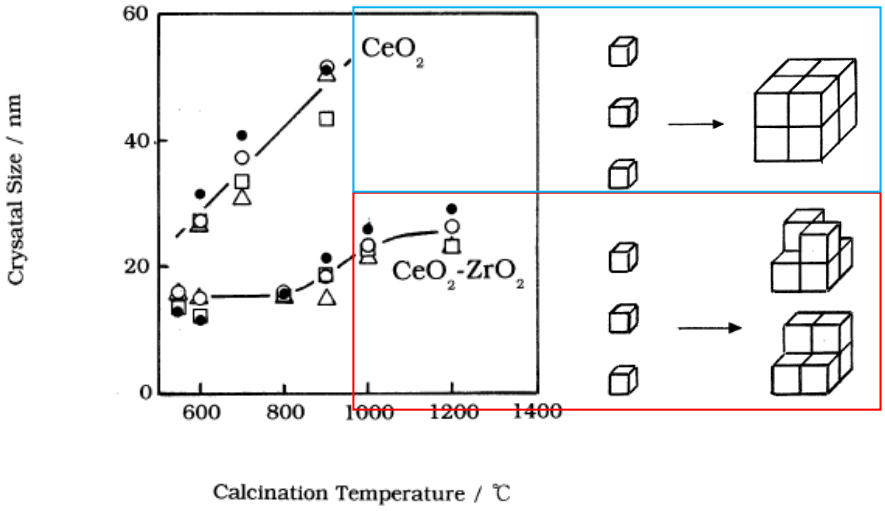

Figure 10. Effect of calcination temperature on the particle size growth on CeO_2 and CeO_2-ZrO_2 crystals (Copyright © 2000 Elsevier. Reproduced with permission from [48, 49].

ZrO_2 exhibits different crystal structures where the most common phases are monoclinic, tetragonal and cubic phases (Figure 11). At low temperatures, the most stable phase is the monoclinic structure, at ambient pressure and at 1478 K, tetragonal phase having high fracture resistance becomes thermodynamically more stable than the monoclinic system. At higher temperatures such as 2650 K, cubic zirconia phase forms exhibiting a higher refractive index [50, 51].

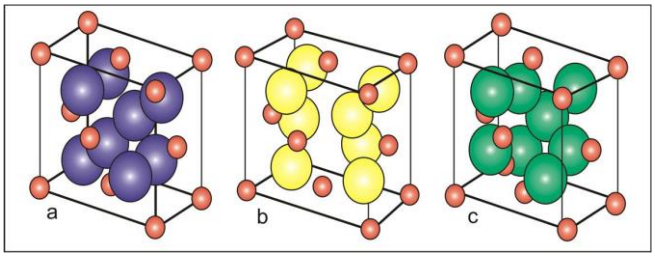

Figure 11. Crystal structures of (a)monoclinic, (b)tetragonal and (c) cubic zirconia polymorphs (Copyright © 2011 Elsevier [50, 51].)

Another significant point rendering zirconia a promising promoter for NSR catalysis is associated with its steam reforming capabilities. ZrO_2 can react with water and hydrocarbons in the exhaust stream to provide *on-board* H_2 which can function favorably as an additional reducing agent in DeNOx processes [52].

There is a wide variety of crystal structures available for Ce-Zr mixed oxide systems revealing a large number of non-equilibrium phases. One of the most commonly known examples of such systems is a *pyrochlore-like* structure, where Ce and Zr atoms are arranged regularly and oxygen vacancies are in the tedrahedral locations positioned between four Zr^{4+} or Ce^{4+} atoms as can be seen in Figure 12 [53, 54].

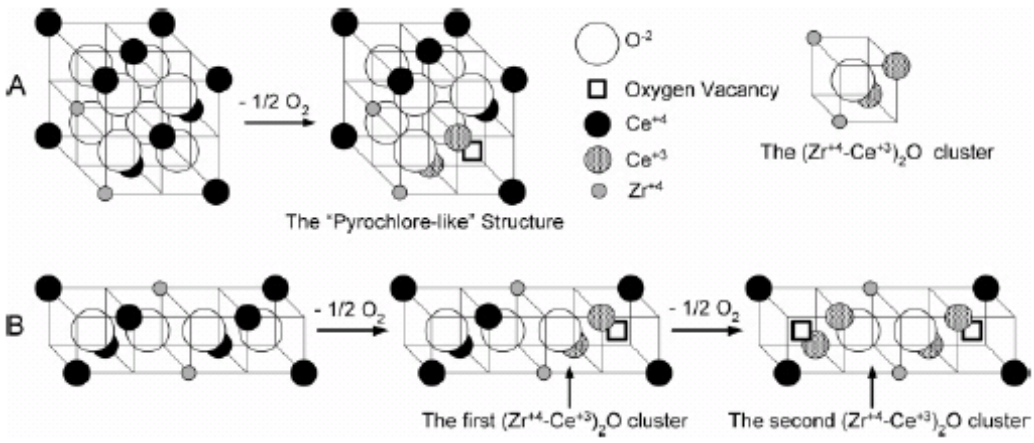

Figure 12. Schematic diagram showing a typical pyrochlore like Ce-Zr mixed oxide structure. (A) formation of the pyrochlore-like cluster. (B) two step reduction of Ce in the cluster. (Copyright © 2006 Elsevier [53].)

Incorporation of ceria with zirconia leads to the $Ce_{1-x}Zr_xO_2$ formation which can increase defect concentration and the metal dispersion on these surfaces [55, 56]. Wang et al. synthesized a series of $Pt/Ba/Ce_{0.6}Zr_{0.4}O_2$ catalysts and

demonstrated the improvement in the dispersion of Pt with the addition of $Ce_{0.6}Zr_{0.4}O_2$. They also stated that Pt/Ba/50 wt % Al_2O_3- 50 wt % $Ce_{0.6}Zr_{0.4}O_2$ catalyst showed good regeneration ability and superior NSR performance [56]. Baiker et al. studied the influence of support on thermal deterioration on Pt/Ba/ $Ce_{1-x}Zr_xO_2$. They reported the transformation of $BaCO_3$ into Ba zirconate and Ba cerate at 1073 K [57].

1.2.2. SO_x Poisoning Problem for NSR Catalysts

Sulfur species present in the fuel results in the accumulation of SO_x on NSR catalysts decreasing the NO_x storage capacity due to the blocking of active sites such as Pt and BaO. After the oxidation of SO_x on Pt, aluminum sulfates ($Al_2(SO_4)_3$) are formed, which can plug the ɣ-Al_2O_3 micropores that are important for NO_x adsorption [58]. Furthermore, SO_x species also react with BaO storage domains forming $BaSO_4$ [52, 54]. $BaSO_4$ is thermodynamically more stable than $Ba(NO_3)_2$, requiring higher temperatures for regeneration [59, 60]. However, regeneration at elevated temperatures are detrimental to the NSR systems due to sintering of the precious metals hindering the NO_x oxidation/reduction/sorption [26, 61]. BaO is strongly basic and thus prone to acidic SO_x species. Experiments done by Kim et al. showed that low BaO loadings (8 wt %) on the Pt-BaO/Al_2O_3 catalyst facilitates desulfation compared to higher BaO loadings (20 wt %) [62].

In order to reduce sulfur accumulation of NSR catalysts, CeO_2 and ZrO_2 can be used as promoters. Crocker et al. studied the desulfation characteristic of Pt-BaO-CeO_2-ZrO_2/Al_2O_3 catalyst and observed greater resistance against sulfur

poisoning and the ability to release sulfur at low temperatures [63]. As a reducing agent for sulfur, hydrogen is more efficient than carbon monoxide [64]. A series of Pt/Ba/ Al_2O_3- $Ce_{0.6}Zr_{0.4}O_2$ with different $Ce_{0.6}Zr_{0.4}O_2$ loadings were synthesized by Wang and Jiang et al. to investigate the effect of ceria-zirconia mixed oxide loading on sulfur poisoning and regeneration with H_2 (g) [56]. H_2-TPR experiments showed that Pt/Ba/ 50 wt% Al_2O_3- 50 wt% $Ce_{0.6}Zr_{0.4}O_2$ catalyst revealed better desulfation ability, strong resistance against SO_2 and superior NSR performance.

1.3. Formation of Nitrates and Sulfates

1.3.1. Nitrate (NO_3^-) Formation

Free nitrate ion (NO_3^-) has a trigonal planar geometry with a central nitrogen atom surrounded by three oxygen atoms. It has three different resonance arrangements. It has three IR active modes at 1430, 825 and 722 cm^{-1} [65]. On the other hand, free nitrite ion (NO_2^-) has two active IR bands at 1330 and 1260 cm^{-1} [66].

	ν_3 (cm^{-1})		ν_1 (cm^{-1})
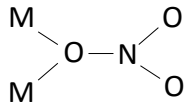	1530-1480	1290- 1250	1035- 970
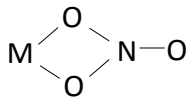	1565-1500	1300- 1260	1040- 1010
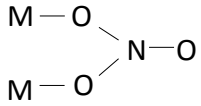	1650-1600	1225- 1170	1030- 1000
NO_3^- (free)	1380		1050

	ν_s (cm^{-1})	ν_{as} (cm^{-1})
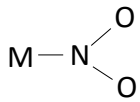	1440-1335	1350- 1315
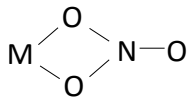	1565-1500	1040- 1010
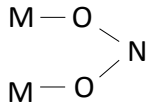	1220-1205	
	1470-1450	1065- 1050
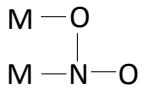	1520-1390	1260-1180
NO_2^- (free)	1260	1330

Figure 13. Stretching vibration frequencies of NO_3^- and NO_2^- in inorganic coordination compounds (Copyright © 2003 Wiley. Reproduced with permission from ref [67]).

Coordination of free nitrate ion to the adsorption site(s) on catalyst surface results in three different nitrate geometries namely; bridging nitrates, monodentate nitrates and bidentate nitrates as illustrated in Figure 14. These different

coordination types lead to different vibrational modes in FT-IR analysis. Bridging nitrates lead to vibrational features at 1000-1030 cm^{-1}, 1590-1660 cm^{-1}, and an asymmetric stretching mode at 1200-1260 cm^{-1}. Vibrational modes of monodentate nitrates can be observed at 1450-1570 cm^{-1}, 1250-1330 cm^{-1} and 970- 1035 cm^{-1}. Finally, bidentate nitrates symmetric stretching can be observed at 1003-1040 cm^{-1} while two other active IR modes appear at 1200-1310 cm^{-1} and 1500-1620 cm^{-1}. IR absorption bands of nitrites and nitrates overlap in the region of 1350-1550 cm^{-1} [65, 66, 68-70].

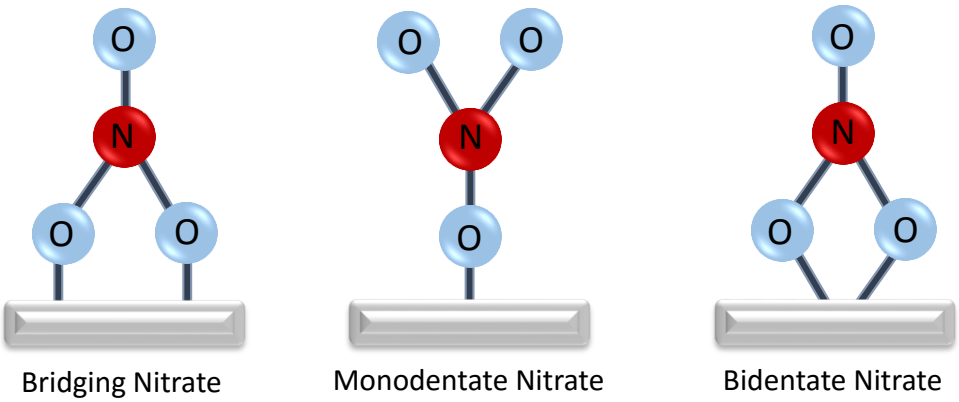

Figure 14. Different coordination types of adsorbed nitrates.

1.3.2. Sulfate (SO_4^{2-}) Formation

Free sulfate ion (SO_4^{2-}) has a tetrahedral geometry with a central sulfur atom possessing +6 oxidation state surrounded by four oxygen atoms. SO_4^{2-} species have IR active modes at 1440, 1240 and 925 cm^{-1}.

	ν_1 (cm^{-1})	ν_3 (cm^{-1})
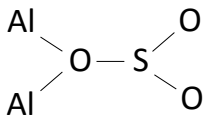	1140	1320- 1326
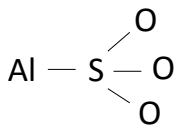	1050-1065	1135
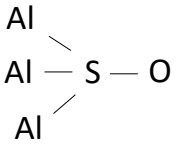	1145-1130	1380
$BaSO_4$ (surface)	1160	1120
$Ce(SO_4)_2$ (surface)	980	1340- 1400
$Al_2(SO_4)_3$ (bulk)	1190	
$BaSO_4$ (bulk)	1155,1248	
$Ce(SO_4)_2$ (bulk)	1145-1240	
SO_4^{2-} (free)		1104
SO_3^{2-} (free)	961	1010

Figure 15. Stretching vibration frequencies of SO_4^- and SO_3^- in inorganic coordination compounds (Copyright © 2012 Elsevier. Reproduced with permission from [71]).

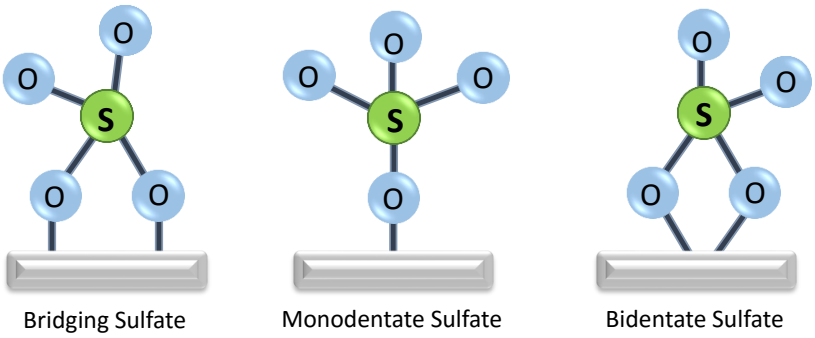

Figure 16. Different coordination types of adsorbed sulfates.

SO_2 coordinates to the metal atom in catalyst structure and forms different sulfates and sulfites such as bridging sulfates, monodentate sulfates, tridentate sulfates and bidentate sulfates. Vibrations of surface sulfates can be observed in the range of 1300- 1390 and 1010-1125 cm^{-1}, whereas surface sulfites can be seen at 1010-950 cm^{-1} [72-76].

Chapter 2

Experimental

2.1. Sample Preparation

2.1.1. Loadings of Individual Components in All of the Synthesized Samples

Weight percentage of the individual components in all of the synthesized catalysts and their abbreviations are listed in Table 2.

Table 2. Weight percent loadings of individual components in the synthesized samples.

Materials	Abbreviations	wt. % Pt	wt. % BaO	wt. % CeO_2	wt. % ZrO_2	wt. % Al_2O_3
$Pt/BaO/Al_2O_3$	Pt20BaAl	1	20	0	0	79
$Pt/CeO_2/Al_2O_3$	Pt20CeAl	1	0	20	0	79
$Pt/ZrO_2/Al_2O_3$	Pt20ZrAl	1	0	0	20	79
$Pt/CeO_2/ ZrO_2/Al_2O_3$	Pt10Ce10ZrAl	1	0	10	10	79
$Pt/ZrO_2/ CeO_2/Al_2O_3$	Pt10Zr10CeAl	1	0	10	10	79
$Pt/CeO_2 - ZrO_2/Al_2O_3$	Pt10-10CeZrAl	1	0	10	10	79
$Pt/8BaO/CeO_2 - ZrO_2 /Al_2O_3$	Pt8Ba10-10CeZrAl	1	8	10	10	71
$Pt/20BaO/CeO_2 - ZrO_2 /Al_2O_3$	Pt20Ba10-10CeZrAl	1	20	10	10	59
$Pt/CeO_2 - ZrO_2 /8BaO/Al_2O_3$	Pt10-10CeZr8BaAl	1	8	10	10	71
$Pt/CeO_2 - ZrO_2 /20BaO/Al_2O_3$	Pt10-10CeZr20BaAl	1	20	10	10	59

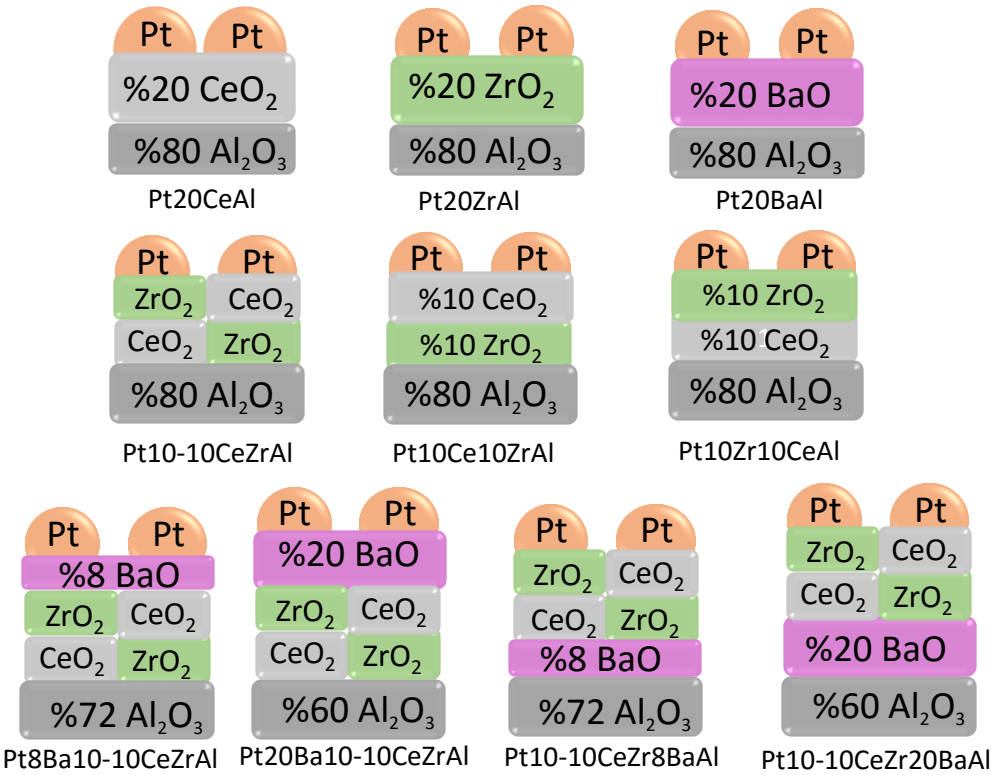

Figure 17. General synthesis strategy employed in the preparation of the currently investigated catalysts emphasizing the variations in the order of impregnation of various oxide sub-components.

2.1.2. Synthesis of Pt/20BaO/Al_2O_3 Benchmark NSR Catalyst

Pt/20BaO/Al_2O_3 benchmark catalyst was synthesized via wetness impregnation method. Firstly, 4.8 g of ɣ-Al_2O_3 (SASOL, Puralox SBa200) precursor was mixed with 30 ml of deionized water. After 10 min of stirring, 2.05 g of barium nitrate ($Ba(NO_3)_2$, Sigma Aldrich, 99%) and 20 ml of deionized water were added over ɣ-Al_2O_3 solution. Then, the solution was stirred for 6 h at *ca.* 350 K. After the drying process, sample was calcined at 873 K for 120 min. Next, 1 wt

% of Pt $(NH_3)_2(NO_2)_2$ (Diammine Dinitritoplatinum (II), Sigma Aldrich, 3.4 wt % in dilute ammonium hydroxide) was impregnated onto the calcined BaO/Al_2O_3 sample with 50 ml of deionized water. In the final calcination step, the sample was calcined at 973 K for 150 min. This sample will be referred as Pt20BaAl in the forthcoming text.

2.1.3. Synthesis of $Pt/CeO_2/Al_2O_3$

4.8 g of ɣ-Al_2O_3 (SASOL, Puralox SBa200) precursor was added to 30 ml of deionized water. After 10 min of stirring the ɣ-Al_2O_3 aqueous suspension, 3.03 g of cerium (III) nitrate hexahydrate (CeN_3O_9. $6H_2O$, Sigma Aldrich, 99%) and 20 ml of deionized water were added to the mixture. Then, the mixture was stirred for 6 h at *ca.* 350 K. After the drying process, the sample was calcined at 873 K for 120 min under ambient conditions. This step was followed by 1 wt % of Pt $(NH_3)_2(NO_2)_2$ (Diammine Dinitritoplatinum (II), Sigma Aldrich, 3.4 wt % in dilute ammonium hydroxide) addition onto the calcined CeO_2/ Al_2O_3 sample with 50 ml of deionized water. Finally, the sample was calcined at 973 K for 150 min. This sample will be named as Pt20CeAl hereafter.

2.1.4. Synthesis of $Pt/ZrO_2/Al_2O_3$

Pt/ZrO_2/ Al_2O_3 sample was synthesized by using wetness impregnation method as well. 4.8 g of ɣ-Al_2O_3 (SASOL, Puralox SBa200) was mixed with 30 ml of deionized water. After 10 min of stirring, 2.25 g of zirconium (IV) oxynitrate hydrate ($N_2O_7Zr.xH_2O$, Sigma Aldrich 99%) and 20 ml of deionized

water were added to the mixture. Then, the solution was stirred for 6 h at *ca.* 350 K. After the drying process, the sample was calcined at 873 K for 120 min. In the next step, 1 wt % of Pt $(NH_3)_2(NO_2)_2$ (Diammine Dinitritoplatinum (II), Sigma Aldrich, 3.4 wt % in dilute ammonium hydroxide) was impregnated onto the calcined ZrO_2/Al_2O_3 sample with 50 ml of deionized water. In the final calcination step, the sample was calcined at 973 K for 150 min. This sample will be abbreviated as Pt20ZrAl, in the rest of the text.

2.1.5. Synthesis of CeO_2-ZrO_2 Mixed Metal Oxide Materials

2.1.5.1. Synthesis of Pt/CeO_2/ZrO_2/Al_2O_3 Materials

CeO_2-ZrO_2 mixed metal oxide materials were also synthesized by wetness impregnation method. Synthesis protocol was started by mixing 4.8 g of ɣ-Al_2O_3 (SASOL, Puralox SBa200) with 30 ml of deionized water for 10 min. Then, 1.13 g of zirconium (IV) oxynitrate hydrate ($N_2O_7Zr.xH_2O$, Sigma Aldrich 99%) and 20 ml of deionized water were added to the mixture. Next, the mixture was stirred for 6 h at *ca.* 350 K. After the drying process, the sample was calcined at 873 K for 120 min. In the next step, calcined ZrO_2/Al_2O_3 was stirred with 30 ml deionized water about 10 min and then 1.51 g of cerium(III) nitrate hexahydrate (CeN_3O_9. $6H_2O$, Sigma Aldrich, 99%) and 20 ml of deionized water were added. Then, the mixture was stirred for 6 h at *ca.* 350 K. After the drying step, the sample was calcined again at 873 K for 120 min. Then, 1 wt % of $Pt(NH_3)_2(NO_2)_2$ (Diammine Dinitritoplatinum(II),Sigma Aldrich, 3.4 wt % in dilute ammonium hydroxide) was added to calcined $CeO_2/ZrO_2/Al_2O_3$ sample with 50 ml of

deionized water. Finally, the sample was calcined at 973 K for 150 min. This sample will be abbreviated as Pt10Ce10ZrAl in the text.

2.1.5.2. Synthesis of Pt/ZrO_2/CeO_2/Al_2O_3 Materials

In the first step, 4.8 g of ɣ-Al_2O_3 (SASOL, Puralox SBa200) was mixed with 30 ml of deionized water. After stirring about 10 min without heating, 1.51 g of cerium(III) nitrate hexahydrate (CeN_3O_9. $6H_2O$, Sigma Aldrich, 99%) was impregnated over ɣ-Al_2O_3 and 20 ml of deionized water was added. The solution was stirred at *ca.* 350 K for 6 h. After drying, the sample was calcined at 873 K for 120 min under ambient conditions. In the following step, calcined CeO_2/Al_2O_3 sample was mixed with 30 ml deionized water about 10 min and then 1.13 g of zirconium(IV) oxynitrate hydrate ($N_2O_7Zr.xH_2O$, Sigma Aldrich 99%)and 20 ml of deionized water were added respectively. Then, the solution was stirred for 6 h at *ca.* 350 K. After the drying process, the sample was calcined again at 873 K for 120 min. Next, 1 wt % of $Pt(NH_3)_2(NO_2)_2$ (Diammine Dinitritoplatinum(II),Sigma Aldrich, 3.4 wt % in dilute ammonium hydroxide) was added to calcined ZrO_2/CeO_2/Al_2O_3 sample with 50 ml of deionized water. Final calcination tesp was performed at 973 K for 150 min. This sample will be called Pt10Zr10CeAl in the rest of the text.

2.1.5.3. Synthesis of Pt/CeO_2 – ZrO_2/Al_2O_3 Materials

4.8 g of ɣ-Al_2O_3 (SASOL, Puralox SBa200) was mixed with 30 ml of deionized water. After stirring about 10 min without heating, 1.51 g of cerium

(III) nitrate hexahydrate (CeN_3O_9. $6H_2O$, Sigma Aldrich, 99%) and 1.13 g of zirconium(IV) oxynitrate hydrate($N_2O_7Zr.xH_2O$, Sigma Aldrich, 99%) were added to the mixture at the same time. After the addition of 20 ml of deionized water, the mixture was stirred at *ca.* 350 K for 6 h. After drying, obtained powder was calcined at 873 K for 120 min. Then, 1 wt % of Pt $(NH_3)_2(NO_2)_2$ (Diammine Dinitritoplatinum (II), Sigma Aldrich, 3.4 wt % in dilute ammonium hydroxide) was impregnated onto the calcined CeO_2 - ZrO_2/Al_2O_3 sample with 50 ml of deionized water. Finally, the sample was calcined at 973 K for 150 min. This sample will be called Pt10-10CeZrAl hereafter in the text.

2.1.6. Synthesis of BaO-CeO_2 - ZrO_2 Mixed Metal Oxide Materials

2.1.6.1. Synthesis of Pt/BaO/CeO_2 - ZrO_2 /Al_2O_3 Materials

In the synthesis of Pt/BaO/CeO_2-ZrO_2 /Al_2O_3 materials, two different amounts of BaO precursors were added over the co-impregnated CeO_2 - ZrO_2 /Al_2O_3 mixed metal oxide materials. Firstly, calcined CeO_2 - ZrO_2 /Al_2O_3 material was added to 30 ml of deionized water and stirred about 10 min without heating. Then, needed amounts of barium nitrate (Ba $(NO_3)_2$, Sigma Aldrich, 99%) and 20 ml of deionized water were added to the mixture. The amounts of the Ba precursors to obtain 20 wt% and 8 wt% BaO impregnated materials were 1.93 g and 0.77 g, respectively. After stirring for 6 h at *ca.* 350 K, the samples became completely dry. Afterwards, the samples were calcined at 873 K for 120 min. In the next step, 1 wt % of Pt $(NH_3)_2(NO_2)_2$ (Diammine Dinitritoplatinum (II), Sigma Aldrich, 3.4 wt % in dilute ammonium hydroxide) was impregnated to calcined

BaO/CeO_2-ZrO_2/Al_2O_3 samples with 50 ml of deionized water. In the final calcination step, the samples were calcined at 973 K for 150 min. These samples were named as Pt8Ba10-10CeZrAl and Pt20Ba10-10CeZrAl in the text.

2.1.6.2. Synthesis of Pt/CeO_2 - ZrO_2 /BaO/Al_2O_3 Materials

For the synthesis of Pt/CeO_2-ZrO_2 /BaO/Al_2O_3 materials, first step was the synthesis of BaO/Al_2O_3 materials. The amounts of the Ba precursors (i.e. barium nitrate ($Ba(NO_3)_2$, Sigma Aldrich, 99%) to obtain 20 wt% and 8 wt% BaO impregnated materials were 2.04 g and 0.82 g, respectively. After the calcination of BaO/Al_2O_3 materials at 873 K for 120 min, calcined samples were mixed with 30 ml of deionized water and stirred about 10 min without heating. Then, 1.51 g of cerium (III) nitrate hexahydrate (CeN_3O_9. $6H_2O$, Sigma Aldrich, 99%) and 1.13 g of zirconium (IV) oxynitrate hydrate ($N_2O_7Zr.xH_2O$, Sigma Aldrich, 99%) were added over the mixture at the same time. After the addition of 20 ml of deionized water, the mixtures were stirred at *ca.* 350 K for 6 h. After drying, samples were calcined at 873 K for 120 min. In the following step, 1 wt % of Pt $(NH_3)_2(NO_2)_2$ (Diammine Dinitritoplatinum (II), Sigma Aldrich, 3.4 wt % in dilute ammonium hydroxide) was impregnated onto the calcined BaO/CeO_2 - ZrO_2 /Al_2O_3 sample with 50 ml of deionized water. Finally, the samples were calcined at 973 K for 150 min. These samples were abbreviated as Pt10-10CeZr8BaAl and Pt10-10CeZr20BaAl in the text.

2.2. Instrumentation & Measurement Techniques

2.2.1. Structural Characterization

2.2.1.1. X-ray Diffraction (XRD) Analysis

XRD patterns of the powder samples were recorded by using a Rigaku diffractrometer that has a Miniflex goniometer and an X-ray source with Cu Kα radiation at λ= 1.5418 Å kV and 15 mA. Powder samples were packed into a standard-sized quartz slides and were scanned in the 2θ range of 10-80° with 0.01^{o} s $^{-1}$ scan rate. Diffraction patterns were assigned by using Joint Committee on Powder Diffraction Standards (JCPDS).

2.2.1.2. Brunauer Emmett Teller (BET) Surface Area Analysis

Five point BET experiments were performed after dehydration process at 573 K for 120 min in vacuum. Specific surface areas were measured by using a Micromeritics ASAP 2000 N_2 sorption system.

2.2.2. Functional Characterization

2.2.2.1. FT-IR Spectroscopy

Adsorption and desorption experiments were carried out by using an transmission in-situ FTIR spectrometer (Bruker Tensor 27) that was combined with a custom-made batch mode spectroscopic cell. In-situ FT-IR system was coupled to a quadruple mass spectrometer (QMS, Stanford Research Systems,

SRS RGA200) with a QMS filament made of thoria-coated iridium for temperature programmed desorption (TPD) experiments as illustrated in Figure 18.

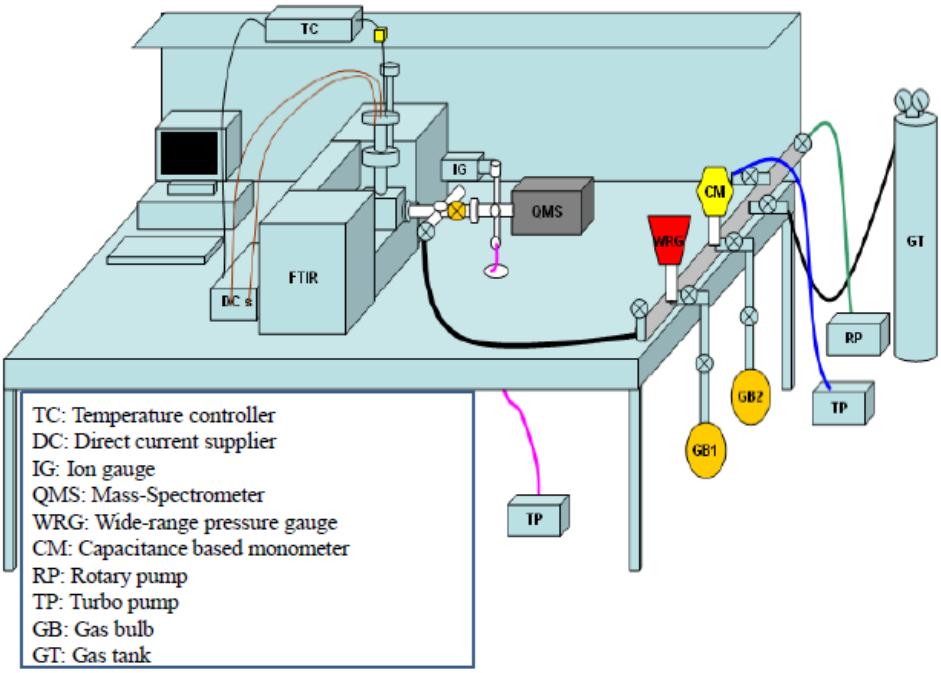

Figure 18. Schematic diagram of *in-situ* FTIR and TPD analysis system [77].

Materials were placed in a custom-designed in-situ FTIR spectroscopic cell that has a home-made K-type thermocouple (alumel and chromel, with 0.015 thickness, Omega Engineering, Inc.), high purity tungsten grid (TechEtch, USA, P/N PW10379-003) and cupper legs. Powder catalysts within a mass range of 16-22 mg were pressed onto the etched W-grid by applying 3 ton of pressure. Temperature of the catalysts was controlled by the computer controlled heating system, designed to work within 273- 1273 K, including a PID-controller (Gefran 600-DRRR) and a DC power supply. During the experiments, pressed samples

can be heated between 323-1023 K with a linear heating rate of 12 K/min. All in-situ FTIR spectra were collected at 323 K by using a liquid nitrogen cooled MCT (Hg-Cd-Te) mid-IR detector with a resolution of 4 cm^{-1} and 128 scans. In order to control pressures, a MKS Baratron Pressure Transducer Type 626 and a combined wide range pressure gauge (EDVAC WRG-S-NW35) were used.

2.2.2.2. Temperature Programmed Desorption (TPD)

Temperature Programmed Desorption (TPD) is a technique that monitors the evolution of the species from the materials' surface back into the gas phase by heating the sample with a controlled linear heating rate. Common detector for TPD analysis is a quadruple mass spectrometer (QMS) that gives a plot of the signal as a function of the mass to charge (m/z) ratios. These spectra can be used to understand the amount of adsorbed species and the strength of binding to the surface. For temperature programmed desorption (TPD) experiments, quadruple mass spectrometer (QMS, Stanford Research System, RGA200) was used. By using DC power supply and PID electronics (Gefran 600-DRRR) catalysts were heated linearly within the range of 323- 1023K with 12 K/min ramping rate.

2.2.3. Experimental Procedures

Before the *in-situ* FT-IR and TPD experiments, a pretreatment protocol was applied for all samples in order to clean the material surfaces. Calcined samples were pressed onto the tungsten grid and assembled on the sample holder. Then, the samples were annealed at 403 K for 12 h in vacuum to eliminate the

water on the catalyst surfaces and the reactor walls. After cooling the sample to 323 K, material surfaces were flushed with 0.5 Torr of NO_x (g) (NO_2 gas prepared by mixing NO(g) (Air Products, 99.9%) and excess O_2 (Linde GmbH, 99.999%) for 5 min at 323 K and subsequently annealed to 973 K with a 12 K/min linear heating rate under vacuum. Materials were kept 973 K for 3 min and then cooled to 323 K.

2.2.3.1. NO_x Adsorption Experiments *via in-situ* FTIR

In stepwise NO_2 adsorption experiments, two successive exposures of 0.5 Torr NO_2 (g) (NO_2 gas prepared by mixing NO (g) (Air Products, 99.9%) and excess O_2 (Linde GmbH, 99.999 %) was introduced on the samples at 323 K followed by eight steps of 1.0 Torr of NO_2 (g) at 323 K where each exposure lasted for 1 min. After 1 min, the gas was evacuated from the IR cell to a pressure lower than 10^{-2} before taking an in-situ FTIR spectrum. After these subsequent steps, 5.0 Torr NO_2 (g) was exposed over the surface at 323 K for 10 min in order to saturate the catalyst surface with NO_x.

2.2.3.2. NO_x Desorption and Reduction in H_2 Atmosphere *via in-situ* FTIR

After stepwise NO_x adsorption experiments, NO_2 saturated sample surface was exposed to 15.0 Torr H_2 (g) (Linde GmbH, > 99.9%) and sample was held 2 h in H_2 (g) environment. The time- dependent spectra were taken for 120 min at 323 K. After 120 min, the samples were heated to 473, 573 and 673 K in the presence

of H_2 (g) and spectra were taken after each heating step followed by cooling to 323 K.

2.2.3.3. NO_x Desorption Experiments *via* TPD

After NO_x adsorption and reduction experiments, reduced sample surfaces were exposed to 5.0 Torr NO_2 (g) for 10 min to saturate the surfaces with NO_x. Upon evacuation of the gases in the reactor, in-situ FTIR spectra were acquired before the TPD analysis. After 40 mins of outgassing, materials were heated to 973 K with a linear rate of 12 K/min in vacuum where the TPD data were acquired. In TPD experiments, a Quadruple Mass Spectrometer (QMS) was used to monitor desorption patterns of the adsorbates. For NO_x TPD experiments, recorded m/z desorption channels were: 14 (N), 28 (N_2 or CO), 30 (NO), 44 (N_2O), 46 (NO_2). In-situ FTIR data were recorded also after the TPD experiments. By comparing two different FTIR spectra, residual amount of nitrate/nitrite species on the material surfaces can be understood.

2.2.3.4. SO_x Adsorption Experiments *via in-situ* FTIR

2.0 Torr SO_2 + O_2 gas mixture (SO_2 : O_2 = 1:10) (SO_2 Air Products >99%; O_2, Linde GmbH >99.999%) were introduced over the catalyst surfaces at 323 K and samples were heated to different temperatures for 5 min in the presence of this gas mixture. After waiting for 5 mins at each temperature, samples were cooled to 323 K, and FTIR spectra were obtained at 323 K in the presence of the gas mixture.

2.2.3.5. SO_x Regeneration Experiments with H_2(g) *via in-situ* FTIR

After SO_x adsorption experiments, 15.0 Torr H_2 (g) (Linde GmbH, > 99.9%) was introduced over the sulfur-poisoned sample surfaces at 323 K. Then samples were annealed step by step at 473, 573, 673, 773, 873 and 973 K in H_2 (g) atmosphere and kept for 5 min at each temperature. Between each step, materials were cooled to 323 K, and FTIR spectra were recorded in H_2 (g) atmosphere to understand the regeneration abilities of the catalysts.

2.2.3.6. SO_x Desorption Experiments *via* TPD

After the pretreatment process, 2.0 Torr SO_2 + O_2 (g) mixture was dosed over the catalyst surfaces and samples were heated up to 673 K and kept for 30 mins at that temperature. After cooling the sample to 323 K, FTIR spectra were obtained before TPD analysis. After evacuation of the gases inside the reactor to < 10^{-3} Torr, materials were outgassed for 40 min; then they were heated up to 1173 K under vacuum with a 12 K/min linear heating rate. After cooling the sample to 323 K, FTIR spectra were acquired. In the SO_x TPD experiments, m/z desorption channels at 32 (O_2) and 64 (SO_2) were recorded.

Chapter 3

Results and Discussion

3.1. Structural Characterization

3.1.1. XRD Analysis

XRD profiles of binary, ternary and quaternary oxides are presented in Figures 19, 20, and 21, respectively. After calcination at 973 K, crystallization can be observed for all materials. For the Zr-containing samples, tetragonal ZrO_2 (JCPDS 80-2155) peaks cannot be seen easily suggesting a rather disordered structure. As can be seen in Figure 19, Pt20BaAl conventional catalyst reveals the formation of undesired $BaAl_2O_4$ (JCPDS 017-0306) which is known to decrease the NO_x storage capacity. Cubic ceria peaks (JCPDS 004-0593) can be observed for Pt20CeAl sample and peaks belong to γ-Al_2O_3 (JCPDS 001-1303) can be seen for all synthesized samples.

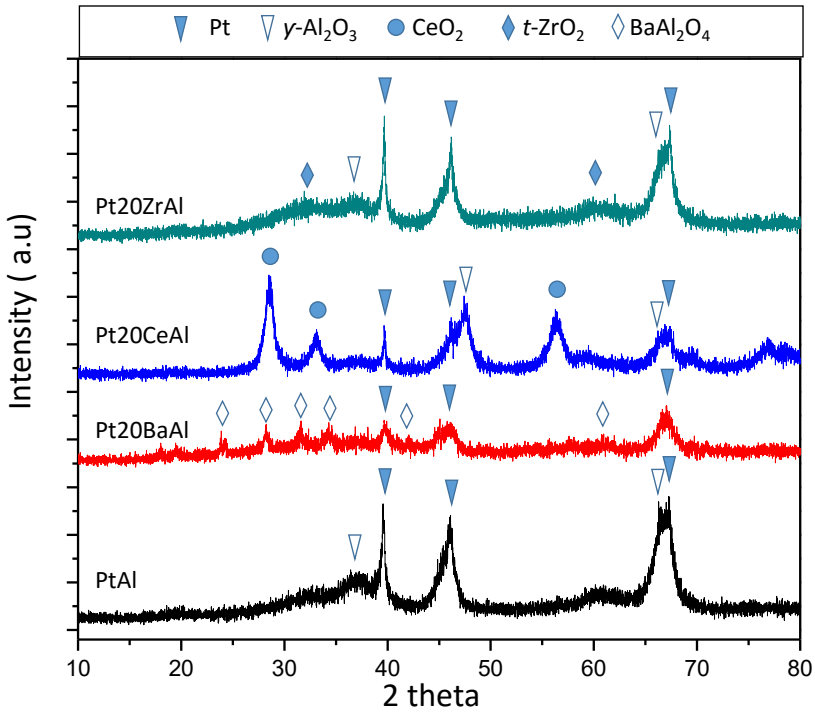

Figure 19. XRD patterns of PtAl, Pt20BaAl, Pt20CeAl and Pt20ZrAl materials (i.e. binary oxides) upon calcination at 973 K.

Structural aspects of ternary oxides as a function of synthesis method are illustrated in Figure 20 via XRD data. It is apparent that the impregnation order of the subsequent precursors or co-impregnation protocol does not yield significant differences in the XRD profiles of the ternary oxides (Figure 20).

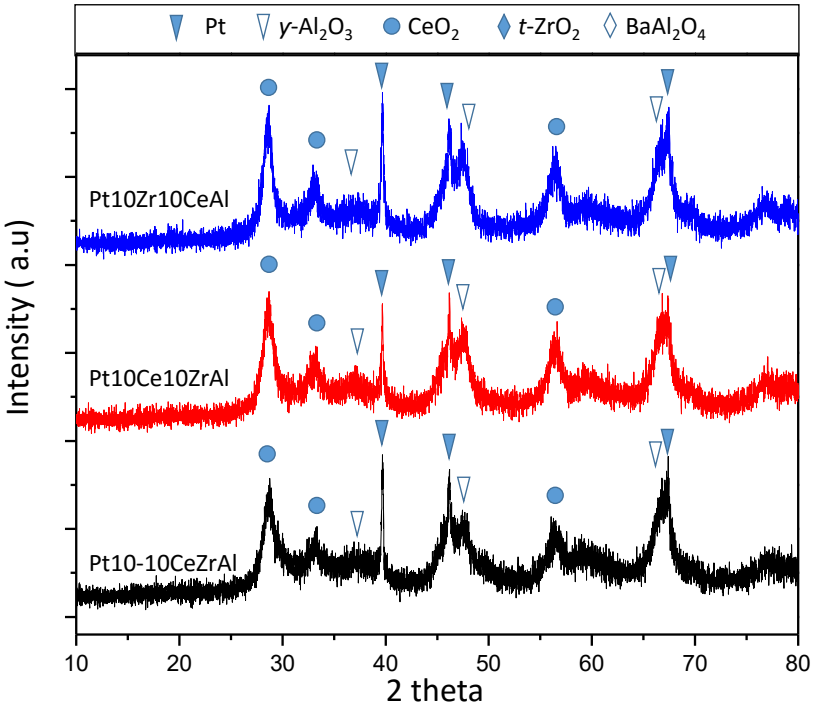

Figure 20. XRD patterns of Pt10-10CeZrAl, Pt10Ce10ZrAl and Pt10Zr10CeAl materials (i.e. ternary oxides) upon calcination at 973 K.

Figure 21 illustrates the XRD patterns of quaternary oxides including Ba functionalized Ce-Zr mixed metal oxide samples with 8 and 20 wt. % BaO loadings. Presence of CeO_2 (JCPDS 004-0593), t-ZrO_2 (JCPDS 80-2155) and ɣ-Al_2O_3 (JCPDS 001-1303) features are visible in all of the quarternary mixed oxides. Formation of $BaAl_2O_4$ (JCPDS 017-0306) can be observed only for high BaO (20 wt. %) loading samples but with lower intensities as compared to the Pt20BaAl sample. Unlike the Pt20BaAl benchmark catalyst, minor diffraction peaks corresponding to $BaCO_3$ (JCPDS 005-0378) were observed for BaO impregnated Ce-Zr mixed metal oxides. It is known that high thermally stable $BaCO_3$ may have a negative effect on NO_x storage Capacity (NSC)[78]. ICDD

card numbers of all of the crystalline phases detected in Figures 19-21 are also given in Figure 22.

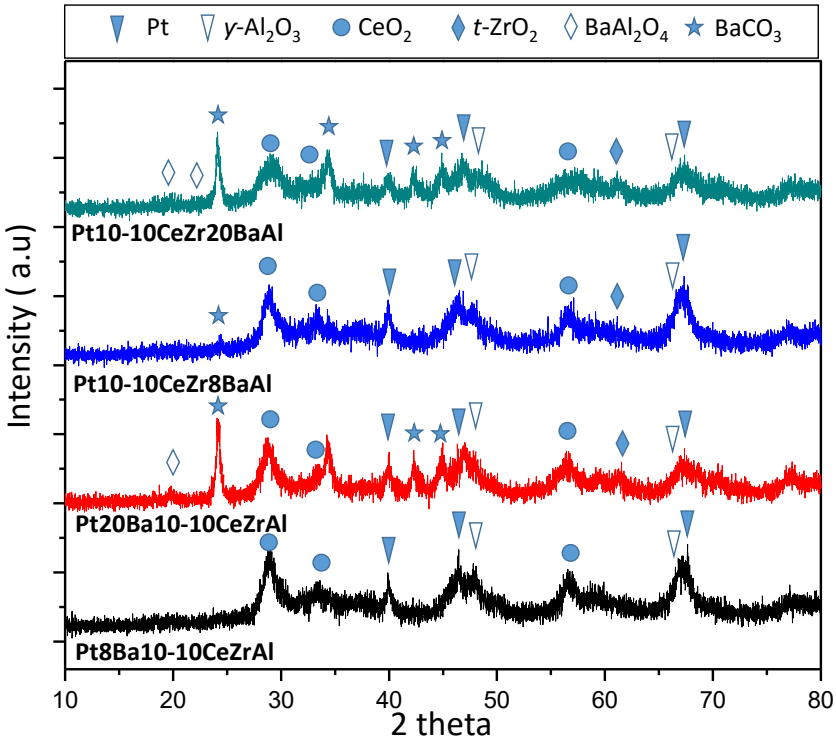

Figure 21. XRD patterns of Pt8Ba10-10CeZrAl, Pt20Ba10-10CeZrAl, Pt10-10CeZr8BaAl and Pt10-10CeZr20BaAl materials (i.e. quaternary oxides) upon calcination at 973 K.

ICDD RDF - CARD NO	
Pt(metallic)	JCPDS 004-0802
y-Al_2O_3	JCPDS 001-1303
CeO_2	JCPDS 004-0593
t-ZrO_2	JCPDS 80-2155
$BaAl_2O_4$	JCPDS 017-0306
$BaCO_3$	JCPDS 005-0378

Figure 22. JCPDS card number codes for some of the major features observed in XRD patterns.

Diffraction features belong to metallic Pt (JCPDS 004-0802) can be observed from the XRD patterns. In order to understand Pt dispersion differences between the catalysts, average Pt particle sizes of the synthesized catalysts were estimated by using Schrerrer Equation given below:

$$D_p = \frac{0.94\lambda}{\beta_{1/2}\cos\theta}$$

Where Dp = Average Crystallite size,
β = Line broadening in radians.
ϑ = Bragg angle.
λ = X-ray wavelength

Equation 1. Schrerrer equation [79].

Table 3. Average Pt particle sizes of the synthesized catalysts calculated using the XRD data by Schrerrer equation.

Sample Name	Full-Width Half Maxima(^{o})	Peak Position (^{o})	D_c Average Particle Size(nm)
Pt20BaAl	0.7	39.76	13 nm
Pt20CeAl	0.16	39.71	55 nm
Pt20ZrAl	0.21	39.67	42 nm
Pt10-10CeZrAl	0.22	39.70	40 nm
Pt10Ce10ZrAl	0.17	39.70	52 nm
Pt10Zr10CeAl	0.28	39.66	32 nm
Pt10-10CeZr8BaAl	0.46	39.93	19 nm
Pt10-10CeZr20BaAl	0.68	39.90	13 nm
Pt8Ba10-10CeZrAl	0.33	39.96	27 nm
Pt20Ba10-10CeZrAl	0.37	40.00	24 nm

It can be readily seen from the table, Pt20BaAl and Pt10-10CeZr20BaAl samples have the smallest average Pt particle sizes, which can also be observed from the broadening of the main peak of metallic Pt (2θ=40°) in XRD patterns. Impregnation of BaO on co-impregnated Ce-Zr mixed metal oxide systems seems to facilitate the Pt dispersion and decrease average Pt particle size.

3.1.2. BET Analysis

Specific surface areas (SSA) of binary, ternary and quaternary oxides calcined at 973 K were analyzed by BET, and the SSA values are given in Figure 23. Except for the high BaO laoding co-impregnated Ce-Zr mixed metal oxide catalysts, SSA values of all catalysts are comparable to each other. For binary oxides, Pt20ZrAl sample has a slightly higher SSA value than Pt20BaAl and Pt20CeAl samples. BET measurements indicated that sequential impregnation and co-impregnation of CeO_2 and ZrO_2 does not result in a drastic change in SSA values.

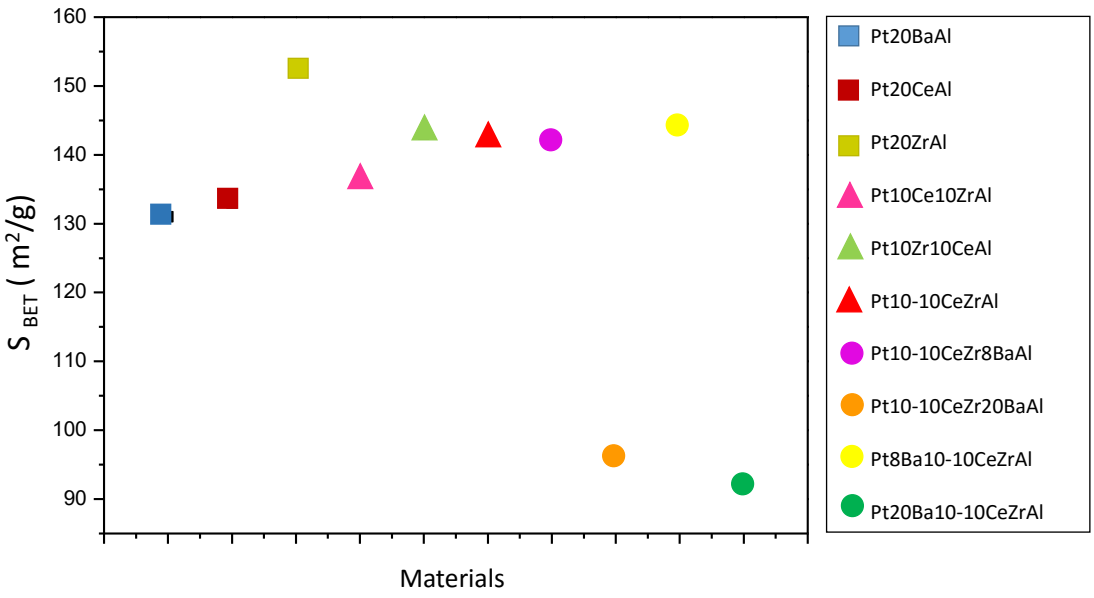

Figure 23. SSA values for the synthesized catalysts.

SSA values for 8 wt. % BaO catalysts, Pt10-10CeZr8BaAl and Pt8Ba10-10CeZrAl, were found to be 142 and 144 m^2/g, respectively. On the other hand, SSA values for the catalysts enriched by high BaO loadings, Pt10-10CeZr20BaAl and Pt20Ba10-10CeZrAl, were measured to be 97 and 92 m^2/g, respectively.

These results reveal that as Ba loading increases, the specific surface area of the catalysts decreases. Such a decrease in SSA values can be correlated with the negative effect of excess BaO leading to sintering and filling of the pores of the catalysts.

3.2. NO_x Adsorption *via in-situ* FTIR: Elucidation of NO_x Uptake and Storage Pathways

3.2.1. NO_x Adsorption on Binary Oxides *via in-situ* FTIR

Figure 24 shows *in-situ* FT-IR results of NO_x adsorption on conventional Pt20BaAl, catalyst, which was pretreated with 0.5 Torr NO_2 (g) and annealed 3 min at 973 K, as described in section 2.2.4. Five different vibrational features at 1632, 1567, 1433, 1330 and 1256 cm^{-1} and additional vibrational features within 1000-1080 cm^{-1} that can be associated with the symmetric, asymmetric and bending modes of monodentate, bridged and bidentate nitrates were detected for Pt20BaAl [80]. The frequencies at 1632 and 1256 cm^{-1} can be assigned to bridging nitrates, and the vibrational frequency at 1567 cm^{-1} can be attributed to bidentate nitrates [66], [65], [68], [69], [81]. Additionally, the frequencies at 1433 and 1330 cm^{-1} indicate the formation of bulk/ionic type of nitrates [80].

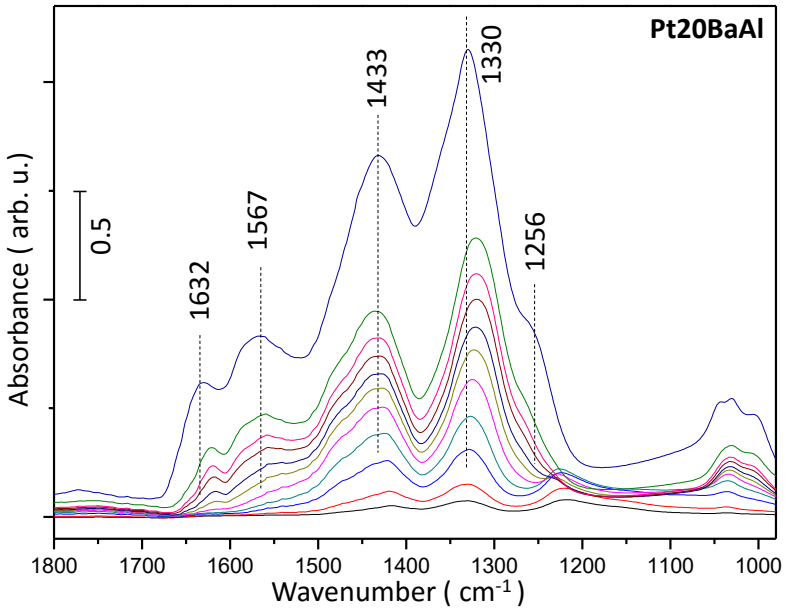

Figure 24. In-situ FTIR spectra for stepwise NO_x adsorption on Pt20BaAl, benchmark catalyst, at 323 K. The top spectrum was recorded after achieving surface saturation with 5.0 Torr of NO_2 (g) for 10 min at 323 K.

FTIR spectra for NO_2 (g) adsorption on (a) Pt20CeAl and (b) Pt20ZrAl were illustrated in Figure 25. Four vibrational features that can be assigned to formation of surface nitrates were observed for both Ce and Zr binary oxides. The features at 1630 and 1254 cm^{-1} for Pt20CeAl and 1635 and 1253 cm^{-1} for Pt20ZrAl can be attributed to bridging nitrates and the features at 1590 cm^{-1} can be ascribed to the bidentate nitrates [82], [45]. Finally, the features at 1296 and 1301 cm^{-1} can be assigned to monodentate nitrates [45, 81]. The absence of a signal around 1430 cm^{-1} for Pt20CeAl and Pt20ZrAl catalysts is a sign for the lack of bulk/ionic like nitrates formation, unlike the conventional catalyst,Pt20BaAl.

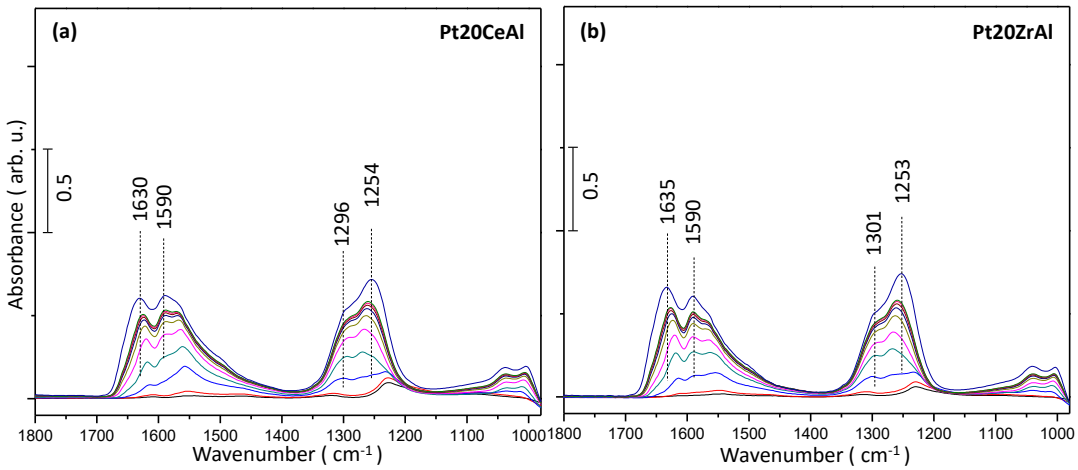

Figure 25. In-situ FT-IR spectra for stepwise NO_x adsorption of (a) Pt20CeAl and (b) Pt20ZrAl catalysts at 323 K. The top spectra were recorded after achieving surface saturation with 2.0 Torr of NO_2 (g) for 10 min at 323 K.

Similar NO_x adsorption geometries for Pt20CeAl and Pt20ZrAl and almost identical absorbance intensities can correspond to similar NSC. On the other hand, one needs to be careful in terms of comparing IR intensities and surface coverages of different adsorbates, as the correlation between these two entities are often not linear. Thus, in order to make a semi-quantitative comparison of NSC, NO_x TPD experiments were also performed which will be described in section 3.4.

3.2.2. NO_x Adsorption on Ternary Oxides *via in-situ* FTIR

Stepwise NO_2 adsorption experiments were also performed on ternary oxides and the results are illustrated in Figure 26 for Pt10-10CeZrAl and in Figure 27 for Pt10Ce10ZrAl and Pt10Zr10CeAl. Note that the Pt10-10CeZrAl was synthesized by using co-impregnation (i.e. simultaneous impregnation) method,

while Pt10Ce10ZrAl and Pt10Zr10CeAl were synthesized via a sequential impregnation protocol, as described in section 2.1.

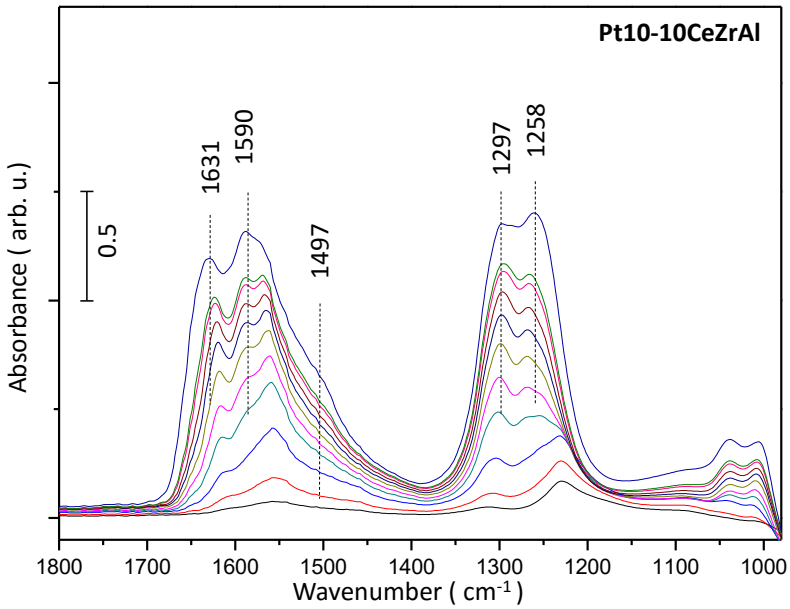

Figure 26. In-situ FTIR spectra for stepwise NO_x adsorption on co-impregnated Pt10-10CeZrAl catalyst at 323 K. The top spectrum was recorded after achieving surface saturation with 5.0 Torr of NO_2 (g) for 10 min at 323 K.

There are five main features located at 1631, 1590, 1497, 1297 and 1258 cm^{-1} on Ce-Zr mixed ternary oxide catalysts (Figures 26 and 27). Vibrational modes at 1625-1631 and 1258-1266 cm^{-1} can be assigned to bridging nitrates and at 1497, 1503 and 1297 - 1301 cm^{-1} can be attributed to monodentate nitrates. In addition to these features, the signal recorded at 1569 - 1590 cm^{-1} is related to bidentate nitrates.

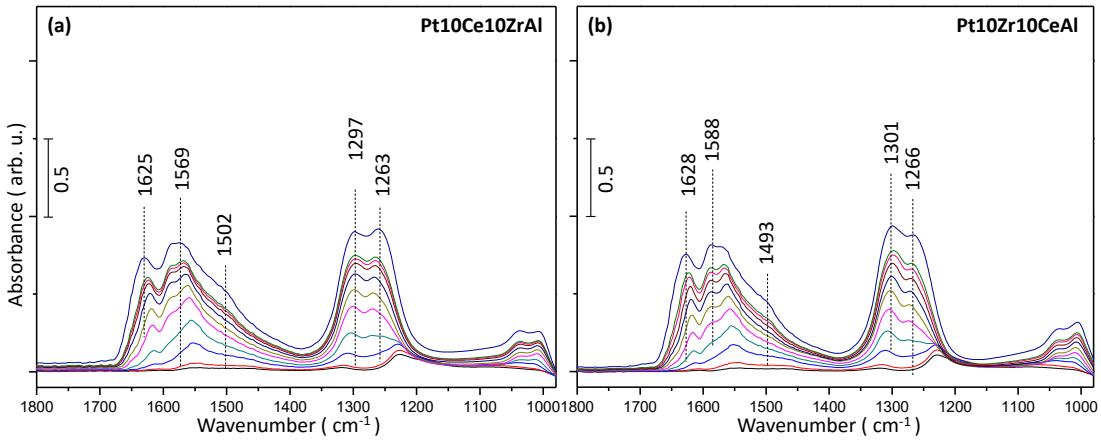

Figure 27. In-situ FTIR spectra for stepwise NO_x adsorption on (a) Pt10Ce10ZrAl and (b) Pt10Zr10CeAl catalysts at 323 K. The top spectra were recorded after achieving surface saturation with 5.0 Torr of NO_2 (g) for 10 min at 323 K.

As can be seen from the Figures 26 and 27, three different ternary oxides had similar types of adsorbed NO_x species. In other words, FT-IR spectroscopic data suggest that changing the synthesis protocol does not lead to a considerable difference in NO_x adsorption characteristics. Furthermore, IR absorbance intensities for the catalysts synthesized by sequential impregnation with different sequences (i.e. Pt10Ce10ZrAl and Pt10Zr10CeAl in Figure 27) were almost identical. However, NO_x absorbance intensities were higher for the Pt10-10CeZrAl catalyst synthesized using the co-impregnation method (Figure 26). Higher absorbance intensities can be linked to a higher NSC. For a more accurate comparison of NO_x adsorption capacities, quantitative NO_x desorption experiments *via* TPD were performed. These results will be discused in section 3.4.

As it was described in section 2.1, co-impregnated Pt10-10CeZrAl catalyst was a calcined twice at 873 K and subsequently at 973 K, however catalysts synthesized by sequential impregnation (i.e. Pt10Ce10ZrAl and Pt10Zr10CeAl) were calcined three times (i.e. two calcination steps at 873 K and one calcination step at 973 K). This additional calcination step for sequentially impregnated materials can affect the oxide surface structure leading to the minor but detectable functional differences evident by differences in IR absorption intensities. There exists a large number of non-equilibrium solid oxide solutions with Ce:Zr 1:1 molar ratio rendering the determination of the exact crystallographic phases via XRD rather challenging [83-86].

Comparison of Figures 25 with Figure 26 and 27 reveals that the co-presence of ceria and zirconia increases the NO_x adsorption intensities in the in-situ FTIR data. Especially, adding cerium precursor and zirconium precursor via co-impregnation protocol particularly increases the IR absorption intensities for the adsorbed NO_x species and most likely the corresponding NSC. This observation can be linked to the oxygen storage/release properties of the catalysts. Yashima et al. reported that $Ce_{0.5}Zr_{0.5}O_2$ containing 1 wt% Pt had higher oxygen storage capacity (i.e. oxygen vacancies) and higher mobility of oxide ions than that of the Pt/CeO_2 catalyst. It is known that, the redox properties of ceria-based materials play a significant role in their catalytic activities [87].

3.2.1. NO_x Adsorption on Quaternary Oxides *via in-situ* FTIR

Figure 28 shows *in-situ* FTIR spectra corresponding to stepwise NO_x adsorption experiments on quaternary oxides namely; (a) Pt10-10CeZr8BaAl, (b) Pt10-10CeZr20BaAl, (c) Pt8Ba10-10CeZrAl, (d) Pt20Ba10-10CeZrAl. The recorded IR spectra during the NO_2 adsorption from low pressures up to surface saturation with 5.0 Torr NO_2 (g) display comparable adsorption characteristics for quaternary oxides which are quite different than that of the BaO-free catalysts presented in Figures 25-27.

While the vibrational features in Figure 28 located at 1420-1439 cm^{-1} and 1324-1330 cm^{-1} can be attributed to bulk/ ionic like nitrates, the features at 1567-1580 cm^{-1} can be assigned to bidentate type of nitrates. On the other hand, the signals at 1248-1254 cm^{-1} and 1634-1641 cm^{-1} can be ascribed to bridging nitrates. It is observed that, BaO impregnation onto co-impregnated Pt10-10CeZrAl mixed metal oxide catalyst, reveals the formation of bulk/ionic like nitrates in additional to the surface nitrates.

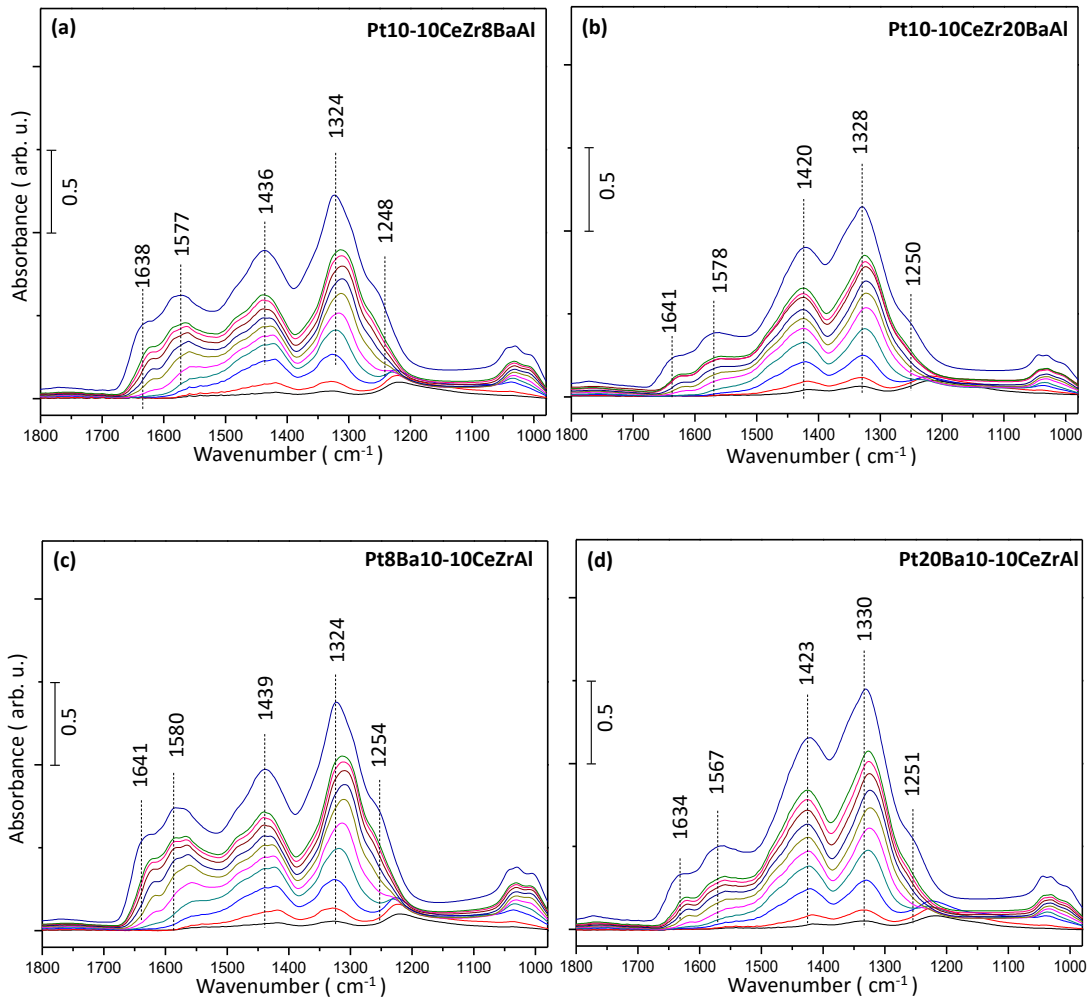

Figure 28. In-situ FTIR spectra for stepwise NO_2 adsorption on (a) Pt10-10CeZr8BaAl, (b) Pt10-10CeZr20BaAl, (c) Pt8Ba10-10CeZrAl and (d) Pt20Ba10-10CeZrAl catalysts at 323 K. The top spectra were recorded after achieving surface saturation with 5.0 Torr of NO_2 (g) for 10 min at 323 K.

Comparing absorbance intensities and nitrate adsorption geometries for different catalysts in Figure 28 can give information about the influence of the synthesis protocol on NO_x adsorption characteristics over quaternary oxide catalysts. These two particular catalysts provide information regarding the functional differences that may arise due to the variations in the dispersion of the

BaO directly on the γ-Al_2O_3 support as in the case of Pt10-10CeZr8BaAl (Figure 28a) versus dispersion of BaO on the 10-10CeZrAl surface as in the case of Pt8Ba10-10CeZrAl (Figure 28c). It is apparent that Pt10-10CeZr8BaAl and Pt8Ba10-10CeZrAl catalysts with 8wt% BaO loading shown in Figures 28a and 26c, respectively had almost identical types of adsorbed NO_x species and IR absorbance intensities. A similar observation is also valid for 20 wt % BaO loading catalysts namely, Pt10-10CeZr20Ba and Pt20Ba10-10CeZrAl presented in Figures 28b and 28d, respectively. Thus, although the relative amount of bulk nitrates on the quaternary oxide catalysts increases with increasing BaO loading (note the increase in 1420-1436 cm^{-1} features in Figures 28b and 28d compared to that of Figures 28a and 28c), impregnation sequence for BaO does not lead to significant changes in adsorption characteristics for a particular BaO loading. Increase in the bulk nitrates for 20wt% BaO loading is consistent with the increasing tendency towards sintering and decreasing dispersion of the BaO overlayer on the support surface.

3.3. NO_x Reduction Experiments in H_2 (g) Atmosphere *via in-situ* FTIR: Chemical Regeneration of Adsorbed NO_x Species with an Aggressive Reducing Agent

3.3.1. NO_x Reduction in H_2 (g) Atmosphere on Binary Oxides *via in-situ* FTIR

Figure 29 and 30 illustrate the time and temperature-dependent nitrate reduction experiments in the presence of H_2(g) on binary oxides monitored in real-time with in-situ FTIR spectroscopy. After surface saturation with 5.0 Torr of

NO_2 (g) at 323 K, materials were exposed to 15 Torr of H_2 (g) at 323 K and held 120 mins at this temperature. Then, materials were annealed at 373, 473 and 573 K in H_2 (g) environment.

Figure 29 presents the corresponding nitrate reduction experiments for the conventional Pt20BaAl catalyst. Time-dependent spectra obtained at 323 K suggest a decrease in absorbance intensities for bridging nitrates (1624 and 1261 cm^{-1}) and bidentate nitrates (1563 cm^{-1}) upon interaction with H_2. Conversely, the intensities of bulk/ionic like nitrates (1418 and 1343 cm^{-1}) showed a concomitant increase.

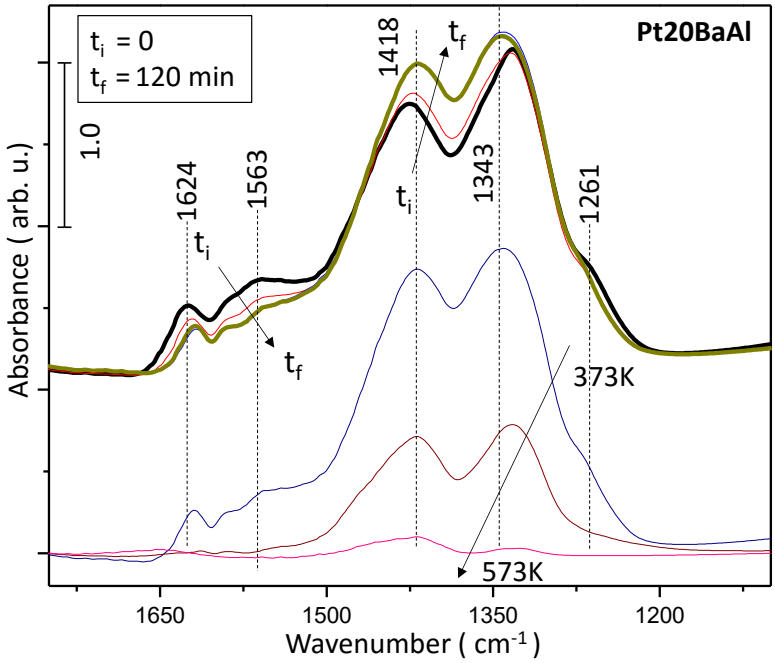

Figure 29. In-situ FTIR spectra for time-dependent and temperature-dependent NO_x reduction in the presence of excess H_2 (g) atmosphere on Pt20BaAl. The upper set of spectra present the time-dependent nitrate/nitrite reduction while the bottom set of spectra show temperature-dependent reduction of nitrate/nitrite functional groups.

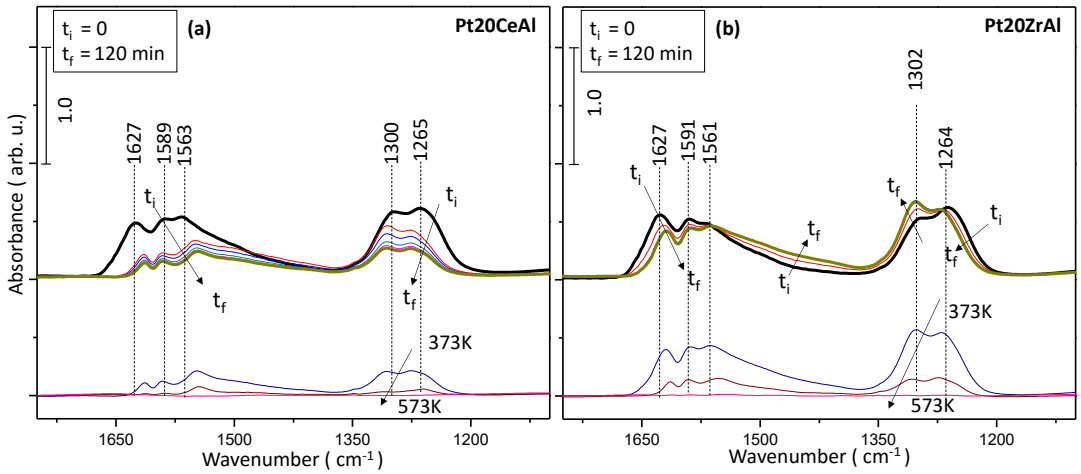

Figure 30. In-situ FTIR spectra for time-dependent and temperature-dependent NO_x reduction in the presence of excess H_2 (g) atmosphere on (a) Pt20CeAl and (b) Pt20ZrAl. The upper part of spectra demonstrate time-dependent nitrate/nitrite reduction. The upper set of spectra present the time-dependent nitrate/nitrite reduction while the bottom set of spectra show temperature-dependent reduction of nitrate/nitrite functional groups.

As can be seen in Figure 30, for the Pt20CeAl and Pt20ZrAl binary oxide catalysts, nitrate reduction takes place through the initial transformation of bridging nitrates to monodentate nitrates. Stabilities of adsorbed nitrate/nitrite species on the NO_x saturated Pt20CeAl and Pt20ZrAl surfaces can be also compared from the data provided in Figure 30. It is clear that surface nitrate features on Pt20ZrAl are more stable than that of the Pt20CeAl in the presence of excess reducing agent (H_2 (g)) environment. This can be attributed to the enhanced hydrogen activation on the Pt/ceria interfacial sites as well as the presence of abundant mobile oxygen vacancies on the ceria surface triggering H-H bond cleavage and initiating the reduction route. Along these lines, the bottommost set of FTIR spectra in Figures 29 and 30 recorded as a function of temperature during the annealing process reveal enhanced attenuation of the

vibrational intensities of adsorbed surface nitrates on Pt20CeAl (Figure 30a) as compared to that of the Pt20BaAl (Figure 29) and Pt20ZrAl (Figure 30b). Nitrate/nitrite functional groups are eliminated significantly on the Pt20CeAl and Pt20ZrAl surfaces (Figure 30) after annealing at 573 K. However, complete reduction of surface and bulk/ ionic type of nitrates/nitrites annealing requires much higher temperatures for Pt20BaAl the catalyst. These results suggest that presence of basic BaO sites significantly increase the resilience of the stored nitrates even in the presence of an aggressive reducing agent such as hydrogen.

3.3.1. NO_x Reduction in H_2 (g) Atmosphere on Ternary Oxides *via in-situ* FTIR

Figure 31 and 32 represent the time-dependent and temperature dependent in-situ FTIR spectra regarding the reduction of adsorbed NO_x features on ternary oxides in the presence of excess H_2 (g) exposure. While time-dependent in-situ FTIR spectra were demonstrated on the top series, infrared results recorded during annealing from 373 K to 573 K were depicted at the bottom part of the Figures 31 and 32.

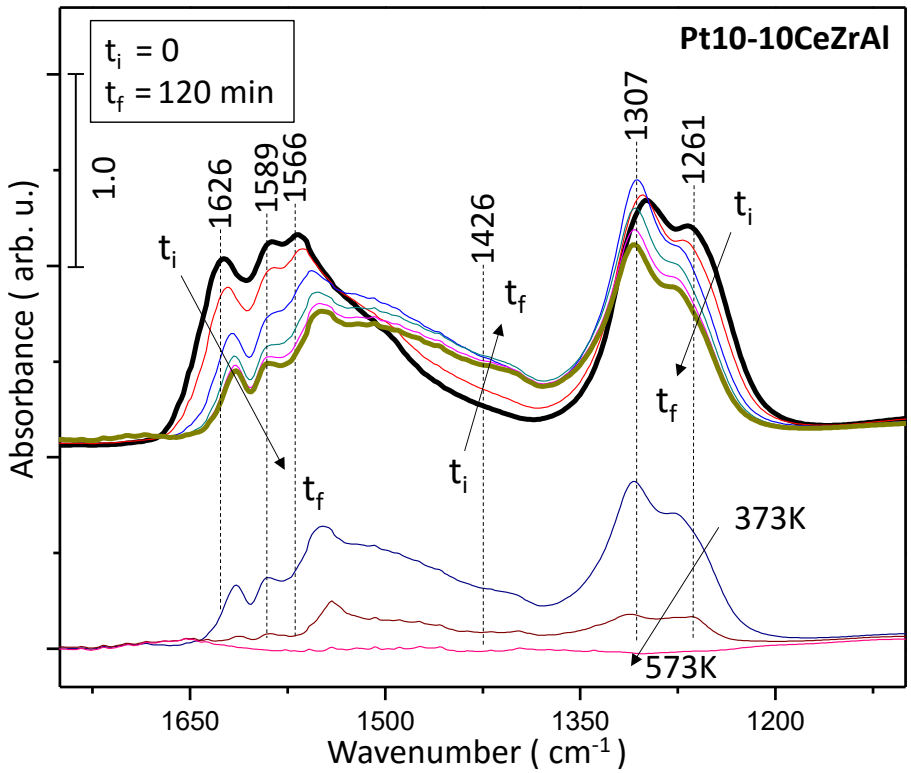

Figure 31. In-situ FTIR spectra for time-dependent and temperature-dependent NO_x reduction in the presence of excess H_2 (g) atmosphere on co-impregnated Pt10-10CeZrAl catalyst. The upper set of spectra present the time-dependent nitrate/nitrite reduction while the bottom set of spectra show temperature-dependent reduction of nitrate/nitrite functional groups.

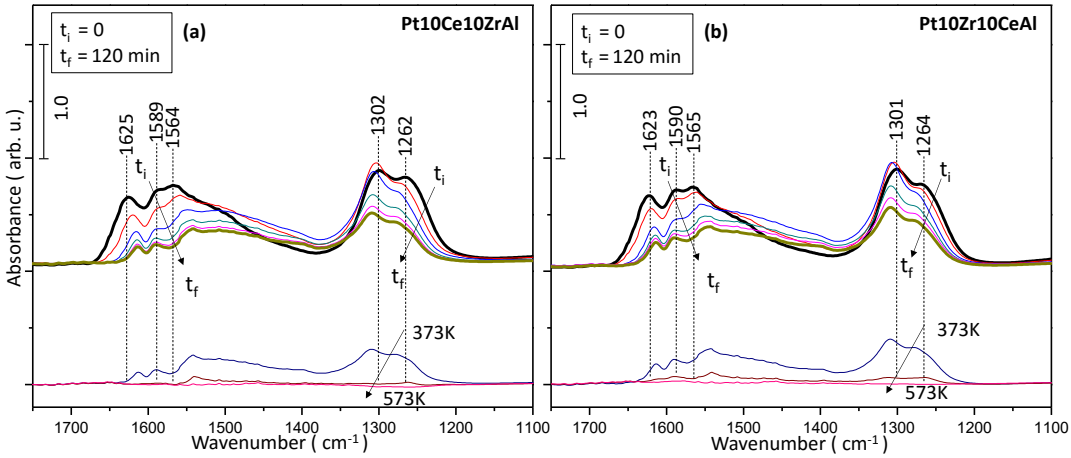

Figure 32. In-situ FTIR spectra for time-dependent and temperature-dependent NO_x reduction in the presence of excess H_2 (g) atmosphere on sequentially impregnated (a) Pt10Ce10ZrAl, (b) Pt10Zr10CeAl catalysts. The upper set of spectra present the time-dependent nitrate/nitrite reduction while the bottom set of spectra show temperature-dependent reduction of nitrate/nitrite functional groups.

Nitrate/nitrite reduction characteristics of ternary oxides synthesized by different synthesis protocol were quite comparable except the presence of a greater extent of bulk/ ionic like nitrates or nitrites on the Pt10-10CeZr co-impregnated catalyst (Figure 31) towards the end of reduction process. The monodentate nitrates (1564-1566 cm^{-1}) were thermally more stable than bridging nitrates (1625 cm^{-1}). Complete regeneration of bridging nitrates can be achieved at 473 K, however residual amount of monodentate nitrates still continue to exist on the ternary oxide surfaces at this temperature.

Comparison of Figures 31 and 32 reveals that simultaneous presence of CeO_2 and ZrO_2 enhances the nitrate stability. As it is mentioned in section 3.3.1. nitrates on Pt20ZrAl are more stable than that of Pt20CeAl which is also clear

from the greater IR absorbance intensities on Pt20ZrAl material during time-dependent NO_x reduction process (Figure 31). These results are in a good agreement with a former study regarding Pt-functionalized $Ce_xZr_{1-x}O_2$ where it was reported that nitrate reduction temperatures shift to lower values with increasing ceria loading [88].

3.3.2. NO_x Reduction Experiments in H_2 (g) Atmosphere on Quaternary Oxides *via in-situ* FTIR

Analogous NO_x reduction experiments were also performed on the synthesized quaternary oxide catalysts as shown in Figure 33.

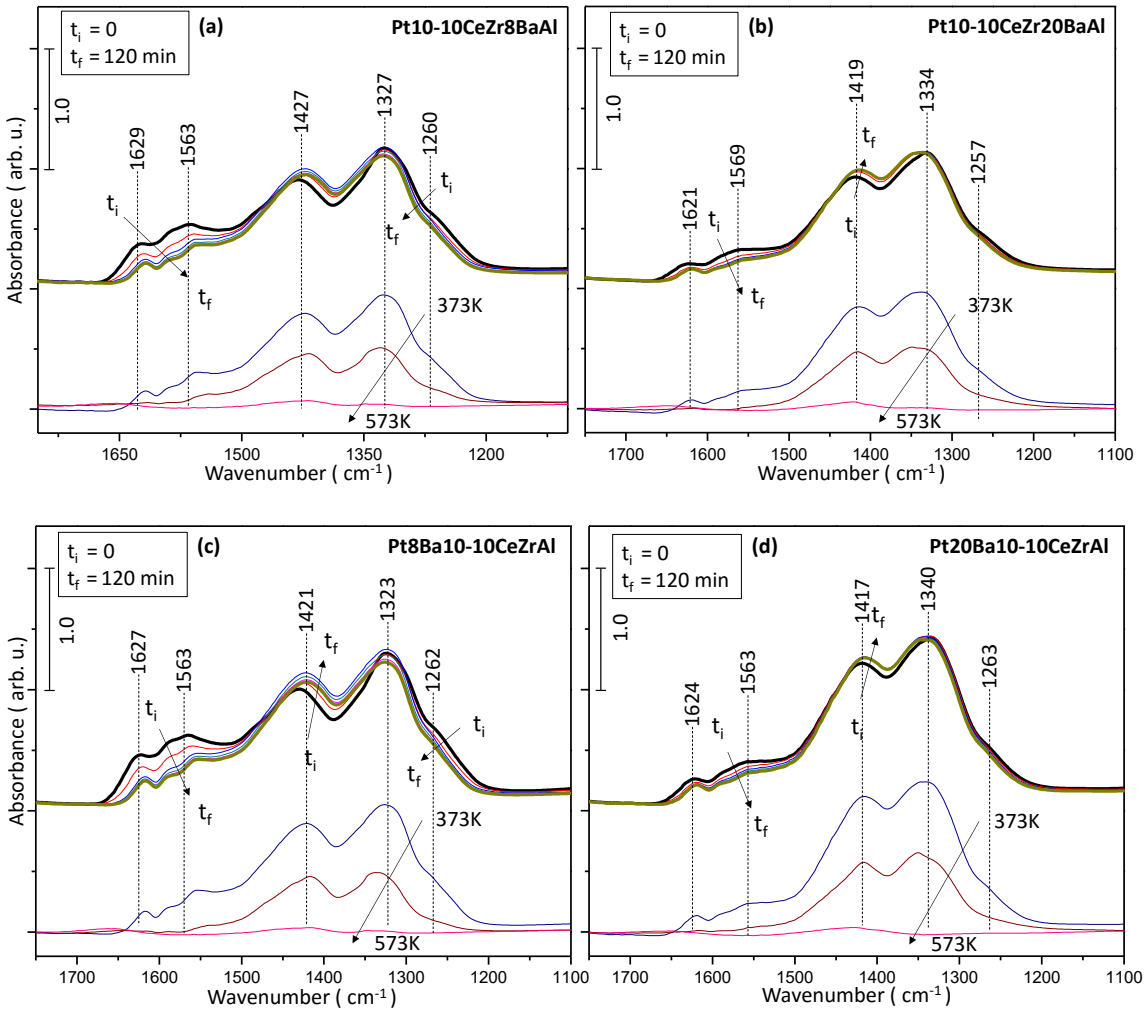

Figure 33. In-situ FTIR spectra for time-dependent and temperature-dependent NO_x reduction in the presence of excess H_2 (g) atmosphere on quaternary oxides (a) Pt10-10CeZr8BaAl, (b) Pt10-10CeZr20BaAl, (c) Pt8Ba10-10CeZrAl and (d) Pt20Ba10-10CeZrAl catalysts. The upper set of spectra present the time-dependent nitrate/nitrite reduction while the bottom set of spectra show temperature-dependent reduction of nitrate/nitrite functional groups.

In Figure 33, all of the quaternary oxides had similar reduction characteristics; yet differences in IR absorbance intensities of nitrate/nitrate functional groups were observed as a function of BaO loading. Figure 33 reveals that the intensities of the vibrational signals at 1627, 1629 cm^{-1} (bridging nitrates) and at 1563 cm^{-1} (bidentate nitrates) attenuated more significantly during reduction process for low BaO loading materials namely, Pt10-10CeZr8BaAl and Pt8Ba10-10CeZrAl. It can be argued that, increasing the BaO loading enhances nitrate/nitrite stability. Barium aluminate ($BaAl_2O_4$) formation can also be considered for the BaO-functionalized catalysts. NO_x adsorption on barium aluminate reveals bands at 1360-1430 cm^{-1} due to various types of nitrates and a broad band at 1605-1630 cm^{-1} that is ascribed to the bridging nitrates [89]. Since, such features also exist in Figure 33, existence of nitrates on $BaAl_2O_4$ domains cannot be ruled out. Note that corresponding XRD data for these samples presented in Section 3.1.1 also indicate the presence of $BaAl_2O_4$, particularly for high BaO loading materials.

3.4. NO_x Desorption Experiments *via* TPD: Quantitative NO_x Storage Capacity Analysis and Thermal Regeneration of Adsorbed NO_x Species in the Absence of a Reducing Agent

3.4.1. NO_x Desorption *via* TPD on Binary Oxides

As discussed earlier, TPD experiments were performed in order to obtain quantitative NSC data for comparing the storage characteristics of different catalysts currently synthesized. NO_x desorption *via* TPD results can also provide information about thermal regeneration abilities of NO_x related features in the

absence of a reducing agent and reveal insight regarding thermal stabilities of that stored NO_x species.

NO_x TPD profiles were recorded saturating the catalyst surfaces with NO_2 as described in the experimental section. Note that NO_x TPD experiments were carried out on aged/de-greened catalysts which were initially subjected to NO_2 saturation at 323 K and subsequent reduction with H_2 at various temperatures as mentioned in the previous section.

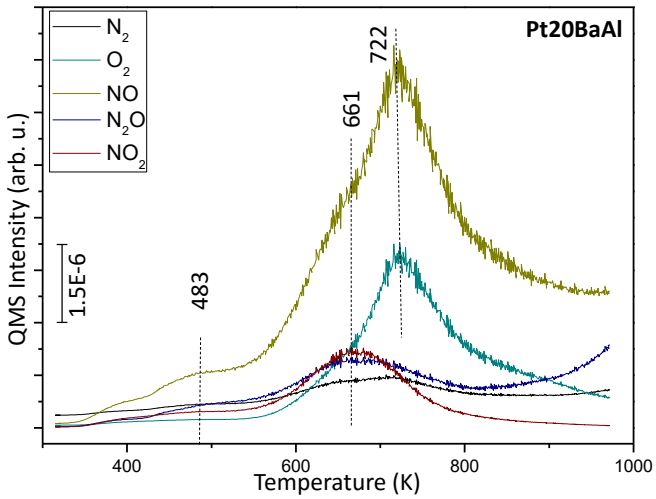

Figure 34. NO_x TPD profiles of Pt20BaAl after surface saturation with 5.0 Torr NO_2 (g) at 323 K for 10 min.

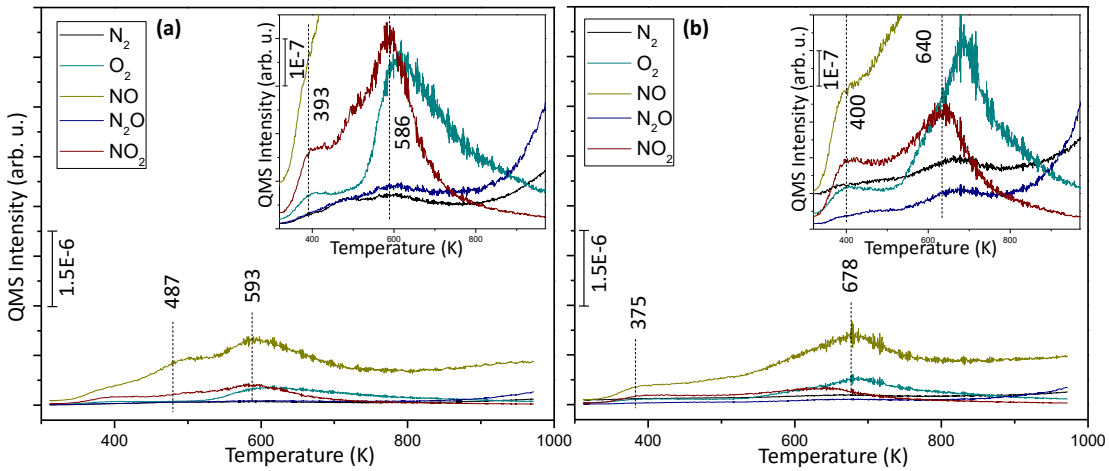

Figure 35. NO_x TPD profiles of (a) Pt20CeAl and (b) Pt20ZrAl after surface saturation with 5.0 Torr NO_2 (g) at 323 K for 10 min.

Figures 34 and 35 illustrate NO_x TPD experiments for binary oxides namely, Pt20BaAl (Figure 342) as well as Pt20CeAl and Pt20ZrAl (Figure 35). While three main NO desorption signals were observed for Pt20BaAl catalyst, Pt20CeAl and Pt20ZrAl materials had two major desorption signals appearing at lower desorption temperatures than that of the Pt20BaAl catalyst. TPD profiles of Pt20BaAl show a desorption maximum at 722 K for NO (m/z= 30) and O_2 (m/z=32) and a second maximum at 661 K for N_2 (m/z=28), N_2O (m/z=44) and NO_2 (m/z=46), as well as another maximum at 483 K for m/z=30 (NO). TPD results clearly indicate that nitrate/nitrite decomposition on Pt20CeAl takes place at lower temperatures (487 and 593 K) than that of the Pt20ZrAl and Pt20BaAl materials. Stability of the nitrate/nitrite groups can be correlated with decomposition temperatures. Thus, it can be argued that Pt20CeAl can catalyze nitrate/nitrites decomposition in more facile way as compared to that of Pt20ZrAl. Furthermore, adsorbed nitrate/nitrite functional groups on Pt20BaAl were found to be thermally more stable than the Ce-Zr containing binary oxides.

Total NO_x storage capacities were calculated from total integrated areas under all of the NO_x related desorption features (i.e. N_2, NO, N_2O and NO_2) in TPD by using National Institute of Standards and Technology (NIST) mass spectroscopic fragmentation patterns for each gas. For NO_2 quantification, QMS channels at m/z = 14, m/z = 30 and m/z = 46 were used. According to the NIST database QMS fragmentation patterns, total intensity of m/z = 14 (N_2), m/z = 30 (NO) and m/z = 46 (NO_2) channels to the channel at m/z = 46 ratio is 3.98. Therefore to compute total NO_x that comes from NO_2 gas, integrated area under m/z = 46 signal (I46) was multiplied by a factor of 3.98. For the N_2O desorption signal, channels at m/z =14, m/z =28, m/z =30 and m/z =44 were considered. In order to normalize the integrated areas for N_2O desorption channel, the integrated area under m/z = 44 was multiplied by a factor of 2.65. For the desorption of NO gas, the integrated m/z = 30 signal was multiplied by 1.08. Finally, N_2 gas desorption is relevant to N_2 m/z = 28 and N m/z = 14 channels. Hence, in order to normalize the integrated area under m/z = 28 signal, it should be multiplied by a factor of 1.14.

It should be noted that m/z = 28 signal is associated with more than one desorption channels (i.e. N_2 and N_2O assuming desorption of CO is negligible), thus contribution from N_2O to this signal should be subtracted from the total m/z = 28 signal. Likewise, m/z = 30 channel signal comes from NO, N_2O and NO_2 desorption channels. Thus, m/z=30 signal coming from N_2O and NO_2 should be subtracted from the total m/z=30 signal to calculate the net NO desorption signal. Additionally, some of the gases such as N_2 and N_2O are comprised of 2 N atoms

per molecule, so their integrated signals must be multiplied by two. Finally, total NO_x storage capacities were demonstrated after normalizing them by their masses.

Corresponding equations that were used to calculate total NO_x storage capacities are given below:

$$\sum_N (NO_2) = I_{46} \times 3.98$$

$$\sum_N (N_2O) = I_{44} \times 2.65$$

$$\sum_N (NO) = [I_{30} - I_{44} \times 0.31 - I_{46} \times 2.72] \times 1.08$$

$$\sum_N (N_2) = [I_{28} - I_{44} \times 0.22] \times 2.14$$

$$\text{Total } NO_x \text{ Storage} = \sum_N (NO_2) + \sum_N (N_2O) + \sum_N (NO) + \sum_N (N_2)$$

$\sum_N (A)$ symbol was used to represent corrected number of desorbed NOx related molecules comes from the *A* molecule , I_A symbol represents integrated area for m/z =*A* signal.

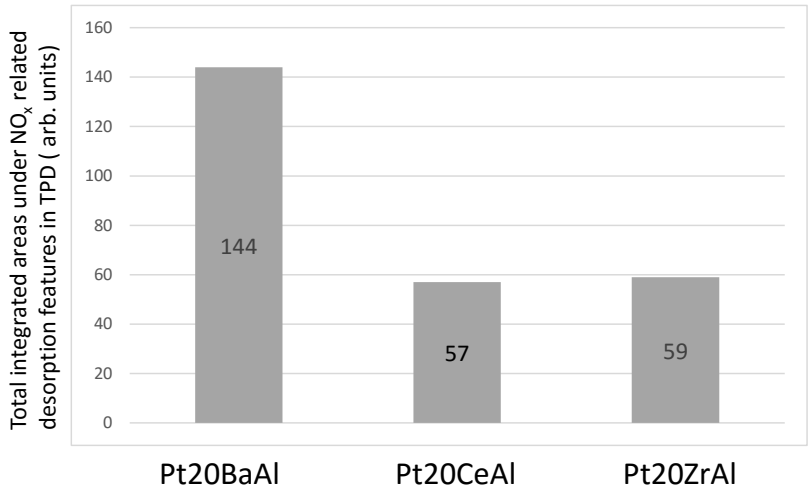

Figure 36. Total integrated TPD signals under NO_x related desorption features in TPD for Pt20BaAl, Pt20CeAl and Pt20ZrAl.

Comparison of the total NSC of Pt20CeAl and Pt20ZrAl with that of the conventional Pt20BaAl catalyst reveals that although NSC values are comparable for the Pt20CeAl and Pt20ZrAl, they are significantly lower than that of the conventional catalyst. These results clearly point out the need for the presence of basic BaO sites for enhanced NSC.

3.4.2. NO_x Desorption *via* TPD on Ternary Oxides

NO_x desorption and decomposition behavior of ternary oxides synthesized by sequential impregnation or co-impregnation methods were also investigated using NO_x TPD after NO_x adsorption and reduction experiments. Figure 37 demonstrates the NO_x TPD profiles of Pt10-10CeZrAl, co-impregnated catalyst, and Figure 38 illustrates the analogous results on sequentially impregnated samples namely, Pt10Ce10ZrAl and Pt10Zr10CeAl.

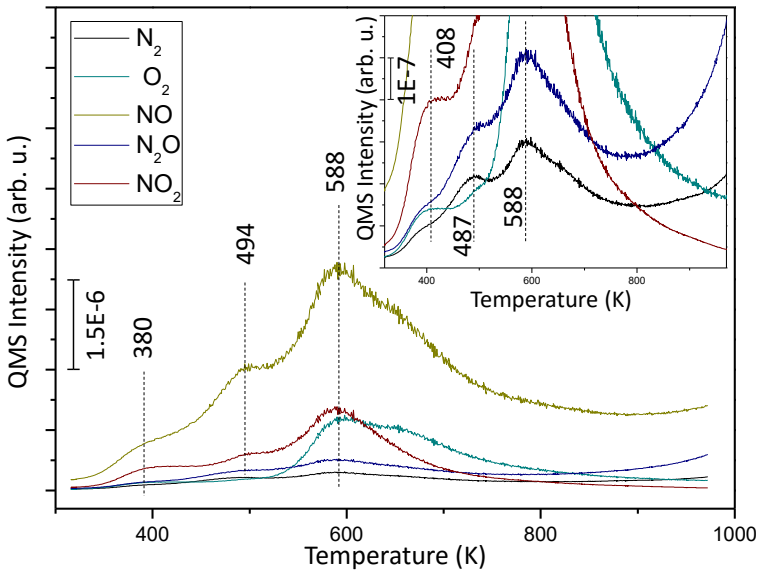

Figure 37. NO_x TPD profiles of Pt10-10CeZrAl after surface saturation with 5.0 Torr NO_2 (g) at 323 K for 10 min.

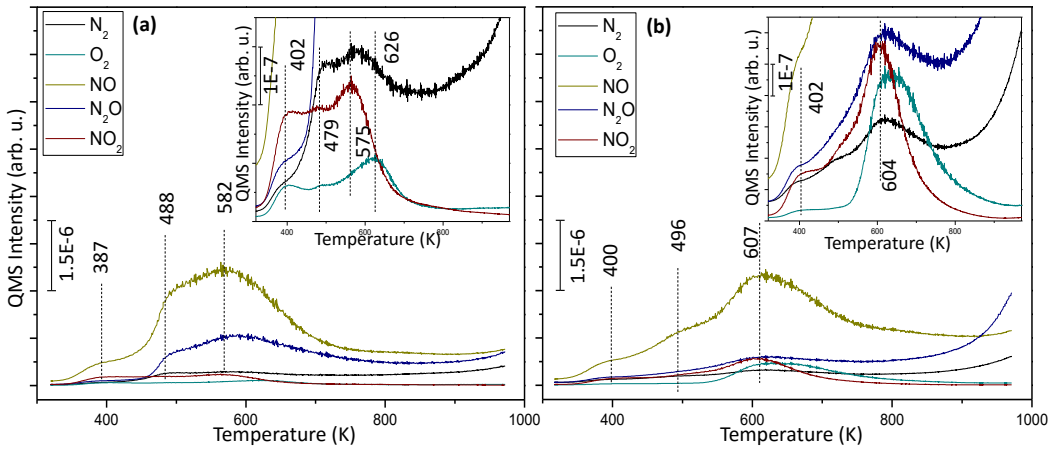

Figure 38. NO_x TPD profiles of (a) Pt10Ce10ZrAl and (b) Pt10Zr10CeAl after surface saturation with 5.0 Torr NO_2 (g) at 323 K for 10 min.

There are three major NO (m/z=30) desorption maxima in the TPD profiles of ternary oxides due to the decomposition of nitrate/nitrite stored on the catalysts (Figures 37 and 38). On the co-impregnated sample (Figure 37) these maxima appear at 380 K, 494 and 588 K. These last couple of NO desorption maxima is also concomitant to the evolution of N_2 (m/z=28), and NO_2 (m/z=46) and N_2O (m/z=44) features as can be seen in the inset of Figure 37. It is worth mentioning that there exist various differences in the thermal decomposition pathways of these ternary oxides prepared with different synthesis protocols. Probably one of the most striking dissimilarity is associated with O_2 evolution. While the co-impregnated Pt10-10CeZrAl catalyst (Figure 37) reveals a significant amount of O_2 evolution within 580-700 K suggesting that strongly bound nitrates (i.e. bulk-like nitrates) decompose predominantly in the form of $NO+O_2$ (along with a lesser extent of N_2 and N_2O evolution), weakly bound nitrates (i.e. surface nitrates) desorbing at T < 580 K decompose mostly in the

form of NO_2 + O_2. It should be noted that oxygen release during nitrate decomposition is a rather complex surface phenomenon as the generated oxygen can also be captured by the reducible oxide domains such as CeO_x/CeO_2 or ZrO_x/ZrO_2 on the catalyst surface and titrate the defects/oxygen vacancies in these structures. Unlike the co-impregnated Pt10-10CeZrAl catalyst, sequential impregnation catalysts (Figure 38) reveals relatively smaller oxygen evolution during nitrate decomposition, this can be attributed to the differences in oxygen vacancy/defect distribution and the dissimilarities in the surface chemistry of the adsorption sites on the reducible oxide domains.

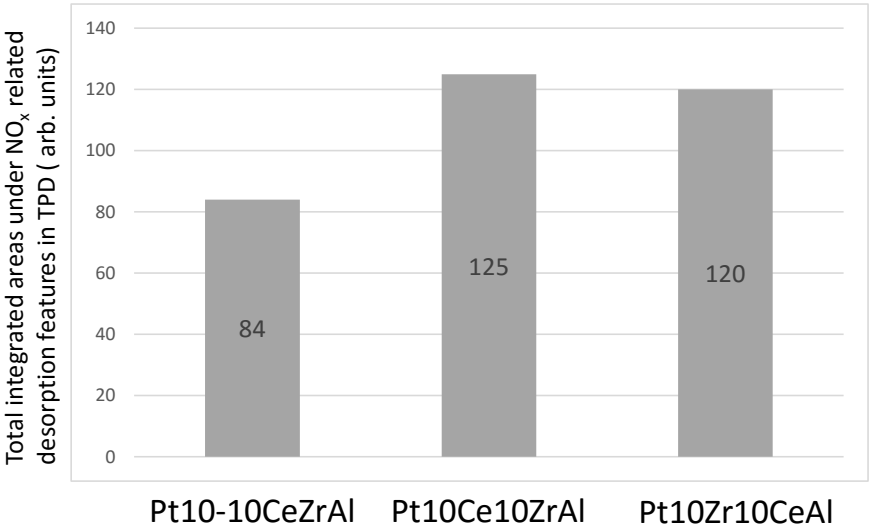

Figure 39. Total integrated areas under NO_x related desorption features in TPD for Pt10-10CeZrAl, Pt10Ce10ZrAl and Pt10Zr10CeAl.

Comparison of Figure 36 (NSC results for Pt20CeAl and Pt20ZrAl binary oxides) and Figure 39 (NSC results for Pt10-10CeZrAl, Pt10Ce10ZrAl and Pt10Zr10CeAl ternary oxides) points to the fact that presence of ceria and zirconia domains significantly enhances the NO_x storage capacity. Furthermore, sequential

impregnation seems to increase the NSC more than that of the co-impregnation protocol.

3.4.3. NO_x Desorption *via* TPD on Quaternary Oxides

NO_x TPD experiments were also performed for different types of quaternary oxides with 8 wt% or 20 wt% BaO loading synthesized with different protocols as described above.

Figure 40 presents the NO_x TPD data for the co-impregnated Pt10-10CeZr8BaAl, Pt10-10CeZr20BaAl, Pt8Ba10-10CeZrAl and Pt20Ba10-10CeZrAl samples where BaO loading is varied between 8 wt% and 20 wt%. Furthermore, in these samples, order for the BaO dispersion is also modified in two different manners. While for the Pt10-10CeZr8BaAl, Pt10-10CeZr20BaAl samples, BaO is directly dispersed on the γ-Al_2O_3 support material, for the Pt8Ba10-10CeZrAl and Pt20Ba10-10CeZrAl samples, BaO is dispersed on the 10-10CeZrAl co-impregnated mixed oxide surface.

As described along with Figure 41, the major NO desorption maximum for co-impregnated Pt10-10CeZrAl material was observed at 588 K. On the other hand for 8 wt% BaO loading quaternary oxides (Figure 40a and 40c) the major NO desorption maximum was at T > 697 K and further increase in BaO loading to 20 wt% leads to even higher decomposition temperatures (Figure 40b and 40d). This observation is in perfect agreement with the previously described current in-situ FTIR results indicating that the increase baria loading stabilizes the stored

nitrate/nitrite species on the catalyst surfaces due to the formation of bulk like nitrates.

It is important to note that although NO_x decomposition profiles for Ba-free ternary oxides (Figures 37 and 38) show discernible differences among each other as a function of catalyst preparation protocol, Ba-containing materials (Figure 40) reveal quite similar desorption characteristics with much less dissimilarities. This observation suggests that for the Ba-containing samples, BaO dispersion (i.e. BaO particle size and the extent of wetting of BaO domains on the CeZrAl surface) is similar for all catalysts where the nitrates are stored mostly on the BaO domains on similar adsorption/storage sites.

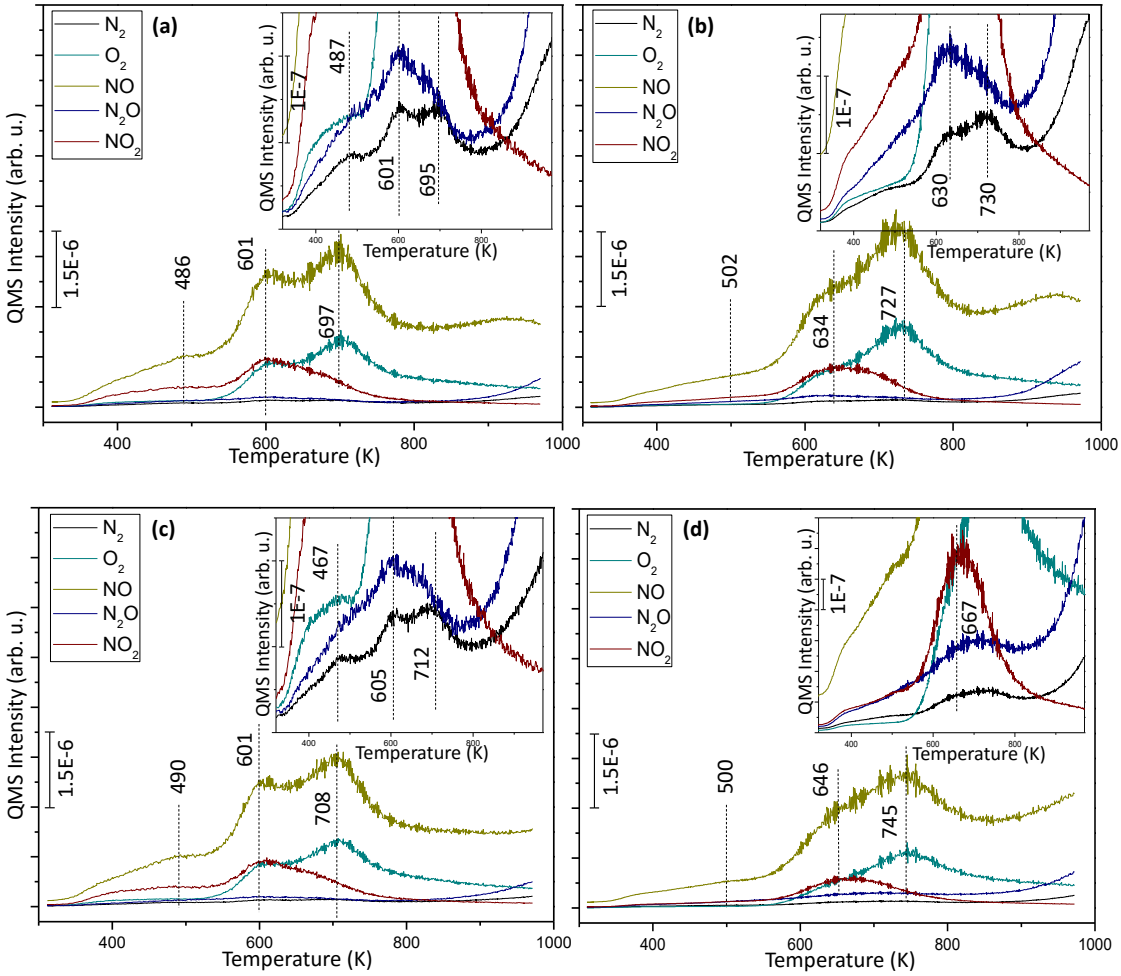

Figure 40. NO_x TPD profiles for (a) Pt10-10CeZr8BaAl, (b) Pt10-10CeZr20BaAl, (c) Pt8Ba10-10CeZrAl and (d) Pt20Ba10-10CeZrAl samples after surface saturation with 5.0 Torr NO_2 (g) at 323 K for 10 min.

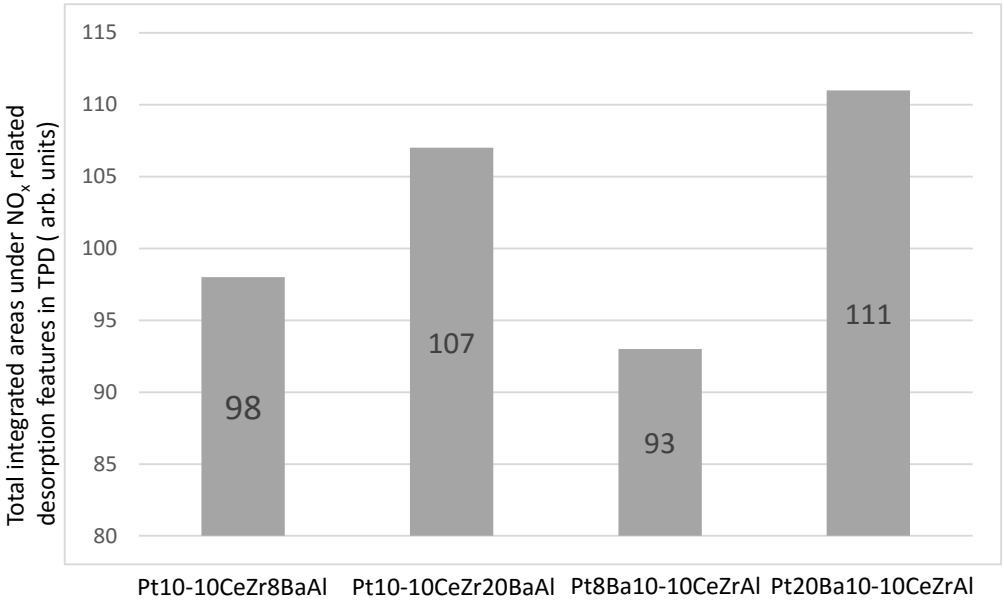

Figure 41. Total integrated areas under NO_x related desorption features in TPD (arb. units) for Pt10-10CeZr8BaAl, Pt10-10CeZr20BaAl, Pt8Ba10-10CeZrAl and Pt20Ba10-10CeZrAl.

Figure 41 compares NSC values obtained via TPD analysis of the Pt10-10CeZr8BaAl, Pt10-10CeZr20BaAl, Pt8Ba10-10CeZrAl and Pt20Ba10-10CeZrAl quaternary oxide catalysts. As compared to their ternary counterparts (Figure 39), BaO addition is observed to increase the NSC by ca. 20% on th quaternary oxide catalysts (Figure 40). Variations in the BaO loading has a relatively minor (ca. 10wt%) influence on the NSC indicating that BaO domains are already well dispersed on the CeZrAl surface even at 8wt% BaO loading where further BaO loading does not significantly enhance the BaO dispersion and hence NSC.

Figure 42 presents a global comparison of the NSC values for all of the investigated NSR catalysts. It is apparent that sequentially impregnated

Pt10Ce10ZrAl and Pt10Zr10CeAl ternary oxide samples as well as 20wt% BaO loading Pt10-10CeZr20BaAl and Pt20Ba10-10CeZrAl quaternary oxide samples have NSC values that are close to that of the conventional Pt20BaAl benchmark catalyst. In other words, Ce-Zr promotion leads to a minor sacrifice in NSC as compared to the benchmark catalyst. However, as will be described in the next section focusing on sulfur poisoning and regeneration, Ce-Zr promoted systems reveal significant improvements/enhancements regarding sulfur tolerance, in spite of their minor underperformance in terms of NSC.

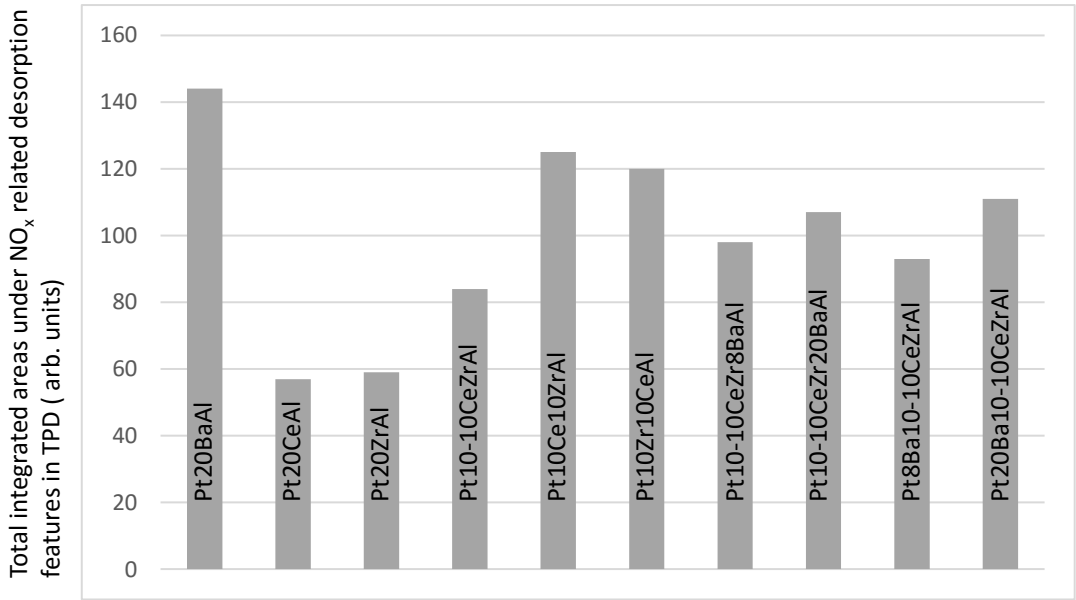

Figure 42. Global comparison of NSC values of all of the currently investigated NSR catalysts.

3.5. SO_x Adsorption *via in-situ* FT-IR Experiments: Understanding Sulfur Uptake and Poisoning Pathways

3.5.1. SO_x Adsorption *via in-situ* FT-IR on Binary and Ternary Oxides

In order to investigate SO_x adsorption characteristics of binary and ternary oxides in-situ FTIR experiments were performed (Figure 43). Catalysts surfaces were initially exposed to 2 Torr of SO_2 + O_2 (SO_2:O_2 = 1:10) gas mixture at 323 K. After 5 min of exposure, the first (black) spectra were recorded. Then, the materials were annealed to 373, 473, 573 and 673 K subsequently. The catalysts were kept at each specific temperature for 5 min and then temperature was decreased to 323 K to acquire IR spectra, followed by annealing to the next target temperature.

During the initial steps of SO_x adsorption at low temperatures, two major vibrational peaks corresponding to surface sulfates and sulfites were observed at ca. 1050 and 940 cm^{-1}. As the annealing temperature was increased to 473 K, additional vibrational features started to appear at 1330 and 1400 cm^{-1} for Pt20CeAl, Pt20ZrAl and Pt10-10CeZrAl and at 1165 and 1250 cm^{-1} for Pt20BaAl (Figure 43).

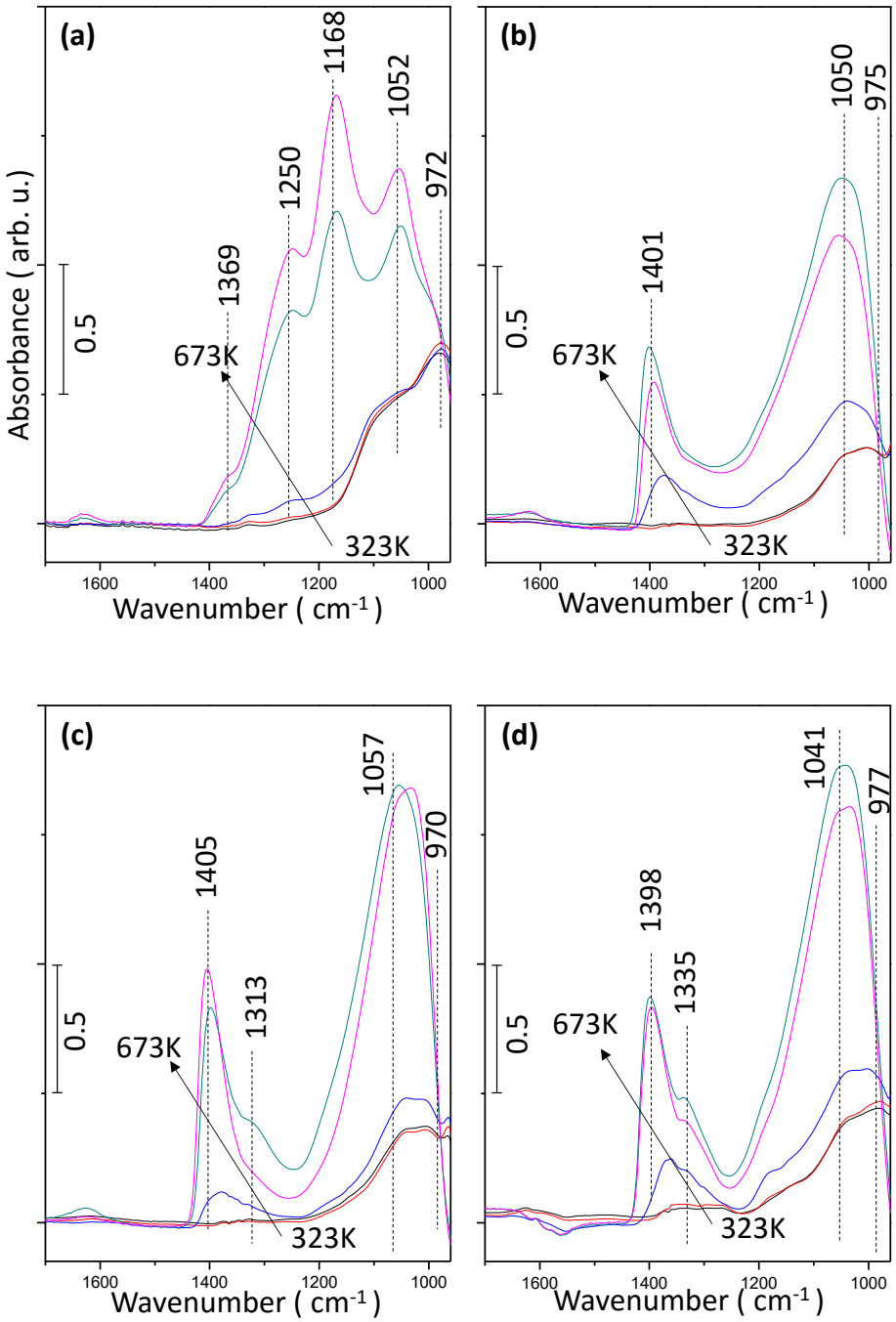

Figure 43. In-situ FTIR spectra for SO_x adsorption on (a) Pt20BaAl, (b) Pt20CeAl, (c) Pt20ZrAl and (d) Pt10-10CeZrAl catalysts. The spectra were recorded after 2.0 Torr of SO_2 + O_2 gas mixture exposure at 323 K. Adsorption properties were followed by annealing the catalysts at 373, 473, 573 and 673 K for 5 min.

Although BaO-deficient binary and ternary oxides resulted in similar SO_x adsorption characteristics (Figures 43b-43d); Pt20BaAl sample (Figure 43a) revealed additional vibrational features at 1168 and 1250 cm^{-1} that can be attributed to bulk/ionic like sulfate ($BaSO_4$) formation. Note that the features located at >1350 and ca. 1050 cm^{-1} can be assigned to surface sulfates (SO_4^{-2}) The stretching located at around 972 cm^{-1} observed for all of the spectra in Figure 43 can be ascribed to surface sulfites (SO_3^{-2}) [72-75, 90].

3.5.2. SO_x Adsorption on Quaternary Oxides *via* in-situ FTIR

Similar SO_x adsorption experiments on quaternary oxides *via in-situ* FTIR are given in Figure 44. In Figures 44a and 44c, Pt10-10CeZr8BaAl and Pt8Ba10-10CeZrAl samples reveal five vibrational features around 1365, 1263, 1169, 1045 and 985 cm^{-1}. The vibrational features at 1365 and 1045 cm^{-1} can be attributed to the formation of surface sulfates, (SO_4^{-2}), whereas, stretching of surface sulfite groups (SO_3^{-2}) can be seen at around 985 cm^{-1}. The feature at 1263 and 1169 cm^{-1} are attributed to bulk/ionic like sulfates [72-75, 90]. With the increase in annealing temperature, transformation of surface sulfites to surface sulfates as well as bulk/ionic type of sulfates can be observed from the vibrational spectra. Identification of individual SO_x features is rather difficult for high-Baria loading samples due to spectral overlap between multiple features. Yet, it can be argued that Pt10-10CeZr20BaAl and Pt20Ba10-10CeZrAl reveal four major SO_x features in their IR spectra (Figure 44). While the peaks at around 1260 and 1160 cm^{-1} can be assigned to bulk/ionic type of sulfates, the features at around 1060 and 1018 cm^{-1} can be attributed to surface sulfates.

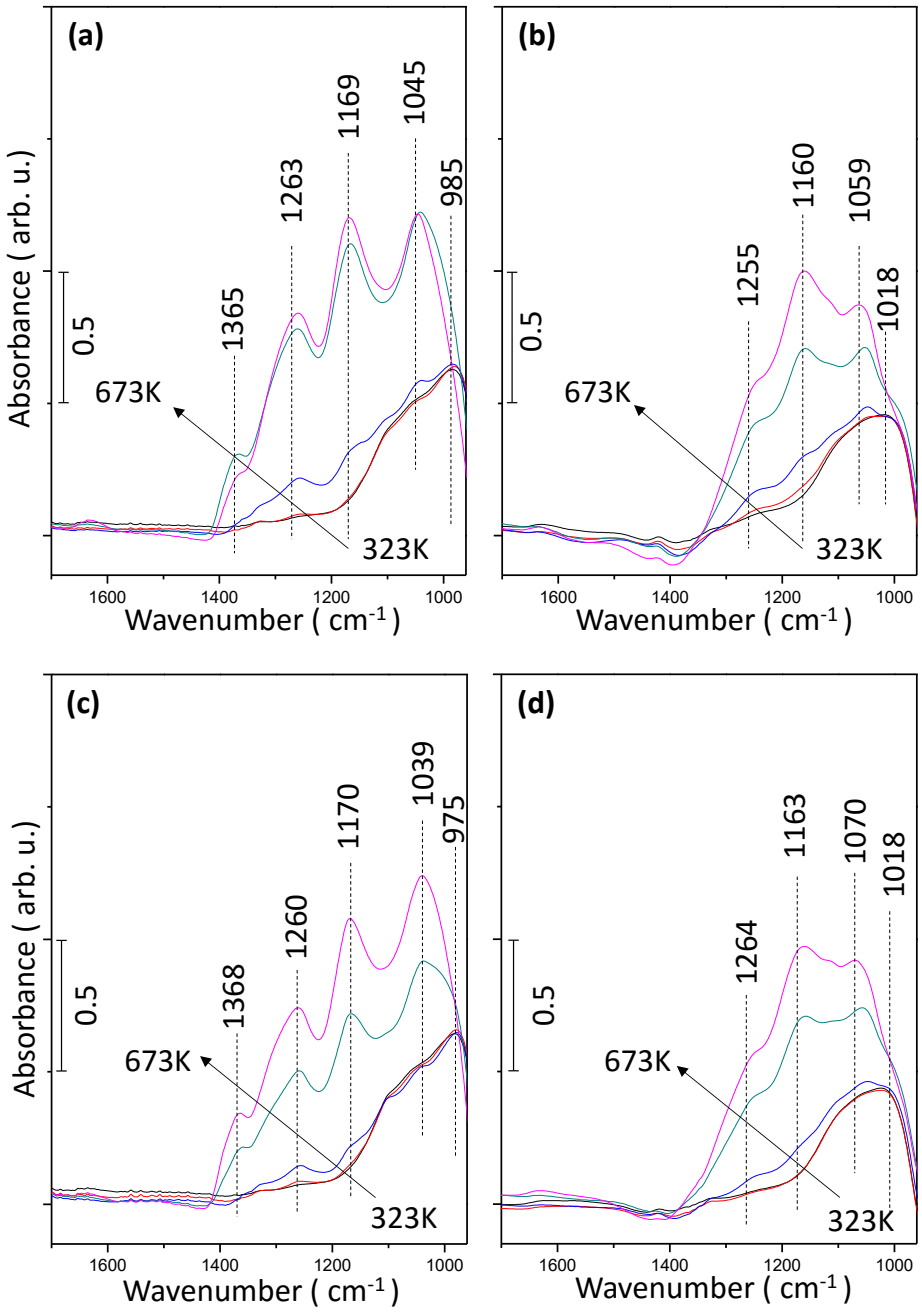

Figure 44. In-situ FTIR spectra for SO_x adsorption of (a) Pt10-10CeZr8BaAl, (b) Pt10-10CeZr20BaAl, (c) Pt8Ba10-10CeZrAl and (d) Pt20Ba10-10CeZrAl catalysts. The spectra were recorded after 2.0 Torr of SO_2 + O_2 gas mixture exposure at 323 K. Adsorption properties were followed by annealing the catalysts at 373, 473, 573 and 673 K for 5 min.

3.6. Monitoring SO_x Regeneration in the Presence of a Reducing Agent *via in-situ* FTIR Experiments

3.6.1. SO_x Reduction *via in-situ* FTIR on Binary and Ternary Oxides

SO_x reduction experiments were performed via in-situ FTIR after SO_x adsorption for selected samples in order to understand chemical regeneration abilities of adsorbed SO_x species with an aggressive reducing agent, H_2(g). Sulfur poisoned catalysts were initially exposed to 15 Torr of H_2 (g) at 323 K and subsequently annealed to 473, 573, 673, 773, 873 and 973 K respectively for 5 min in order to follow desulfation characteristics of binary and ternary oxides. In each panel in Figure 45, the red spectra illustrate the FTIR spectra recorded at 323 K after initial poisoning at 673 K, and the green spectra correspond to the IR spectra recorded at 323 K, after SO_x reduction process at 873 K in H_2(g).

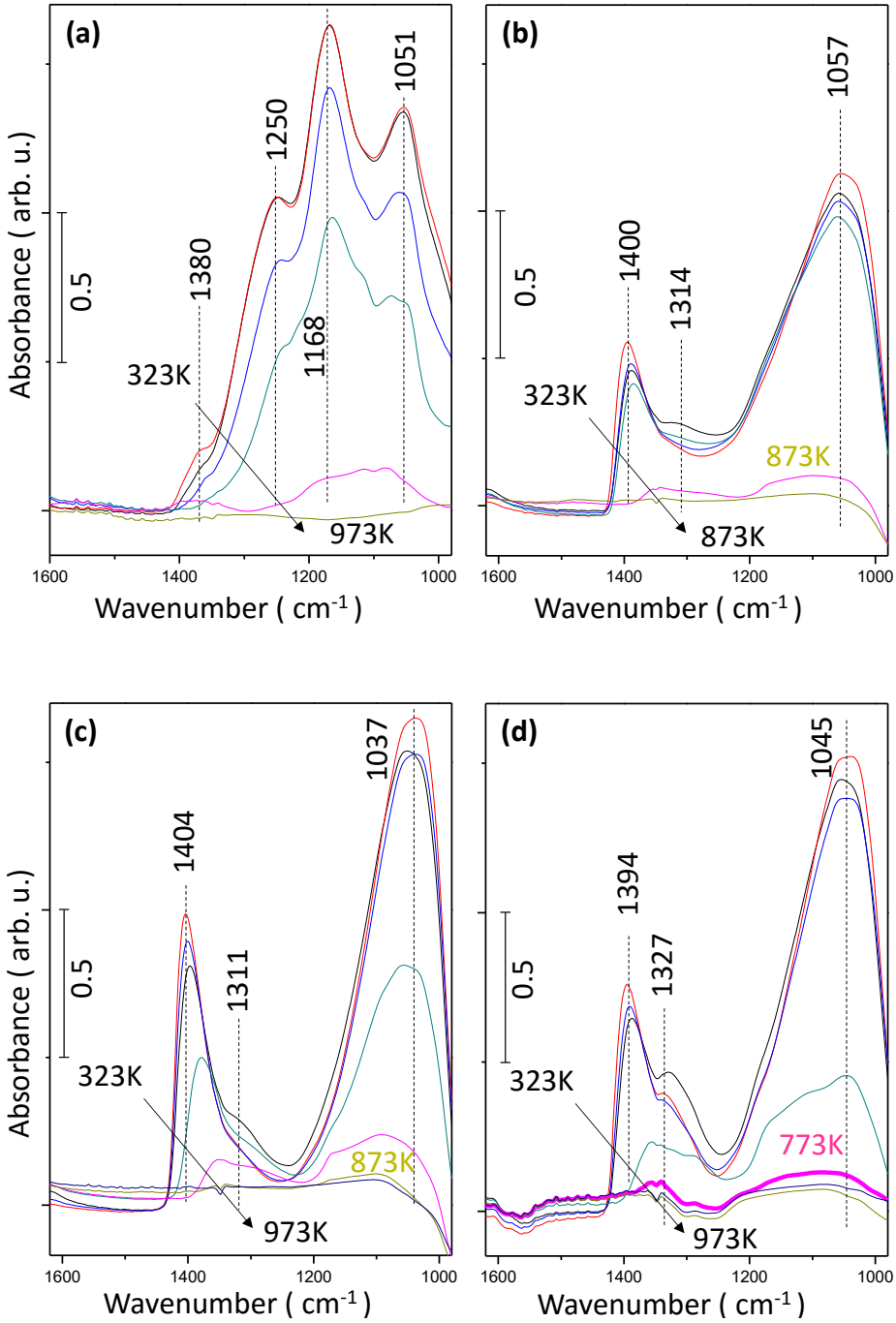

Figure 45. In-situ FTIR spectra for temperature dependent SO_x reduction in excess H_2 (g) (15.0 Torr) atmosphere on sulfur poisoned (a) Pt20BaAl, (b) Pt20CeAl, (c) Pt20ZrAl and (d) Pt10-10CeZrAl catalysts.

One of our former studies showed the formation of H_2S from SO_x species during the desorption of SO_x species on ɣ-Al_2O_3, TiO_2 and ɣ-Al_2O_3/TiO_2 catalysts [71] via the following reactions.

$$BaSO_4 + 4H_2 \rightarrow BaS + 4H_2O \quad (20)$$

$$BaS + H_2O \rightarrow BaO + H_2S \quad (21)$$

However, in the current experiments H_2S (g) generation from reaction between the H_2(g) and SO_x related functional groups could not be detected possibly due to the fact that the concentration of such species were below the detection limits of the currently used experimental techniques.

For the Pt20BaAl benchmark catalyst, regeneration of adsorbed sulfate/sulfite species can be achieved after annealing the catalyst to 973 K in hydrogen (Figure 45a). On the contrary, complete desulfation of Pt20CeAl, Pt20ZrAl and the co-impregnated Pt10-10CeZrAl surfaces can be attained at lower temperatures (Figures 45b-45d). It is clear that formation of strongly bound bulk/ionic like sulfate/sulfite functional groups on Pt20BaAl leads to an increase in the temperature needed to achieve complete sulfur regeneration. Increasing the annealing temperature to 773 K (pink spectra in Figure 45) during H_2 (g) exposure results in a quite limited extent of SO_x reduction on Pt20BaAl. In contrast, at the same temperature, a significant attenuation in the IR absorption intensities of SO_x species on Pt20CeAl, Pt20ZrAl and Pt10-10CeZrAl is visible. The presence of oxygen defects on ceria and zirconia domains and the effect of Pt-O-Ce sites at

the Pt/CeO_2 interface can be responsible for the improvement of the sulfur regeneration behavior of Ce-Zr containing catalysts [91].

3.6.2. SO_x Reduction *via in-situ* FTIR on Quaternary Oxides

Similar in-situ FT-IR experiments were also performed on quaternary oxides (Figure 46). Figure 46 shows that for the annealing steps < 573 K, no significant amount of sulfates/sulfites reduction was observed for any of the quaternary oxides. Annealing in H_2 (g) at 673 K (light blue spectra) results in a detectable amount of reduction in all types of sulfates on the 8 wt% BaO functionalized Pt10-10CeZr8BaAl and Pt8Ba10-10CeZrAl catalysts (Figures 46a and 46c). Further increase in temperature to 873 K reveals almost complete regeneration of SO_x species on 8 wt% BaO containing catalysts. On the other hand, in order to reach complete regeneration of sulfates and sulfites over high-baria loading (20 wt% BaO) catalyst surfaces, an elevated regeneration temperature of 973 K was needed. Achievement of SO_x regeneration only at elevated temperatures indicate a higher thermal stability of sulfates and sulfites on the 20 wt% BaO containing catalysts. Therefore, increase in BaO loading, makes the sulfur regeneration of NSR systems more challenging even in the presence of an aggressive reducing agent such as hydrogen.

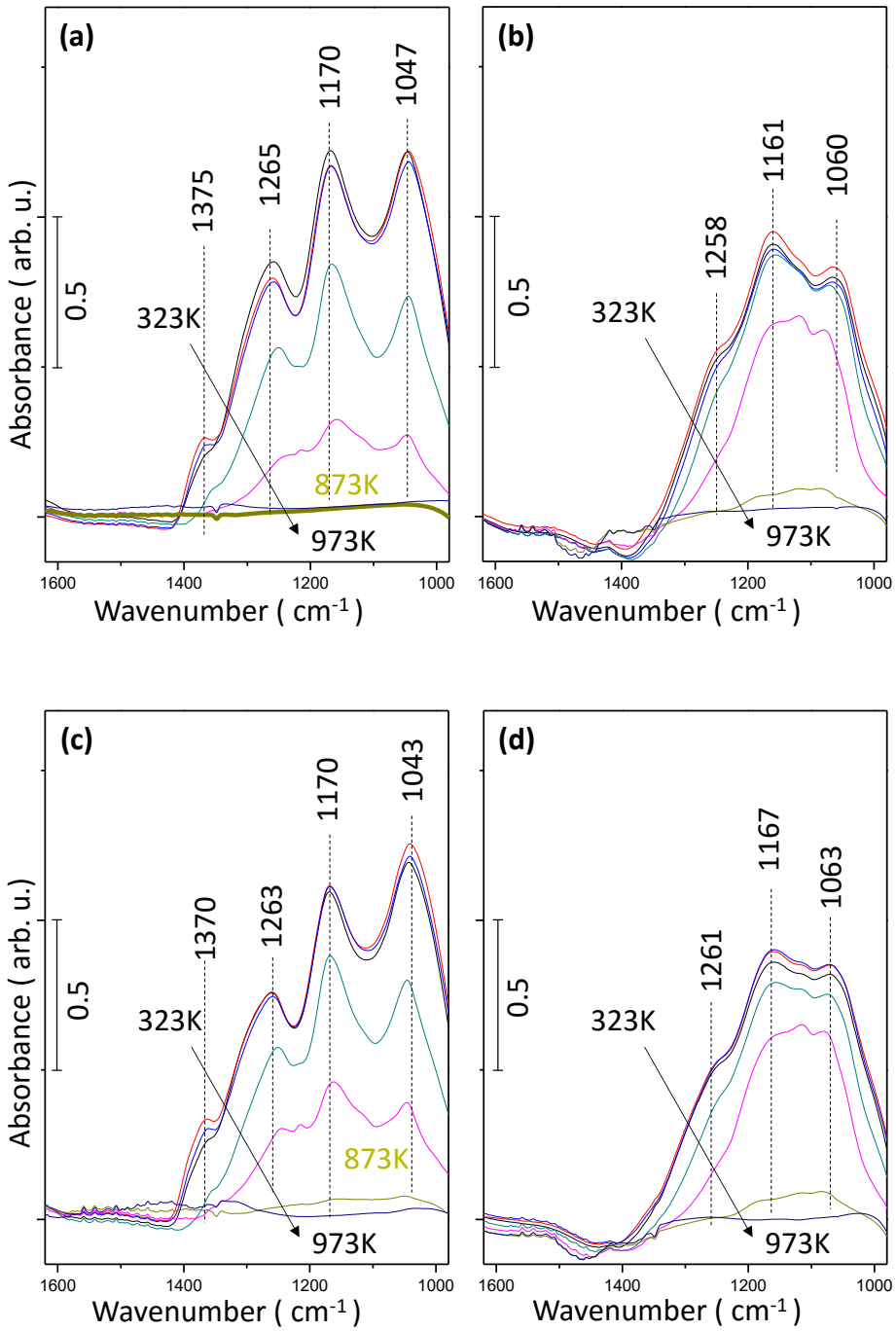

Figure 46. In-situ FTIR spectra for temperature dependent SO_x reduction in excess H_2 (g) (15.0 Torr) atmosphere on sulfur poisoned (a) Pt10-10CeZr8BaAl, (b) Pt10-10CeZr20BaAl, (c) Pt8Ba10-10CeZrAl and (d) Pt20Ba10-10CeZrAl catalysts.

3.7. SO_x Desorption Experiments *via* TPD: Quantitative SO_x Uptake Analysis and Thermal SO_x Regeneration in the Absence of a Reducing Agent

3.7.1. SO_x Desorption *via* TPD on Binary and Ternary Oxides

SO_x desorption via TPD provides information about thermal stability of stored SO_x features and thermal regeneration abilities of SO_x related species in the absence of reducing agents. Experiments on binary oxides and on the co-impregnated ternary oxide were performed after surface saturation with 2.0 Torr of SO_2 + O_2 gas mixture. To achieve complete saturation (i.e. severe poisoning), materials were heated to 673 K and held at this temperature for 30 min.

Figure 47 demonstrates the SO_x TPD profiles of binary and ternary oxides in the range of 323 – 1100 K showing O_2 (m/z=32) and SO_2 (m/z=64) desorption channels which are the main gases generated upon the thermal decomposition of sulfate/sulfite functional groups on the catalyst surfaces. The inset part in each panel illustrates the in-situ FTIR spectra of the samples obtained before the SO_x TPD analysis (i.e. after sulfur poisoning (black)) and after SO_x TPD analysis (i.e. after thermal regeneration (red)).

O_2 and SO_2 are the major desorption products for $BaSO_4$ and $Al_2(SO_4)_3$ which can be generated through the reactions given below.

$$BaSO_4 \rightarrow BaO + 1/2O_2 + SO_2 \qquad (22)$$

$$Al_2(SO_4)_3 \rightarrow Al_2O_3 + 3/2O_2 + 3SO_2 \qquad (23)$$

Sulfate/sulfite decomposition signals reveal a maximum at ca. 890 K on Pt20CeAl and Pt10-10CeZrAl. On the other hand, Pt20ZrAl binary oxide had a SO_x desorption maximum at 928 K. Figure 47 indicates that complete thermal sulfate/sulfite decomposition and regeneration can be achieved on Pt20CeAl, Pt20ZrAl and Pt10-10CeZrAl at T<1050 K, however sulfate/sulfite decomposition is incomplete even at T > 1050 K for the conventional Pt20BaAl catalyst. It is clear that Pt20BaAl reveals thermally more stable sulfate/sulfite features than Ce-Zr promoted binary and ternary oxides; hence the presence of basic sites leads to the formation of strong binding/poisoning sites for SO_x species.

Total relative SO_x uptake amounts of the investigated catalysts were quantified by integrating the areas under m/z=64 (SO_2) desorption channel in TPD (Figure 48). It is observed that Pt20BaAl, the benchmark catalyst, had the highest amount of SO_x uptake, in other words it has highest sulfur poisoning with respect to those of Pt20CeAl, Pt20ZrAl and Pt10-10CeZrAl catalysts.

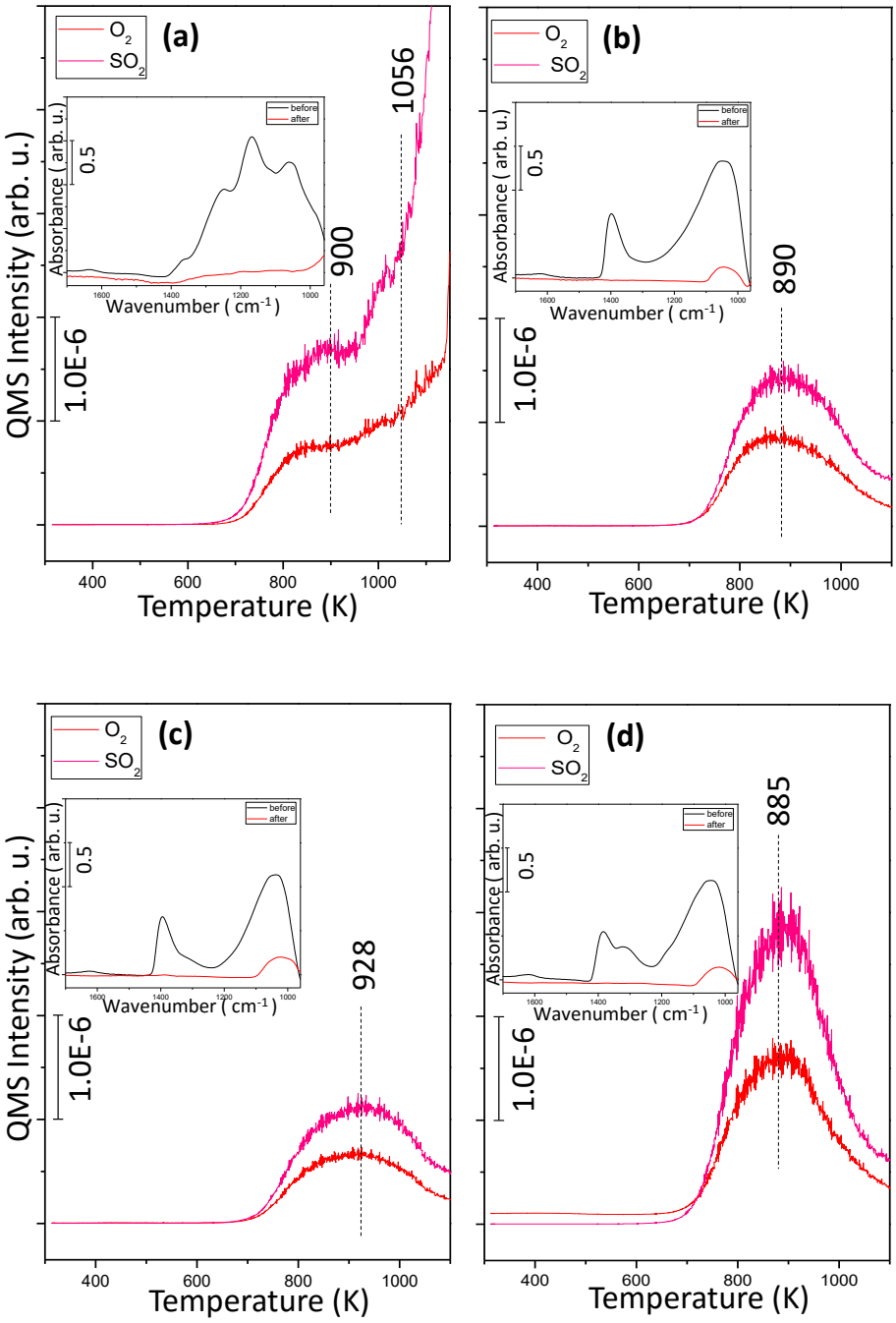

Figure 47. SO_x TPD profiles of (a) Pt20BaAl, (b) Pt20CeAl, (c) Pt20ZrAl and (d) Pt10-10CeZrAl after surface saturation with 2.0 Torr of SO_2 + O_2 (g) (SO_2 : O_2 = 1:10) at 623 K for 30 min. Inset shows the in-situ FTIR spectra presenting the residual SO_x species on the catalyst surfaces before (black) and after (red) TPD analysis.

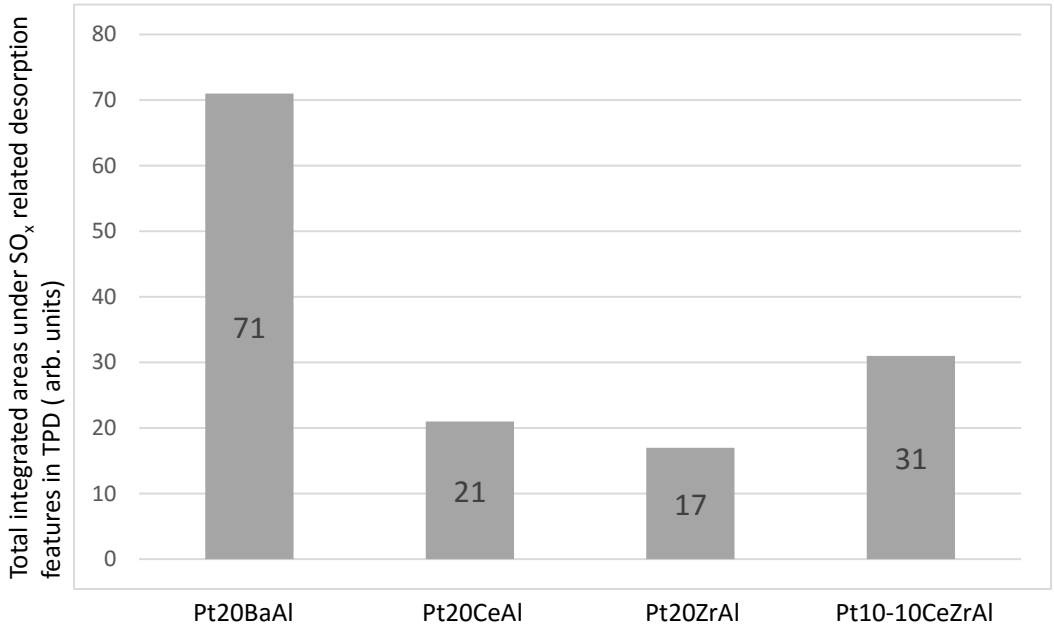

Figure 48. Total integrated areas under SO_x related desorption features in TPD (arb. units) for Pt20BaAl, Pt20CeAl, Pt20ZrAl and Pt10-10CeZrAl.

3.7.2. SO_x Desorption *via* TPD on Quaternary Oxides

Identical set of SO_x TPD experiments were also performed on quaternary oxides (Figure 49). Four different quaternary oxides were chosen where two of them had 8 wt% BaO content while the others had 20 wt% BaO loading with two different synthesis protocols. The effect of the impregnation sequence of BaO on the thermal stability of adsorbed sulfate/sulfite functional groups can be inferred from the TPD profiles in Figure 49. Low-baria loading catalysts namely, Pt10-10CeZr8BaAl and Pt8Ba10-10CeZrAl were found to reveal almost complete thermal decomposition. However increase in BaO loading results in increasing thermal decomposition temperatures for adsorbed SO_x species.

The effect of loading sequence of BaO on sulfate/sulfite decomposition pathways was more apparent for quaternary oxides with high-baria loading such as Pt10-10CeZr20BaAl and Pt20Ba10-10CeZrAl. Adding BaO domains *before* ceria and zirconia co-impregnation leads to a SO_x desorption maxima at 1110 K. On the other hand, loading BaO *over* co-impregnated CeO_2-ZrO_2/Al_2O_3 material surface reveals incomplete thermal decomposition even at temperatures higher than 1100 K. In-situ FTIR spectra recorded after thermal regeneration (red spectra in the insets given in Figure 49) showed that Ce-Zr promoted catalysts with a low-BaO loading of 8 wt.% can be completely regenerated from SO_x species using thermal decomposition while this is not the case for high BaO loading materials where residual SO_x species continue to exist even after thermal regeneration at elevated temperatures such as 1050 K.

Calculated integrated areas under SO_x related TPD signals (Figures 50-51) reveal that benchmark catalyst Pt20BaAl, has almost three times higher amount of SO_x uptake than other binary, ternary and quaternary oxides. Pt10-10CeZr20BaAl and Pt20Ba10-10CeZrAl have slightly lower sulfur uptake values than low BaO loading quaternary oxides (e.g. Pt10-10CeZr8BaAl and Pt8Ba10-10CeZrAl, and co-impregnated ternary oxide, Pt10-10CeZrAl), revealing reasonably high NO_x adsorption capacities (Figure 42 and 51) which are only slightly less than that of the benchmark catalyst. It can be concluded that BaO addition on Pt10-10CeZrAl catalyst increases sulfur resistance and NO_x adsorption capacity simultaneously.

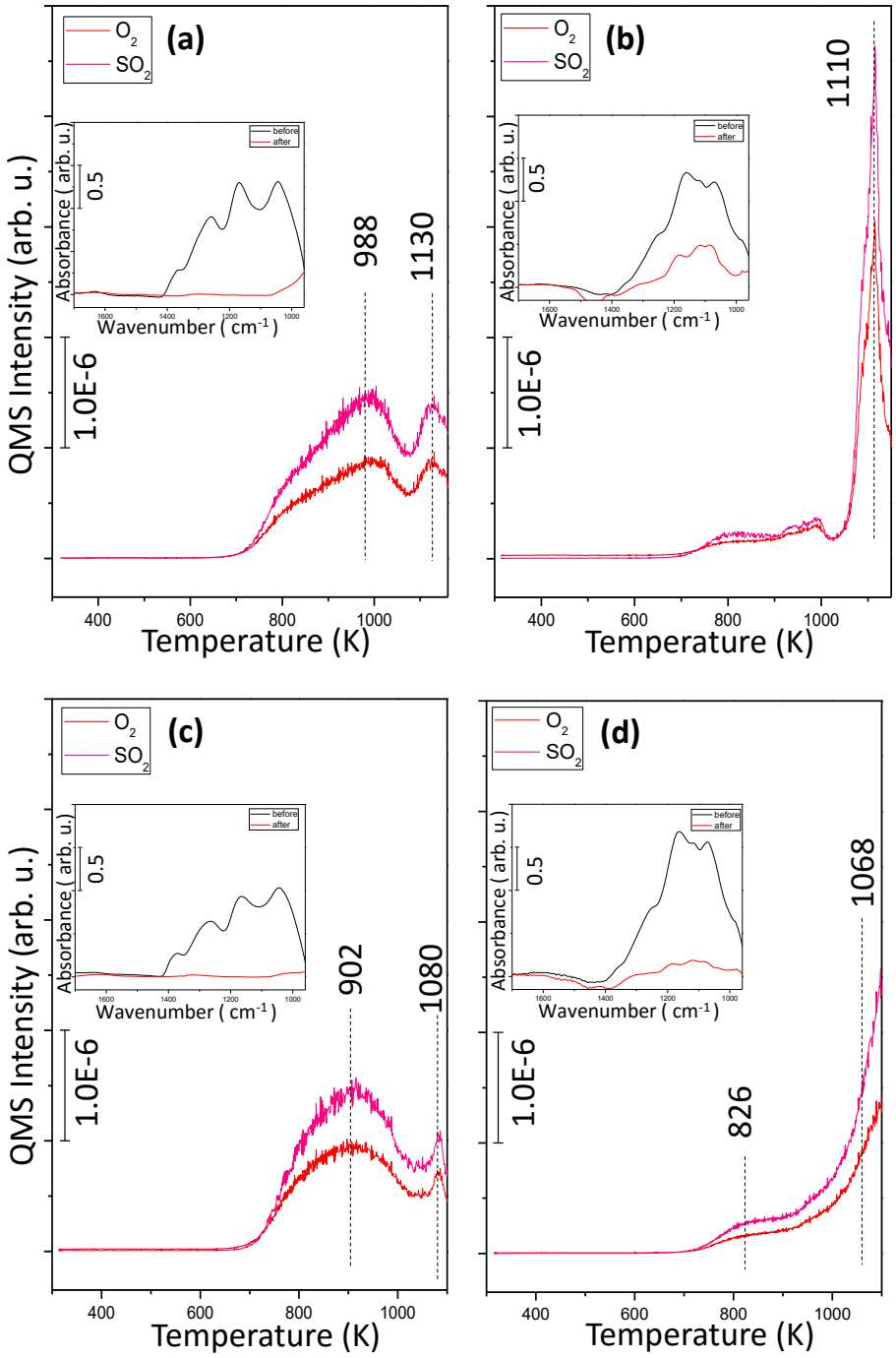

Figure 49. SO_x TPD profiles of (a) Pt10-10CeZr8BaAl, (b) Pt10-10CeZr20BaAl, (c) Pt8Ba10-10CeZrAl and (d) Pt20Ba10-10CeZrAl after surface saturation with 2.0 Torr of $SO_2 + O_2$ (g) ($SO_2 : O_2 = 1:10$) at 623 K for 30 min. Inset shows the in-situ FTIR spectra presenting the SO_x species on the catalyst surfaces before (black) and after (red) TPD analysis.

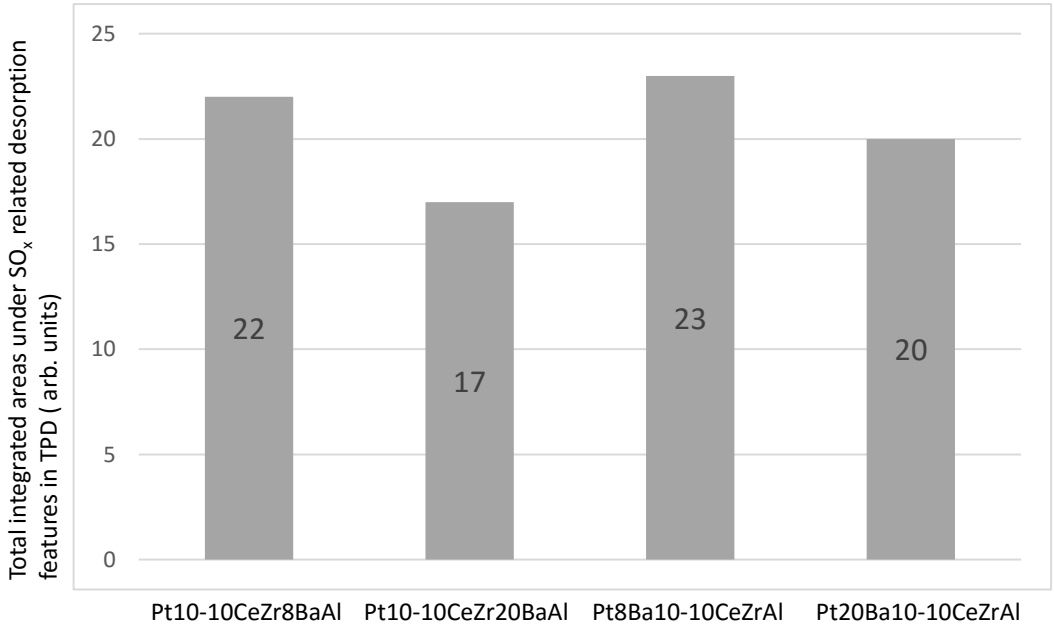

Figure 50. Total integrated areas under SO_x related desorption features in TPD (arb. units) for Pt10-10CeZr8BaAl, Pt10-10CeZr20BaAl, Pt8Ba10-10CeZrAl and Pt20Ba10-10CeZrAl.

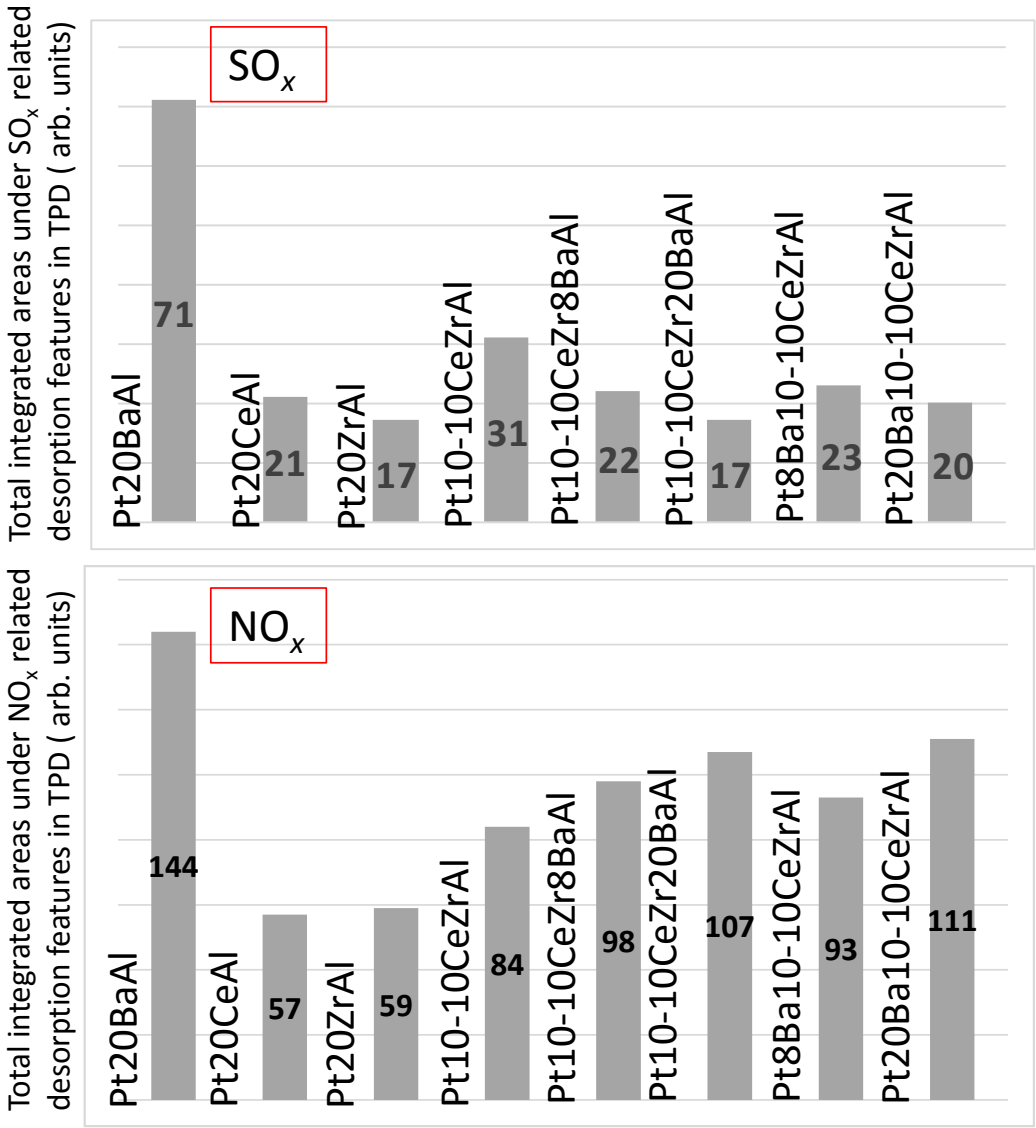

Figure 51. Global comparison of NSC and SO_x uptake values of all of the currently investigated NSR catalysts.

Chapter 4

Conclusion

In the current work, binary oxides; Pt20BaAl, Pt20CeAl and Pt20ZrAl; ternary oxides; Pt10-10CeZrAl, Pt10Ce10ZrAl and Pt10Zr10CeAl; quaternary oxides; Pt10-10CeZr8BaAl, Pt10-10CeZr20BaAl, Pt8Ba10-10CeZrAl and Pt20Ba10-10CeZrAl, were synthesized by wetness impregnation method. These materials were also characterized by XRD, BET, in-situ FTIR and TPD analysis. NO_x and SO_x uptake/storage characteristics and subsequent regeneration abilities in H_2 (g) were studied by in-situ FTIR while relative quantitative NO_x and SO_x storage capacities and thermal regeneration abilities in the absence of a reducing agent were investigated via TPD analysis. All results were discussed in a comparative fashion considering the Pt20BaAl conventional benchmark catalyst. Some of the major conclusions of the current study can be summarized as follows:

- Formation of the undesired $BaAl_2O_4$ phase was observed for the Pt20BaAl benchmark catalyst, and for high BaO loading quaternary oxides namely, Pt10-10CeZr20BaAl and Pt20Ba10-10CeZrAl.
- The impregnation of BaO on co-impregnated Ce-Zr mixed metal oxide surface facilitates the Pt dispersion and decreases average Pt crystallite size.

- BET analysis showed that binary oxides, ternary oxides and low BaO loaded quaternary oxides have similar SSA values. However, increasing BaO loading decreases the SSA values of quaternary oxides.
- The Ce-Zr containing binary and ternary oxides reveal similar NO_x adsorption geometries revealing the formation of surface nitrates, whereas Pt20BaAl and Ba-containing quaternary oxides also form bulk/ ionic nitrates due tp sintering of the baria domains.
- Co-presence of ceria and zirconia leads to higher NO_x storage capacity possibly due to higher oxygen storage capacity and higher defect concentrations of these surfaces.
- Nitrate/nitrite decomposition on Pt20CeAl takes place at lower temperatures than Pt20ZrAl, suggesting higher nitrate stability for the former surface.
- Pt20BaAl sample had higher NSC and thermally more stable nitrate features than Ce or Zr containing binary oxides.
- Presence of BaO in co-impregnated catalyst, Pt10-10CeZrAl, increases the stability of adsorbed nitrates/nitrites. Increasing the BaO loading increases the stability of nitrate/nitrites.
- Presence of Ce-Zr mixed oxides decreases the sulfur poisoning tendency and increases the thermal regeneration ability of the sulfur poisoned catalysts.
- Formation of strongly bound bulk/ionic like sulfate/sulfite functional groups on Pt20BaAl leads to an unfavorable increase in the temperature needed to achieve complete sulfur regeneration.

- Quaternary oxides, having more basic BaO sites increases the thermal stability of adsorbed sulfates and sulfites.
- BaO addition to Pt10-10CeZrAl increases sulfur resistance and increases NO_x uptake (per sample weight).
- A new NSR catalyst which is promoted with reducible mixed metal oxides namely, Pt20Ba10-10CeZrAl shows promising functional characteristics revealing superior sulfur resistance with respect to the Pt20BaAl conventional benchmark, with a minor sacrifice in NSC.

References

[1] E. E. Agency, "Environment and Human Health," No 5, 2013.

[2] E. E. Agency, "The contribution of the transport sector to total emissions of the main air pollutants in 2009," 2009.

[3] P. Granger and V. I. Parvulescu, "Catalytic NO x abatement systems for mobile sources: from three-way to lean burn after-treatment technologies," *Chemical Reviews,* vol. 111, pp. 3155-3207, 2011.

[4] E. E. Agency, "Air Quality in Europe- Report 2015," 5, 2015.

[5] E. E. Agency, "European Union emission inventory report

1990–2013 under the UNECE Convention on

Long-range Transboundary Air Pollution (LRTAP)," 2015.

[6] E. E. Agency, "National emissions reported to the Convention on Longrange

Transboundary Air Pollution (LRTAP Convention)," European Environment Agency2014.

[7] N. Miyoshi, S. i. Matsumoto, K. Katoh, T. Tanaka, J. Harada, N. Takahashi, *et al.,* "Development of new concept three-way catalyst for automotive lean-burn engines," SAE Technical Paper 0148-7191, 1995.

[8] J. G. Nunan, H. J. Robota, M. J. Cohn, and S. A. Bradley, "Physicochemical properties of Ce-containing three-way catalysts and the effect of Ce on catalyst activity," *Journal of Catalysis,* vol. 133, pp. 309-324, 1992.

[9] J. Kašpar, P. Fornasiero, and N. Hickey, "Automotive catalytic converters: current status and some perspectives," *Catalysis Today,* vol. 77, pp. 419-449, 2003.

[10] Y. Li, S. Roth, J. Dettling, and T. Beutel, "Effects of lean/rich timing and nature of reductant on the performance of a NOx trap catalyst," *Topics in Catalysis,* vol. 16, pp. 139-144, 2001.

[11] N. Takahashi, K. Yamazaki, H. Sobukawa, and H. Shinjoh, "The low-temperature performance of NO x storage and reduction catalyst," *Applied Catalysis B: Environmental,* vol. 70, pp. 198-204, 2007.

[12] W. S. Epling, A. Yezerets, and N. W. Currier, "The effect of exothermic reactions during regeneration on the NOX trapping efficiency of a NOX storage/reduction catalyst," *Catalysis letters,* vol. 110, pp. 143-148, 2006.

[13] S. Roy and A. Baiker, "NO x Storage− Reduction Catalysis: From Mechanism and Materials Properties to Storage− Reduction Performance," *Chemical Reviews,* vol. 109, pp. 4054-4091, 2009.

[14] C. Verrier, J. H. Kwak, D. H. Kim, C. H. Peden, and J. Szanyi, "NO x uptake on alkaline earth oxides (BaO, MgO, CaO and SrO) supported on γ-Al 2 O 3," *Catalysis Today,* vol. 136, pp. 121-127, 2008.

[15] T. Lesage, J. Saussey, S. Malo, M. Hervieu, C. Hedouin, G. Blanchard, *et al.*, "Operando FTIR study of NO x storage over a Pt/K/Mn/Al 2 O 3-CeO 2 catalyst," *Applied Catalysis B: Environmental,* vol. 72, pp. 166-177, 2007.

[16] A. Kustov and M. Makkee, "Application of NO x storage/release materials based on alkali-earth oxides supported on Al 2 O 3 for high-temperature diesel soot oxidation," *Applied Catalysis B: Environmental,* vol. 88, pp. 263-271, 2009.

[17] M. Piacentini, M. Maciejewski, and A. Baiker, "NO x storage-reduction behavior of Pt–Ba/MO 2 (MO 2= SiO 2, CeO 2, ZrO 2) catalysts," *Applied Catalysis B: Environmental,* vol. 72, pp. 105-117, 2007.

[18] S. i. Matsumoto, "DeNO x catalyst for automotive lean-burn engine," *Catalysis today,* vol. 29, pp. 43-45, 1996.

[19] L. Olsson, H. Persson, E. Fridell, M. Skoglundh, and B. Andersson, "A Kinetic Study of NO Oxidation and NO x Storage on Pt/Al2O3 and Pt/BaO/Al2O3," *The Journal of Physical Chemistry B,* vol. 105, pp. 6895-6906, 2001.

[20] P. J. Schmitz and R. J. Baird, "NO and NO2 Adsorption on Barium Oxide: Model Study of the Trapping Stage of NO x Conversion via Lean NO x Traps," *The Journal of Physical Chemistry B,* vol. 106, pp. 4172-4180, 2002.

[21] P. Forzatti, L. Castoldi, I. Nova, L. Lietti, and E. Tronconi, "NO x removal catalysis under lean conditions," *Catalysis today,* vol. 117, pp. 316-320, 2006.

[22] I. Nova, L. Castoldi, L. Lietti, E. Tronconi, P. Forzatti, F. Prinetto, *et al.*, "NO x adsorption study over Pt–Ba/alumina catalysts: FT-IR and pulse experiments," *Journal of catalysis,* vol. 222, pp. 377-388, 2004.

[23] I. Nova, L. Castoldi, F. Prinetto, V. Dal Santo, L. Lietti, E. Tronconi, *et al.*, "NO x adsorption study over Pt–Ba/alumina catalysts: FT-IR and reactivity study," *Topics in catalysis,* vol. 30, pp. 181-186, 2004.

[24] J. H. Kwak, D. H. Kim, T. Szailer, C. H. Peden, and J. Szanyi, "NO x uptake mechanism on Pt/BaO/Al2O3 catalysts," *Catalysis Letters,* vol. 111, pp. 119-126, 2006.

[25] H. Abdulhamid, E. Fridell, and M. Skoglundh, "Influence of the type of reducing agent (H2, CO, C3H6 and C3H8) on the reduction of stored NO X in a Pt/BaO/Al2O3 model catalyst," *Topics in catalysis,* vol. 30, pp. 161-168, 2004.

[26] E. Fridell, H. Persson, L. Olsson, B. Westerberg, A. Amberntsson, and M. Skoglundh, "Model studies of NOx storage and sulphur deactivation of NOx storage catalysts," *topics in catalysis,* vol. 16, pp. 133-137, 2001.

[27] R. Burch and P. Millington, "Selective reduction of nitrogen oxides by hydrocarbons under lean-burn conditions using supported platinum group metal catalysts," *Catalysis Today,* vol. 26, pp. 185-206, 1995.

[28] D. H. Kim, Y.-H. Chin, G. G. Muntean, A. Yezeretz, N. W. Currier, W. S. Epling, *et al.*, "Relationship of Pt Particle Size to the NO x Storage Performance of Thermally Aged Pt/BaO/Al2O3 Lean NO x Trap

Catalysts," *Industrial & engineering chemistry research,* vol. 45, pp. 8815-8821, 2006.

[29] G. Dutta, U. V. Waghmare, T. Baidya, and M. Hegde, "Hydrogen spillover on CeO 2/Pt: enhanced storage of active hydrogen," *Chemistry of Materials,* vol. 19, pp. 6430-6436, 2007.

[30] L. Olsson and E. Fridell, "The Influence of Pt Oxide Formation and Pt Dispersion on the Reactions NO 2⇔ NO+ 1/2 O 2 over Pt/Al 2 O 3 and Pt/BaO/Al 2 O 3," *Journal of Catalysis,* vol. 210, pp. 340-353, 2002.

[31] L. Lietti, P. Forzatti, I. Nova, and E. Tronconi, "NO x Storage Reduction over Pt・ Ba/γ-Al 2 O 3 Catalyst," *Journal of catalysis,* vol. 204, pp. 175-191, 2001.

[32] I. Malpartida, M. A. L. Vargas, L. J. Alemany, E. Finocchio, and G. Busca, "Pt–Ba–Al 2 O 3 for NO x storage and reduction: Characterization of the dispersed species," *Applied Catalysis B: Environmental,* vol. 80, pp. 214-225, 2008.

[33] M. Piacentini, M. Maciejewski, T. Bürgi, and A. Baiker, "Role of support in lean DeNO x catalysis," *Topics in catalysis,* vol. 30, pp. 71-80, 2004.

[34] M. Casapu, J.-D. Grunwaldt, M. Maciejewski, M. Wittrock, U. Göbel, and A. Baiker, "Formation and stability of barium aluminate and cerate in NO x storage-reduction catalysts," *Applied Catalysis B: Environmental,* vol. 63, pp. 232-242, 2006.

[35] P. Broqvist, H. Grönbeck, E. Fridell, and I. Panas, "NO x storage on BaO: theory and experiment," *Catalysis Today,* vol. 96, pp. 71-78, 2004.

[36] H. Mahzoul, J. Brilhac, and P. Gilot, "Experimental and mechanistic study of NOx adsorption over NOx trap catalysts," *Applied Catalysis B: Environmental,* vol. 20, pp. 47-55, 1999.

[37] M. Casapu, J.-D. Grunwaldt, M. Maciejewski, A. Baiker, M. Wittrock, U. Göbel, *et al.*, "Thermal ageing phenomena and strategies towards reactivation of NO x-storage catalysts," *Topics in Catalysis,* vol. 42, pp. 3-7, 2007.

[38] M. Symalla, A. Drochner, H. Vogel, S. Philipp, U. Göbel, and W. Müller, "IR-study of formation of nitrite and nitrate during NOx-adsorption on NSR-catalysts-compounds CeO2 and BaO/CeO2," *Topics in Catalysis,* vol. 42, pp. 199-202, 2007.

[39] M. Casapu, J.-D. Grunwaldt, M. Maciejewski, A. Baiker, S. Eckhoff, U. Göbel, *et al.*, "The fate of platinum in Pt/Ba/CeO 2 and Pt/Ba/Al 2 O 3 catalysts during thermal aging," *Journal of Catalysis,* vol. 251, pp. 28-38, 2007.

[40] M. Casapu, J.-D. Grunwaldt, M. Maciejewski, F. Krumeich, A. Baiker, M. Wittrock, *et al.*, "Comparative study of structural properties and NO x storage-reduction behavior of Pt/Ba/CeO 2 and Pt/Ba/Al 2 O 3," *Applied Catalysis B: Environmental,* vol. 78, pp. 288-300, 2008.

[41] M. Casapu, J.-D. Grunwaldt, M. Maciejewski, A. Baiker, R. Hoyer, M. Wittrock, *et al.*, "Enhancement of Activity and Self-reactivation of NSR-catalysts by Temporary Formation of BaPtO3-perovskite," *Catalysis Letters,* vol. 120, pp. 1-7, 2008.

[42] Y. Ji, J.-S. Choi, T. J. Toops, M. Crocker, and M. Naseri, "Influence of ceria on the NO x storage/reduction behavior of lean NO x trap catalysts," *Catalysis Today,* vol. 136, pp. 146-155, 2008.

[43] M. Piacentini, M. Maciejewski, and A. Baiker, "Supported Pt-Ba NO x storage-reduction catalysts: Influence of support and Ba loading on stability and storage efficiency of Ba-containing species," *Applied Catalysis B: Environmental,* vol. 66, pp. 126-136, 2006.

[44] J. H. Kwak, D. H. Kim, J. Szanyi, and C. H. Peden, "Excellent sulfur resistance of Pt/BaO/CeO 2 lean NO x trap catalysts," *Applied Catalysis B: Environmental,* vol. 84, pp. 545-551, 2008.

[45] Z. Say, E. I. Vovk, V. I. Bukhtiyarov, and E. Ozensoy, "Influence of ceria on the NO x reduction performance of NO x storage reduction catalysts," *Applied Catalysis B: Environmental,* vol. 142, pp. 89-100, 2013.

[46] M. Yang, Y. Li, J. Wang, and M. Shen, "Effects of CO 2 and steam on Ba/Ce-based NOx storage reduction catalysts during lean aging," *Journal of Catalysis,* vol. 271, pp. 228-238, 2010.

[47] X. Liu, Y. Ryabenkova, and M. Conte, "Catalytic oxygen activation versus autoxidation for industrial applications: a physicochemical approach," *Physical Chemistry Chemical Physics,* vol. 17, pp. 715-731, 2015.

[48] E. Mamontov, T. Egami, R. Brezny, M. Koranne, and S. Tyagi, "Lattice defects and oxygen storage capacity of nanocrystalline ceria and ceria-zirconia," *The Journal of Physical Chemistry B,* vol. 104, pp. 11110-11116, 2000.

[49] K. Hashimoto, N. Toukai, R. Hamada, and S. Imamura, "Reduction of Rh/CeO2-ZrO2 with hydrogen," *Catalysis letters,* vol. 50, pp. 193-198, 1998.

[50] F. Namavar, G. Wang, C. L. Cheung, R. F. Sabirianov, X. C. Zeng, W. N. Mei, *et al.*, "Thermal stability of nanostructurally stabilized zirconium oxide," *Nanotechnology,* vol. 18, p. 415702, 2007.

[51] C. Â. M. Volpato, F. Bondioli, L. G. D.´Altoé Garbelotto, and M. C. Fredel, *Application of zirconia in dentistry: biological, mechanical and optical considerations*: INTECH Open Access Publisher, 2011.

[52] S. i. Matsumoto, Y. Ikeda, H. Suzuki, M. Ogai, and N. Miyoshi, "NO x storage-reduction catalyst for automotive exhaust with improved tolerance against sulfur poisoning," *Applied Catalysis B: Environmental,* vol. 25, pp. 115-124, 2000.

[53] P. R. Shah, T. Kim, G. Zhou, P. Fornasiero, and R. J. Gorte, "Evidence for entropy effects in the reduction of ceria-zirconia solutions," *Chemistry of materials,* vol. 18, pp. 5363-5369, 2006.

[54] S. i. Matsumoto, "Recent advances in automobile exhaust catalysts," *Catalysis Today,* vol. 90, pp. 183-190, 2004.

[55] L. Z. Min, W. J. Li, Z. J. Bo, C. Y. Qiang, Y. S. Hui, and G. M. Chu, "Catalytic combustion of toluene over platinum supported on Ce–Zr–O solid solution modified by Y and Mn," *Journal of hazardous materials,* vol. 149, pp. 742-746, 2007.

[56] X. Wang, J. Mi, W. Wen, Z. Chen, L. Jiang, and R. Wang, "Influence of Ce 0.6 Zr 0.4 O 2 loading on the sulfur poisoning and regenerability of

Pt/Ba/Al 2 O 3–Ce 0.6 Zr 0.4 O 2 in NOx removal by hydrogen," *Materials Research Bulletin,* vol. 75, pp. 41-46, 2016.

[57] R. Strobel, F. Krumeich, S. E. Pratsinis, and A. Baiker, "Flame-derived Pt/Ba/CexZr1− xO2: Influence of support on thermal deterioration and behavior as NOx storage-reduction catalysts," *Journal of Catalysis,* vol. 243, pp. 229-238, 2006.

[58] S. Elbouazzaoui, E. Corbos, X. Courtois, P. Marecot, and D. Duprez, "A study of the deactivation by sulfur and regeneration of a model NSR Pt/Ba/Al 2 O 3 catalyst," *Applied Catalysis B: Environmental,* vol. 61, pp. 236-243, 2005.

[59] J. Li, J. Theis, W. Chun, C. Goralski, R. Kudla, J. Ura, *et al.*, "Sulfur poisoning and desulfation of the lean NOx trap," SAE Technical Paper 0148-7191, 2001.

[60] J. Parks, S. Huff, J. Pihl, J.-S. Choi, and B. West, "Nitrogen selectivity in lean NOx trap catalysis with diesel engine in-cylinder regeneration," SAE Technical Paper 0148-7191, 2005.

[61] C. Sedlmair, K. Seshan, A. Jentys, and J. Lercher, "Studies on the deactivation of NO x storage-reduction catalysts by sulfur dioxide," *Catalysis Today,* vol. 75, pp. 413-419, 2002.

[62] D. H. Kim, J. Szanyi, J. H. Kwak, T. Szailer, J. Hanson, C. M. Wang, *et al.*, "Effect of barium loading on the desulfation of Pt-BaO/Al2O3 studied by H2 TPRX, TEM, sulfur K-edge XANES, and in situ TR-XRD," *The Journal of Physical Chemistry B,* vol. 110, pp. 10441-10448, 2006.

[63] V. Easterling, Y. Ji, M. Crocker, J. Ura, J. R. Theis, and R. W. McCabe, "Effect of ceria on the desulfation characteristics of model lean NO x trap catalysts," *Catalysis Today,* vol. 151, pp. 338-346, 2010.

[64] L. Limousy, H. Mahzoul, J. Brilhac, F. Garin, G. Maire, and P. Gilot, "A study of the regeneration of fresh and aged SO x adsorbers under reducing conditions," *Applied Catalysis B: Environmental,* vol. 45, pp. 169-179, 2003.

[65] K. Nakamoto, "Infrared and Raman Spectra of Inorganic and Coordination Chemistry," *Part A: Theory and Applications in Inorganic Chemistry, 5th edn., Wiley, New York,* 1997.

[66] K. I. Hadjiivanov, "Identification of neutral and charged N x O y surface species by IR spectroscopy," *Catalysis Reviews,* vol. 42, pp. 71-144, 2000.

[67] A. A. Davydov and N. Sheppard, *Molecular spectroscopy of oxide catalyst surfaces* vol. 690: Wiley Chichester, 2003.

[68] S.-J. Huang, A. Walters, and M. Vannice, "Adsorption and decomposition of NO on lanthanum oxide," *Journal of Catalysis,* vol. 192, pp. 29-47, 2000.

[69] V. Sadykov, V. Lunin, V. Matyshak, E. Paukshtis, A. Y. Rozovskii, N. Bulgakov, *et al.*, "The reaction mechanism of selective catalytic reduction of nitrogen oxides by hydrocarbons in excess oxygen: Intermediates, their reactivity, and routes of transformation," *Kinetics and catalysis,* vol. 44, pp. 379-400, 2003.

[70] Y. Ji, T. J. Toops, J. A. Pihl, and M. Crocker, "NO x storage and reduction in model lean NO x trap catalysts studied by in situ DRIFTS," *Applied Catalysis B: Environmental,* vol. 91, pp. 329-338, 2009.

[71] G. S. Şentürk, E. I. Vovk, V. I. Zaikovskii, Z. Say, A. M. Soylu, V. I. Bukhtiyarov, *et al.*, "SO x uptake and release properties of TiO 2/Al 2 O 3 and BaO/TiO 2/Al 2 O 3 mixed oxide systems as NO x storage materials," *Catalysis Today,* vol. 184, pp. 54-71, 2012.

[72] M. Kantcheva and E. Z. Ciftlikli, "FTIR Spectroscopic Characterization of NO x Species Adsorbed on ZrO2 and ZrO2-SO42," *The Journal of Physical Chemistry B,* vol. 106, pp. 3941-3949, 2002.

[73] C. C. Chang, "Infrared studies of SO2 on γ-alumina," *Journal of Catalysis,* vol. 53, pp. 374-385, 1978.

[74] M. Waqif, A. Pieplu, O. Saur, J. Lavalley, and G. Blanchard, "Use of CeO 2・ Al 2 O 3 as a SO 2 sorbent," *Solid State Ionics,* vol. 95, pp. 163-167, 1997.

[75] O. Saur, M. Bensitel, A. M. Saad, J. Lavalley, C. P. Tripp, and B. Morrow, "The structure and stability of sulfated alumina and titania," *Journal of Catalysis,* vol. 99, pp. 104-110, 1986.

[76] H. Abdulhamid, E. Fridell, J. Dawody, and M. Skoglundh, "In situ FTIR study of SO 2 interaction with Pt/BaCO 3/Al 2 O 3 NO x storage catalysts under lean and rich conditions," *Journal of Catalysis,* vol. 241, pp. 200-210, 2006.

[77] E. Kayhan, "Structure and NOx uptake properties of Fe-Ba/Al2O3 as a model NOx storage material," Bilkent University, 2009.

[78] F. Rodrigues, L. Juste, C. Potvin, J. Tempere, G. Blanchard, and G. Djega-Mariadassou, "NOx storage on barium-containing three-way catalyst in the presence of CO2," *Catalysis Letters,* vol. 72, pp. 59-64, 2001.

[79] P. Scherrer, "The Scherrer Formula for X-Ray Particle Size Determination," *Göttinger Nachrichten,* vol. 2, pp. 98-100, 1918.

[80] B. Westerberg and E. Fridell, "A transient FTIR study of species formed during NO x storage in the Pt/BaO/Al 2 O 3 system," *Journal of Molecular Catalysis A: Chemical,* vol. 165, pp. 249-263, 2001.

[81] Z. Say, M. Tohumeken, and E. Ozensoy, "NO x storage and reduction pathways on zirconia and titania functionalized binary and ternary oxides as NO x storage and reduction (NSR) systems," *Catalysis Today,* vol. 231, pp. 135-144, 2014.

[82] T. Szailer, J. H. Kwak, D. H. Kim, J. C. Hanson, C. H. Peden, and J. Szanyi, "Reduction of stored NO x on Pt/Al 2 O 3 and Pt/BaO/Al 2 O 3 catalysts with H 2 and CO," *Journal of Catalysis,* vol. 239, pp. 51-64, 2006.

[83] J. B. Thomson, A. R. Armstrong, and P. G. Bruce, "A new class of pyrochlore solid solution formed by chemical intercalation of oxygen," *Journal of the American Chemical Society,* vol. 118, pp. 11129-11133, 1996.

[84] J. B. Thomson, A. R. Armstrong, and P. G. Bruce, "An interstitial pyrochlore formed by chemical intercalation of oxygen," *Chemical Communications,* pp. 1165-1166, 1996.

[85] H. Kishimoto, T. Omata, S. Otsuka-Yao-Matsuo, K. Ueda, H. Hosono, and H. Kawazoe, "Crystal structure of metastable κ-CeZrO 4 phase possessing an ordered arrangement of Ce and Zr ions," *Journal of alloys and compounds,* vol. 312, pp. 94-103, 2000.

[86] S. Otsuka-Yao-Matsuo, T. Omata, N. Izu, and H. Kishimoto, "Oxygen Release Behavior of CeZrO 4 Powders and Appearance of New Compoundsκand t," *Journal of Solid State Chemistry,* vol. 138, pp. 47-54, 1998.

[87] M. Yashima, "Invited Review: Some recent developments in the atomic-scale characterization of structural and transport properties of ceria-based catalysts and ionic conductors," *Catalysis Today,* vol. 253, pp. 3-19, 2015.

[88] Ş. Özkara-Aydınoğlu, E. Özensoy, and A. E. Aksoylu, "The effect of impregnation strategy on methane dry reforming activity of Ce promoted Pt/ZrO 2," *international journal of hydrogen energy,* vol. 34, pp. 9711-9722, 2009.

[89] S. Hodjati, P. Bernhardt, C. Petit, V. Pitchon, and A. Kiennemann, "Removal of NO x: Part II. Species formed during the sorption/desorption processes on barium aluminates," *Applied Catalysis B: Environmental,* vol. 19, pp. 221-232, 1998.

[90] H. Yao, H. Stepien, and H. Gandhi, "The effects of SO2 on the oxidation of hydrocarbons and carbon monoxide over Ptγ-Al2O3 catalysts," *Journal of Catalysis,* vol. 67, pp. 231-236, 1981.

[91] Z. Say, E. I. Vovk, V. I. Bukhtiyarov, and E. Ozensoy, "Enhanced sulfur tolerance of ceria-promoted NO x storage reduction (NSR) catalysts: Sulfur uptake, thermal regeneration and reduction with H2 (g)," *Topics in Catalysis,* vol. 56, pp. 950-957, 2013.